universität wien

MASTERARBEIT / MASTER'S THESIS

Titel der Masterarbeit / Title of the Master's Thesis

„Assessment of Oceanic Transports in the Indonesian Throughflow region as represented by Ocean Reanalyses“

verfasst von / submitted by

Magdalena Fritz, BSc BSc

angestrebter akademischer Grad / in partial fulfilment of the requirements for the degree of

Master of Science (MSc)

Wien, 2022 / Vienna, 2022

Studienkennzahl lt. Studienblatt / degree programme code as it appears on the student record sheet:	UA 066 614
Studienrichtung lt. Studienblatt / degree programme as it appears on the student record sheet:	Masterstudium Meteorologie
Betreut von / Supervisor:	Univ.-Prof. Mag. Dr. Leopold Haimberger

Abstract

The Indonesian Seas not only form the primary low latitude connection between the Pacific and the Indian Ocean but also represent a bathymetrically interesting region. This connection is referred to as the Indonesian Throughflow (ITF) and is the focus of this thesis. The thesis centers around the transport of volume through the major passages of Makassar Strait, Lombok Strait, Ombai Strait, and Timor Passage which have already been the target of several measurement campaigns, including the INSTANT program (2004-2006) and the MITF program (2006-2017). Those campaigns aimed to capture characteristics of the Indonesian Throughflow (e.g., velocity, temperature, and salinity) and to establish connections with the larger-scale ocean and the climate system. However, real-time monitoring of the ITF is only possible with Reanalyses, and in order to employ them, their skills have to be evaluated. Comparisons between observations and different Reanalysis products allow for a successful study of the product's performance. The use of five $1/4^\circ \times 1/4^\circ$ products (CGLORS, GLORYS2V4, FOAM, ORAS5, and ORAP6) and one $1/12^\circ \times 1/12^\circ$ product (GLORYS12V1) underlines the importance of a higher resolution product, especially in more narrow straits. Results confirm that there is a qualitative agreement between observations and Reanalyses, and they reflect the flow regimes in the different passages adequately. Nonetheless, in terms of magnitude, there are still notable over- and underestimations in broader and more narrow straits, respectively. Furthermore, we study the seasonal dependence of the ITF transport on the large-scale sea level gradient, defined by the sea level anomalies between the western Pacific and the eastern Indian Ocean. While the upper layer ($<$300 m) of the ITF corresponds to the sea level gradient, our findings reveal a reversal of the current response in the lower layer ($>$300 m). The results raise important questions about the processes that influence the ITF vertical profile and the apparent two-layer system.

Kurzfassung

Die indonesischen Meere bilden nicht nur die wichtigste Verbindung zwischen dem Pazifik und dem Indischen Ozean, sondern stellen auch bathymetrisch gesehen eine durchaus interessante Region dar. Die Verbindung zwischen dem Pazifik und dem Indischen Ozean wird als Indonesian Throughflow bezeichnet und stellt den Fokus dieser Arbeit dar. Die vorliegende Arbeit konzentriert sich auf Volumentransporte durch die bedeutenden Meeresstraßen Makassar, Lombok, Ombai und Timor, welche bereits das Ziel mehrerer Messkampagnen waren, darunter das INSTANT Projekt (2004-2006) und das MITF Projekt (2006-2017). Ziel dieser Kampagnen war sowohl die Erfassung von Eigenschaften des Indonesian Throughflow (z.B. Geschwindigkeit, Temperatur und Salzgehalt) als auch Verbindungen zum globalen Ozean und dem Klimasystem herzustellen. Die Echtzeitüberwachung des ITF ist jedoch nur mit Reanalysen möglich. Um diese einsetzen zu können, müssen ihre Fähigkeiten beurteilt werden. Vergleiche zwischen Beobachtungen und verschiedenen Reanalyse-Produkten ermöglichen eine solche Beurteilung. Die Verwendung von fünf $1/4° \times 1/4°$ Produkten (CGLORS, GLORYS2V4, FOAM, ORAS5 und ORAP6) und einem $1/12° \times 1/12°$ Produkt (GLORYS12V1) unterstreicht die Bedeutung von höher aufgelösten Produkten, insbesondere in engeren Meeresstraßen. Die Ergebnisse bestätigen, dass es eine qualitative Übereinstimmung zwischen Beobachtungen und Reanalysen gibt und dass Strömungsregime in den verschiedenen Straßen von Reanalysen angemessen wiedergegeben werden können. Dennoch kann es zu erheblichen Überschätzungen der Größenordnung in breiten Straßen kommen, sowie zu Unterschätzungen in engeren Straßen. Darüber hinaus untersuchen wir die saisonale Abhängigkeit des ITF-Transportes vom großskaligen Meeresspiegelgradienten, welcher durch die Meeresspiegelanomalien zwischen dem westlichen Pazifik und dem östlichen Indischen Ozean definiert ist. Während die obere Schicht ($<$300 m) des ITF der Dynamik des Meeresspiegelgradienten folgt, zeigen unsere Ergebnisse eine Umkehrung der Strömungsreaktion in der unteren Schicht ($>$300 m). Die Ergebnisse implizieren ein Zweischicht-System und werfen wichtige Fragen zu den Prozessen auf, welche das vertikale ITF-Profil beeinflussen.

Contents

List of Tables 6

List of Figures 6

1. Introduction 8
1.1. Monitoring the ITF . . . 12

2. Physical characteristics of the ocean 15
2.1. Geostrophic flow . . . 15
2.2. Sea Level Balance in Ocean Models . . . 19
2.3. Dynamics of Circulation . . . 19
2.4. Equatorial Waves . . . 21

3. Research Questions 25

4. Data and Methods 26
4.1. Moorings . . . 26
4.2. Reanalysis Products . . . 29
4.3. Observational Data . . . 32
4.4. Reanalysis Data . . . 34
4.5. Satellite-derived Data . . . 36
4.6. Methods . . . 37

5. Results and Discussion 40
5.1. Comparison of Observations and Reanalyses . . . 41
5.1.1. Cross sections (INSTANT) . . . 41
5.1.2. Vertical Profiles (INSTANT) . . . 57
5.1.3. Performance Test (INSTANT) . . . 61
5.1.4. Seasonal Cycle (INSTANT) . . . 64
5.1.5. Mean Seasonal Cycle (INSTANT) . . . 69
5.1.6. Cross correlation Makassar (INSTANT+MITF) . . . 72
5.1.7. Anomaly Time Series (INSTANT+MITF) . . . 73
5.2. Dependence on large-scale sea level gradients . . . 75
5.3. ENSO . . . 91
5.4. Conservation of volume within the Indonesian Seas . . . 98

6. Conclusions and Outlook 100

References 103

A. Appendix 115

List of Tables

1. INSTANT program (2004 - 2006) . . . 14
2. MITF program (2006 - 2017) . . . 14
3. Overview Reanalysis products . . . 31
4. ITF transport estimates INSTANT (2004 - 2006) . . . 45
5. Seasonal averages of ITF transport INSTANT (2004 - 2006) . . . 71
6. ITF transport estimates INSTANT (2004 - 2006) Reanalysis products . . . 115

List of Figures

1. Study area: the Indonesian Archipelago . . . 10
2. Seasonal averages of SLA during Australian-Indonesian monsoon . . . 12
3. Ekman Spiral . . . 17
4. Resolution in Reanalysis products . . . 29
5. Schematic of Arakawa C-grid and method . . . 34
6. Mean ASV cross sections 1/4° . . . 41
7. Mean ASV cross sections 1/12° . . . 46
8. Mean ASV cross sections 1/4° (NN/INT-method) . . . 49
9. Mean ASV cross sections 1/12° (NN/INT-method) . . . 51
10. Mean ASV cross sections 1/4° Reanalysis products . . . 53
11. Mean ASV cross sections 1/12° Reanalysis products . . . 55
12. Mean ASV vertical profiles . . . 57
13. Performance test . . . 61
14. Seasonal cycle of ASV 1/4° . . . 64
15. Seasonal cycle of ASV 1/12° . . . 67
16. Mean seasonal cycle of ITF transport (2004 - 2006) . . . 69
17. Cross correlation Makassar Strait . . . 72
18. Anomaly time series Makassar Strait . . . 73
19. Mean seasonal cycle of ITF transport (2004 - 2017) . . . 75
20. Correlation maps (0 - 300 m) Makassar . . . 77
21. Regression maps (0 - 300 m) Makassar . . . 79
22. Correlation between transport and sea level gradient . . . 80
23. Transport partition Makassar Strait . . . 82
24. Lead and lag correlation/regression Makassar Strait . . . 83
25. Lead and lag correlation/regression Ombai Strait . . . 85
26. Lead and lag correlation/regression Timor Passage . . . 86
27. Correlation (∇p, V(z)) Makassar Strait . . . 88
28. Density and pressure gradient (entrance and exit region) . . . 89
29. Sea Level Anomalies Scaling Check . . . 90
30. Mean sea level anomalies ENSO . . . 91
31. Lead and lag correlations ENSO Makassar Strait . . . 92
32. Correlation between transport and ENSO . . . 93
33. Transport anomalies Luzon and Mindanao Strait . . . 95
34. Mean ASV vertical profiles ENSO . . . 96
35. Conservation of volume . . . 98
36. Mean ASV: Reanalysis Products - REANA Mean Makassar Strait . . . 116
37. Mean ASV: Reanalysis Products - REANA Mean Lombok Strait . . . 117

38. Mean ASV: Reanalysis Products - REANA Mean Ombai Strait 118
39. Mean ASV: Reanalysis Products - REANA Mean Timor Passage 119
40. Mean ASV cross sections Reanalysis products Makassar Strait 120
41. Mean ASV cross sections Reanalysis products Lombok Strait 121
42. Mean ASV cross sections Reanalysis products Ombai Strait 122
43. Mean ASV cross sections Reanalysis products Timor Passage 123
44. Correlations maps Ombai Strait 124
45. Correlations maps Timor Passage 124

1. Introduction

The waters and islands between the Pacific and the Indian Ocean form a geographical and oceanographical unit. Geographically the region is part of Southeast Asia, but oceanographically the waters are part of the Pacific Ocean, where they also originate.
The Indonesian Seas are the primary low latitude connection between the global oceans that facilitate the transport of heat and freshwater from the Pacific to the Indian Ocean. This connection is known as the Indonesian Throughflow (Wyrtki, 1961), and it is part of the upper branch of the global ocean conveyor belt. The ITF consists of numerous narrow channels, connecting seas, and basins of varying sizes and depths that make their way through the Indonesian Archipelago's complex bathymetry (Fig. 1). Notable Indonesian Seas include the Java Sea, the Flores Sea, the Banda Sea, the Timor Sea, and the Arafura Sea. Please refer to Fig. 1 for geographical guidance.

Two western boundary currents prevail at the entrance of the Indonesian Seas in the equatorial western Pacific: the North Pacific Mindanao Current (Schönau et al., 2015) and the South Pacific New Guinea Coastal Current (New Guinea CC. in Fig. 1) (Cresswell, 2000). The Mindanao Current is a branch of the Pacific North Equatorial Current (NEC) (Qui and Lukas, 1996), that is driven by easterly trade winds (Schott, 1939). The second branch of the NEC feeds into the Kuroshio current (Qui and Lukas, 1996; Yu et al., 2007) flowing poleward. The resulting NEC bifurcation latitude undergoes a seasonal cycle and reaches its most northern point in November, and shifts southward during summer (Wyrtki, 1979; Qu and Roger, 2003; Tan and Zhou, 2018). Correlation analyses suggest that the bifurcation latitude is highly correlated with the ENSO phenomenon (Wang and Hu, 2006). The western boundary currents collide and form the ITF as well as the retroflections that feed the North Equatorial Counter Current (NECC) (Wyrtki and Kendall, 1967). Subsequently, North Pacific upper thermocline waters make their way through the Sulawesi Sea into Makassar Strait (250 km), which already accounts for 80% of the ITF (Gordon, 2005). The flow within Makassar Strait is influenced by a large shelf on the western side. Therefore most of the transport occurs within the 45 km wide Labani Channel, situated to the east. After transiting Makassar Strait, water masses either enter the Banda Sea through the Flores Sea or directly exit into the Indian Ocean via the shallow Lombok Strait (35 km) (Boy, 1995; Sprintall et al., 2009). The bulk of the Makassar transport runs eastward into the Banda Sea (Gordon and McClean, 1999). A smaller fraction of North Pacific waters, but mainly denser South Pacific water masses, enter the Indonesian Seas via the Maluku or Halmahera Sea (Wattimena et al., 2018; Yuan et al., 2022). By way of the Lifamatola Passage (van Aken et al., 2009), these water masses enter the Banda Sea, where denser South Pacific water masses and North Pacific upper waters mix. Water masses undergo extensive mixing due to tidal mixing and air-sea exchanges (Ffield and Gordon, 1992; Hautala et al., 1996). From the Banda Sea, the ITF enters the Indian Ocean through small gateways along the Nusa Tenggara island chain (Godfrey, 1996), but mainly through Ombai Strait (37 km) (Molcard et al., 2001; Sprintall et al., 2009) and Timor Passage (160 km) (Molcard et al., 1996; Sprintall et al., 2009). The major outflow passages Lombok, Ombai, and Timor feed fresh water masses into the westward flowing South Equatorial Current (SEC) (Gordon et al., 1997). Hence, the Indonesian Throughflow is responsible for the transport of freshwater and heat into the Indian Ocean (Piola and Gordon, 1984; Vranes et al., 2002; Potemra et al., 2003).

During boreal winter, when the NEC bifurcation latitude shifts northward (Wang and Hu, 2012), the consequently increased transport through Luzon Strait (320 km) and the associated South China Sea (SCS) throughflow (Fig. 1) play an important role (Gordon et al., 2012). The Luzon Strait is located between Taiwan and Luzon (Philippines). The Island Rule theory (Godfrey, 1989) states that the ITF transport is out-of-phase with the SCS throughflow. Using analysed wind data and a high-resolution general circulation model Qu et al. (2005) have shown that Pacific waters enter the SCS through Luzon Strait. Afterward, part of the water resumes into the Java Sea and circles back to the Pacific through Makassar Strait. This circulation strongly depends on the El Niño Southern Oscillation (ENSO), and we will address this in Chapter 5.3. Accordingly, water masses from the SCS contribute to the ITF via the shallow Karimata Strait into the Java Sea (Susanto et al., 2013) and through Sibutu Passage into the western Sulawesi Sea (Gordon et al., 2012). The SCS throughflow carries water masses with low salinity, which is a result of the high precipitation rate over the SCS and river discharge (Fang et al., 2009; Qu et al., 2009). The SCS flow through the shallow Karimata Strait strongly depends on the prevailing monsoon winds with the flow towards the Java Sea during boreal winter and decreased transport toward the SCS during boreal summer (Yan et al., 2019). The transport through Sibutu Passage (Li et al., 2019) is less influenced by wind stress at the surface but strongly connected to the flow through Luzon Strait (Gordon et al., 2012). Apart from being influenced by the monsoon phases, Luzon Strait and hence the SCS throughflow exhibit an ENSO relationship (Qu et al., 2004; Wang et al., 2006) that originates in the high correlation between the NEC bifurcation and ENSO events (Wang and Hu, 2012).

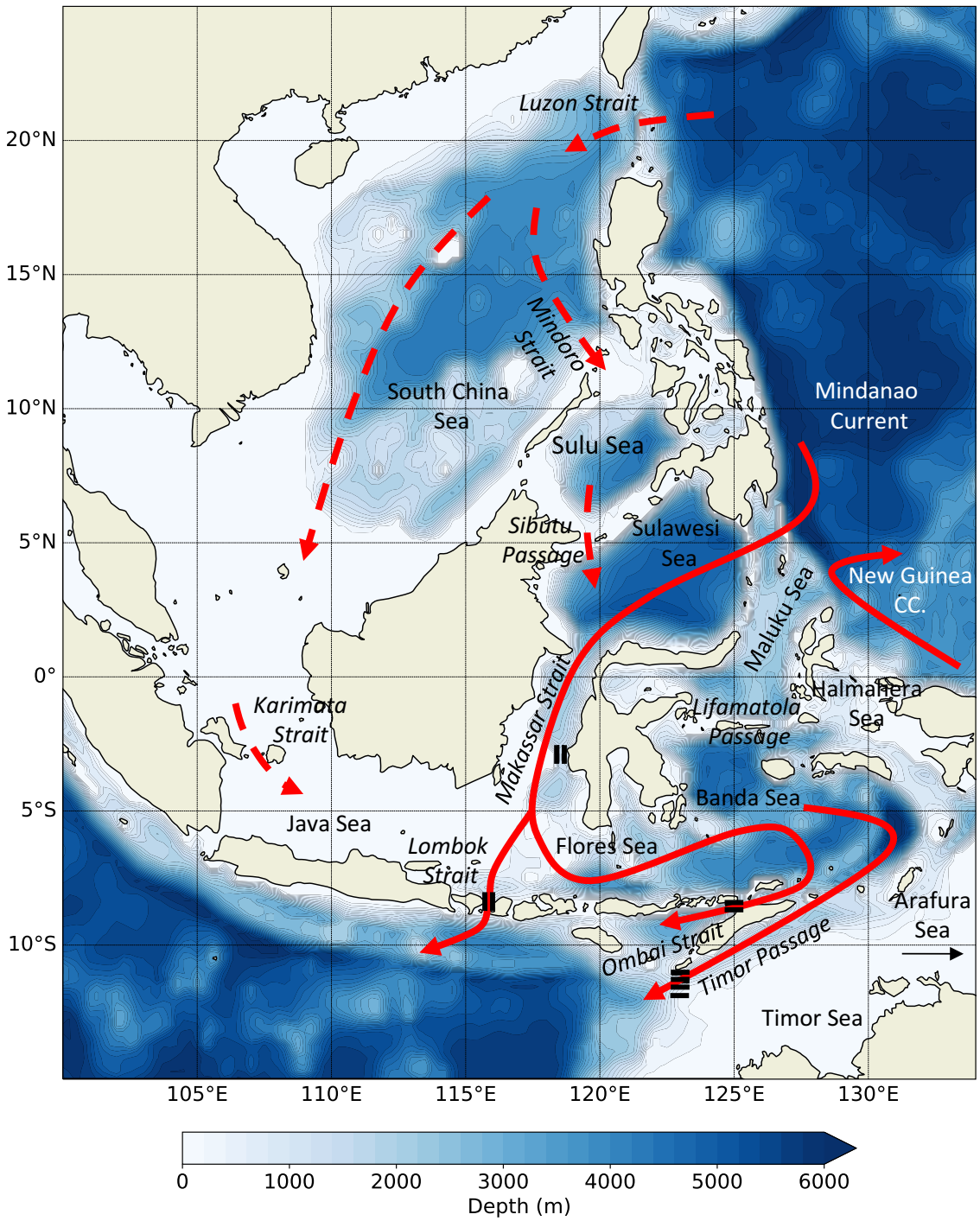

Figure 1: Area of interest: the Indonesian Archipelago. Solid red arrows (dashed red arrows) illustrate a schematic of the Indonesian Throughflow (South China Sea Throughflow). Black vertical and horizontal lines indicate mooring sites during the INSTANT field program (2004-2006). Exact locations can be found in Tab. 1.

The ITF displays fluctuations on a broad range of time scales, from decadal climate variability and its connection to the Pacific Decadal Oscillation (PDO) (Nieves et al., 2015; Ummenhofer et al., 2017), up to interannual time scales and its connection to the El Niño Southern Oscillation (ENSO) (Mayer et al., 2018; Mayer and Alonso Balmaseda, 2021) or

the Indian Ocean Dipole (IOD) (Potemra and Schneider, 2007; Pujiana et al., 2019). On smaller time scales, the Madden Julian Oscillation (MJO) (Nieva Tamasiunas et al., 2021) and the monsoon phases (Clarke and Liu, 1993; Masumoto and Yamagata, 1996) influence the behaviour of the ITF. The mean seasonal cycle of the ITF transport is dictated by trade winds over the western Pacific and reversing wind patterns tied to the Australian-Indonesian monsoon, as first hypothesised by Wyrtki (1987). Together they uphold an interocean pressure gradient between the western Pacific and the eastern Indian Ocean that regulates the ITF. More recent studies have shown that a geostrophic balance prevails in these straits (Potemra et al., 2002), with Pacific winds controlling the pressure in the western tropical Pacific, the ITF's entrance region, while Indian Ocean winds control the pressure in the ITF's exit region, the eastern Indian Ocean (Potemra, 1999).
The Australian-Indonesian monsoon (Wheeler and McBride, 2005) is the southern hemisphere counterpart of the northern hemisphere Asian monsoon. Monsoon phases are accompanied by a pronounced seasonal cycle in the wind regime and monsoonal precipitation rates in the region between Indonesia and Australia. During boreal winter (Fig. 2a), northwesterly winds prevail, whereas the wind regime exhibits a stronger and southeasterly component during boreal summer (Fig. 2b). The nomenclature of monsoon phases is consistent with their corresponding wind regime. Throughout the time of the southeast monsoon (Fig. 2b), southeasterly winds blow along the coast of Sumatra, Java, and the Nusa Tenggara island chain, and this, by definition of the Ekman transport (Ekman, 1905), pushes water masses offshore (Masumoto and Yamagata, 1996). This is indirectly highlighted by the sudden increase in sea level anomalies (SLA) at some distance from the coast. Subsequently, coastal upwelling ensues, resulting in a local mean sea level decrease south of the islands. This increases the interocean pressure gradient towards the Indian Ocean and consequently favors a stronger southward ITF transport during the southeast monsoon. During boreal winter, when the northwest monsoon (Fig. 2a) dominates, the opposite holds true: northwesterly winds approach the coast of Java and Sumatra, causing an increase in mean sea level, thus yielding a suppressed southward- or even northward-directed transport. This behaviour suggests that we can understand the seasonal cycle of ITF transport by studying the interocean pressure gradient between the western Pacific and the eastern Indian Ocean. The interaction between the ITF and the variously mentioned climate phenomenons reflects its connection to the larger scale ocean and the climate system. Therefore, monitoring the ITF is highly relevant.

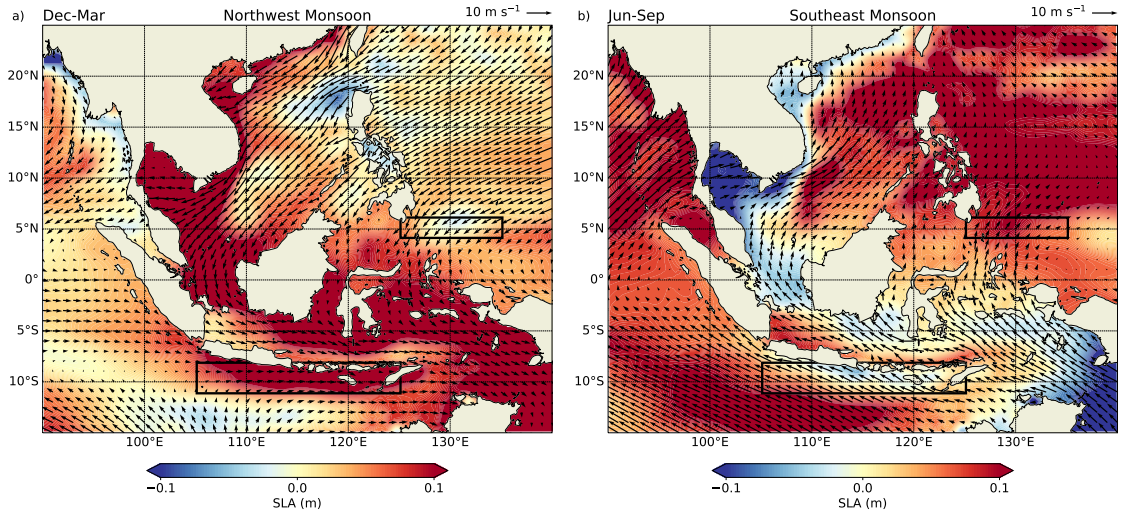

Figure 2: Seasonal averages of sea level anomalies during the two main Australian-Indonesian monsoon phases, the a) northwest monsoon (December-March) and b) southeast monsoon (June-September), inferred from satellite-retrieved data between 2004 and 2017. Black arrows represent the corresponding wind regime with the legend in the top right corner. Black boxes indicate the areas used to determine the pressure gradient (sea level gradient) between the western Pacific and the eastern Indian Ocean.

1.1. Monitoring the ITF

To this day, the Indonesian Seas are counted among the areas where observations are temporally and spatially sparse (Sprintall et al., 2019).
One of the first oceanographic expeditions covering parts of the the Indonesian Seas included the Challenger expedition in 1874 (Willemoes-Suhm, 1874), the Gazelle expedition in 1875 (Schleinitz, 1889) and the Siboga expedition in 1899-1900 (Tydeman, 1902) with special focus on Indonesia. The expeditions provided the first bathymetric map of the area, temperature and salinity measurements, and deep sea soundings. The mission of the Snellius Expedition (van Riehl, 1930) in 1929/1930 was to obtain a three-dimensional description of the water masses in the eastern Archipelago using a model, namely, the Meteor Expedition model. The expedition did not only cover the Indonesian Seas, but also the Atlantic Ocean. However, fundamental differences between the Atlantic Ocean and the Indonesian Seas were not taken into account or perhaps unavoidable at that time, which led to unfeasible data output. It was later established that monsoon-affected regions require at least two expeditions during different seasons. Nonetheless, the results of the expedition included a complete description of the bathymetry and the circulation of deep sea waters. Between 1928 and 1941, Japanese research ships undertook numerous expeditions, mainly covering the western Pacific and the South China Sea (Wyrtki, 1961). From 1949 onwards, merchant ships increased the amount of available information on oceanographic conditions by measuring currents, temperature, and wind. Aside from that, hydrographic offices deliver useful information on climate, local effects and tidal currents. Towards the end of the 20th century, various institutes situated in the area mainly focused on biological research and fisheries (Council, 1957).
Because the transport through Makassar Strait accounts for approximately 80% of the ITF, measuring the integrated transport within Makassar Strait captures the ITF efficiently. Obtaining a time series of measurements, including currents, temperature, and pressure within Makassar Strait, was the goal of the USA Arlindo (Arus Lintas Indonesia) Circulation

Project between 1996 and 1998 (Susanto and Gordon, 1998). The Makassar transport was measured using two moorings, deployed within Labani Channel at approximately 3°S, yielding a transport of -9.1 Sv as determined by Susanto and Gordon (2005). The Arlindo Project covered the strong El Niño event in 1997/98.
In more recent years, numerous monitoring programs captured characteristics of the ITF, including its connection to the Pacific, the individual Indonesian Seas, and outflow regions. The programs covered at most one year-long mooring deployments at different times and depths in different straits. An exception is the IX1 XBT transect (Liu et al., 2005, 2015) between Australia and Indonesia, which provides decade-long estimations of the geostrophic transport of the ITF.
The greatest disadvantage in recent measurement programs is the scarcity of temporal accordance between the data sets. That is why the execution of a multiyear program, simultaneously covering the major inflow and outflow passages of the ITF, provided unprecedented information. As part of the INSTANT (International Nusantra Stratification and Transport) Field Program (Sprintall et al., 2004), an array of 11 moorings were deployed over a three-year period from 2003 to 2006. Between June and July 2005, the moorings were serviced and redeployed. The moorings were designed to measure in situ velocity, temperature, pressure, and salinity profiles using several different instruments. The choice of mooring location was guided by the pathways of the major inflow passages of Makassar Strait and Lifamatola Passage and the main outflow passages of Lombok Strait, Ombai Strait, and Timor Passage. Usually, deep water constrictions are chosen to anchor the moorings to the sea floor. Observations and results from INSTANT in Makassar Strait are discussed by Gordon et al. (2008). Sprintall et al. (2009) focus on the three major outflow passages and find mean integrated transport estimates of -2.6 Sv in Lombok Strait, -4.9 Sv in Ombai Strait, and -7.5 Sv in Timor Passage. Adding the values together results in a total outflow of -15.0 Sv. The estimated transport through Makassar Strait yields -11.6 Sv, as found by Gordon et al. (2008). Fig. 1 shows a schematic of the Indonesian Throughflow pathways and marks the mooring locations in each strait. The exact locations and deployment periods are listed in Table 1.
Funded by the National Oceanic and Atmospheric Administration (NOAA), the Makassar West mooring was redeployed between December 2006 and August 2011 and from August 2013 to August 2017 (Tab. 2). The two-year measuring gap occurred due to logistical reasons. Gordon et al. (2019) find an estimated transport of -12.5 Sv between 2004 and 2017 in 0-760 m. The extension of the time series offers possibilities to investigate connections between the ITF and larger-scale ocean systems.
State-of-the-art ocean observations include Expendable BathyThermographs (XBTs), Mechanical bathythermographs (MBT), Conductivity-Temperature-Depth-Sensors (CTDs), moorings, and Argo floats. The Argo international program (Argo, 2000) was launched in 2000 and has since increased data availability in the global oceans immensely. However, a major drawback is given by the fact that Argo floats do not cover the ITF area because it is to shallow and thus not compatible with their profiling depth (2000 m). The aforementioned instruments mainly provide profiles of temperature, salinity, and velocity.

Table 1: Name, location and deployment period of each mooring employed during the INSTANT (International Nusantra Stratification and Transport) field program (2004-2006).

	Mooring	Location	Deployment Period
Makassar	West	2°51'S, 118°27'E	January 2004 - November 2006
	East	2°51'S, 118°37'E	
Lombok	West	8°26'S, 115°46'E	January 2004 - June 2005
	East	8°24'S, 115°53'E	January 2004 - December 2006
Ombai	North	8°24'S, 125°0'E	January 2004 - December 2006
	South	8°32'S, 125°3'E	August 2003 - December 2006
Timor	Roti	11°9'S, 122°46'E	January 2004 - December 2006
	Sill	11°16'S, 122°51'E	December 2003 - December 2006
	South Slope	11°22'S, 122°57'E	December 2003 - December 2006
	Ashmore	11°31'S, 122°58'E	December 2003 - December 2006

Table 2: Name, location and deployment period for the extended MITF (Monitoring the Indonesian Throughflow) field program (2006-2017).

	Mooring	Location	Deployment Period
Makassar	West	2°51'S, 118°28'E	December 2006 - August 2011 August 2013 - August 2017

In this work, we investigate the performance of various Reanalysis products in a geographically complex area, i.e., the Indonesian Archipelago, by comparing them to specially preprocessed observational data. Here, we aim to construct temporally consistent and uniformly gridded data sets in Makassar Strait, Lombok Strait, Ombai Strait, and Timor Passage. Several different methods will be applied in order to study spatial and temporal differences. Sprintall et al. (2009) and Gordon et al. (2008) serve as a guideline throughout this study. Furthermore, we assess the impact of the Australian-Indonesian monsoon and ENSO on the seasonal cycle of the Indonesian Throughflow. We demonstrate their relations by employing various correlation-based techniques. With respect to ENSO, the influence of the South China Sea throughflow is of importance. The thesis is structured as follows: Chapter 2 contains the theoretical background where general physical characteristics of the oceans are introduced. Moreover, the chapter provides an introduction to geostrophic flow in oceans with a special focus on the dynamics of circulation within the Indonesian Seas as proposed by Wyrtki (1961). We complete the theoretical background with a brief treatment of equatorial waves, particularly eastward propagating Kelvin waves and westward propagating Rossby waves. Chapter 3 introduces the two main research questions. Observational instruments and their output from the INSTANT and MITF programs are discussed in Chapter 4. Furthermore, we introduce the Reanalysis products and comment on the preprocessing methods, as well as further methods used throughout this study. The results are analysed in Chapter 5. In Chapter 6, we conclude our main findings and provide an outlook on possible continuations.

2. Physical characteristics of the ocean

Ocean and atmosphere, both stratified fluids, behave similarly in many ways. Nonetheless, there are some notable differences. Except for the Southern Ocean, all oceans are bounded by land masses, whereas the atmosphere has no bounds. In addition, water is almost incompressible and while the ocean serves as a source of latent heat for the atmosphere, the atmosphere is unable to return the favor. Atmospheric and ocean circulation are subject to different processes in which they are forced. Convection heats the atmosphere from below, whereas the ocean is influenced by the atmosphere at the surface and convection arises through buoyancy loss from the atmosphere. A crucial force, which only the ocean experiences, is the wind exerting stress on its surface. Hence, we can distinguish between wind-driven and buoyancy-driven circulations. The following two sections are based on the ocean and its circulation chapter by Marshall and Plumb (2007).

Contrary to the atmosphere, the density of seawater varies little, but these variations cannot be neglected. Density depends on temperature T, salinity S and pressure p, $\rho = \rho(T, S, p)$. The dependence on pressure is however oftentimes neglected. Calculating the difference between the actual density and a reference value ρ_{ref} yields the density anomaly σ

$$\sigma = \rho - \rho_{ref}, \tag{1}$$

where ρ_{ref} is assumed to be 1000 kg/m^3. Properties such as temperature, salinity and density exhibit substantial vertical gradients near the surface, rather than towards the ocean abyss, where vertical gradients strongly decrease and horizontal gradients almost vanish. The area of strong vertical gradients is referred to as the thermocline, reaching depths of 600 m in mid-latitudes and about 100-200 m in low latitudes. The thermocline is bounded by the overlying mixed layer ranging between depths of 50-100 m. The mixed layer is in direct contact with the atmosphere and therefore agitated by wind and convection, causing it to maintain a relatively homogeneous structure. The ability of the mixed layer to respond promptly to changes in atmospheric forcing sets it apart from the interior ocean. The interior ocean displays alterations on interannual to centennial time scales, while the mixed layer responds to seasonal, inter-annual and even diurnal changes.

2.1. Geostrophic flow

Like the atmosphere, the ocean is a stratified fluid and thus the same basic equations are valid. Accordingly, the geostrophic balance in the ocean can be derived. The horizontal momentum equations are given by

$$\begin{aligned} \frac{Du}{Dt} + \frac{1}{\rho_{ref}}\frac{\partial p}{\partial x} - fv &= F_x \\ \frac{Dv}{Dt} + \frac{1}{\rho_{ref}}\frac{\partial p}{\partial y} + fu &= F_y, \end{aligned} \tag{2}$$

where u and v represent, respectively, zonal and meridional velocity components, f is the Coriolis parameter and $F_{x,y}$ denotes the wind stress at the surface. The surface wind stress is given by

$$F_{x,y} = \frac{1}{\rho_{ref}} \frac{\partial \tau_{x,y}}{\partial z}, \tag{3}$$

where $\tau_{x,y} = (\tau_x, \tau_y)$ represents the horizontal stress vector. Thus, the vector $\vec{F} = (F_x, F_y)$ represents the vertical transport of horizontal momentum by friction on the earth's surface and serves as an important driver for ocean currents (Marshall and Plumb, 2007; Hantel, 2013). The physical unit of $\vec{F}$ is Pa = N/m^2, consequently $\vec{F}$ represents a force. $\vec{F}$ is transferred by turbulent mixing and decreases with depth. The layer above $\tau = 0$, where the stress has vanished, is called the Ekman layer. To obtain the net transport due to wind stress, we subtract the geostrophic component from the (stationary) momentum equation (Eqs. 2) and obtain the equation for ageostrophic flow $\mathbf{v}_{a,g}$

$$f\hat{\mathbf{z}} \times \mathbf{v}_{a,g} = \frac{1}{\rho_{ref}} \frac{\partial \tau_{x,y}}{\partial z}, \tag{4}$$

where $\hat{z}$ represents the vertical unit vector. Multiplying Eq. 4 with ρ_{ref} and integrating from the surface $z = 0$ where $\tau = \tau_{wind}$, to a depth z yields

$$f\hat{\mathbf{z}} \times \mathbf{M}_{ek} = \tau_{wind}, \tag{5}$$

where

$$\mathbf{M}_{ek} = \int_z^0 \rho_{ref} \mathbf{v}_{a,g} \, \mathrm{d}z \tag{6}$$

is the lateral mass transport over the Ekman layer. Using Eq. 4 we can rewrite Eq. 6 to give

$$\mathbf{M}_{ek} = \frac{\tau_{wind} \times \hat{\mathbf{z}}}{f}. \tag{7}$$

Eq. 7 is an important result, indicating that the mass transport of the Ekman layer is perpendicular (to the right in the northern hemisphere) to the surface wind stress (Fig. 3). Thus, alongshore winds can cause onshore or offshore transport. Ekman (1905) demonstrated that the orientation of the horizontal velocity vectors in the Ekman layer, typically 10-100 m, follows that of a spiral (Fig. 3). Therefore, the effects of the wind impact the near-surface area.

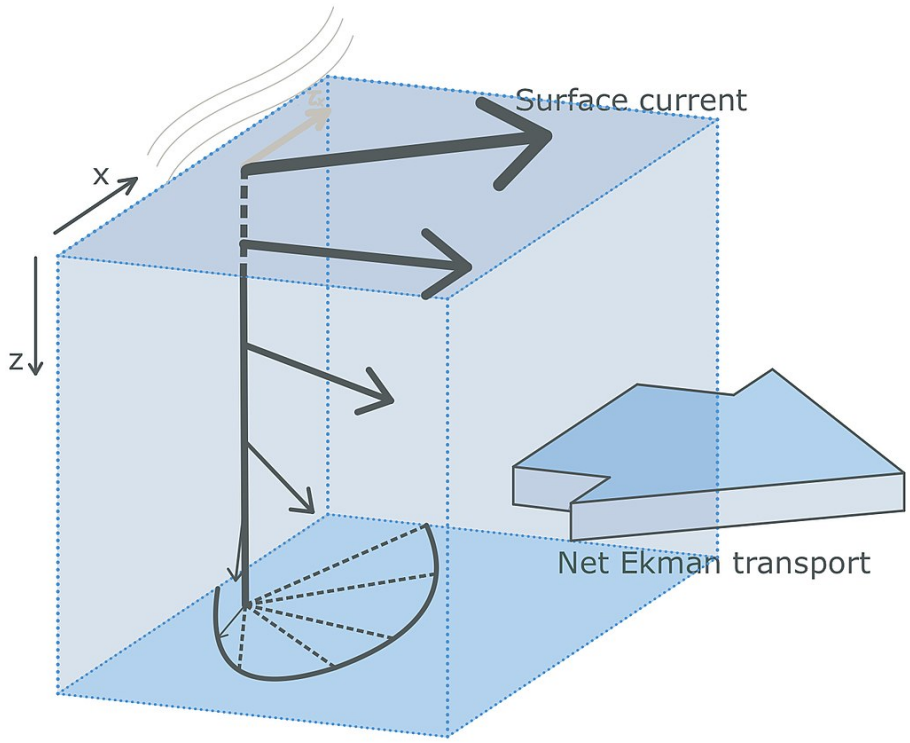

Figure 3: Schematic of the Ekman layer in the northern hemisphere where zonal wind stress τ_x gives rise to Ekman surface currents (45° to the right). Vertically-averaged net Ekman transport is directed perpendicular (90° to the right) to the wind stress (Wikipedia, 2021).

Back to the initial equations, the hydrostatic balance in terms of the density anomaly σ reads

$$\frac{\partial p}{\partial z} = -g(\rho_{ref} + \sigma). \tag{8}$$

Note again that ρ_{ref} is a constant reference value with anomalies σ caused by temperature and salinity variations, and g ($= 9.81$ m/s^2) represents the acceleration of the earth. Integrating Eq. 8 from the sea surface η to a depth z while assuming constant density yields

$$p(z) = p_s + \int_z^\eta g\rho \, \mathrm{d}z = p_s + g\langle\rho\rangle(\eta - z), \tag{9}$$

where p_s represents the atmospheric surface pressure and $\langle\rho\rangle$ is the mean density in a water column determined by η and z. Focusing on the near-surface region ($z = z_0$), where variations of density are negligible, so that $\rho = \rho_{ref}$, Eq. 9 becomes

$$p(z_0) = p_s + g\rho_{ref}(\eta - z_0). \tag{10}$$

Contrary to the atmosphere, pressure increases linearly towards the ocean bed. Note that the third term in Eq. 10 ($g\rho_{ref}z_0$) is dynamically inert, since it does not exhibit horizontal fluctuations. Dynamical features are linked to horizontal fluctuations in the

free surface height η and interior density anomalies σ that vary with temperature and salinity.

Using conventional values for characteristic velocity (U = 0.1 m/s) and length (L = 2 $\times 10^6$ m) scales and the Coriolis parameter ($f = 10^{-4}$ s^{-1}), one obtains a Rossby number of $R_o = 10^{-3}$. With such a small Rossby number ($R_o = 10^{-1}$ in the atmosphere), the effects of planetary motion are substantial, allowing the use of the geostrophic approximation for the internal ocean and away from the equator.
Assuming stationarity and neglecting wind shear, and using the hydrostatic equation (Eq. 9), Eqs. 2 provide the geostrophic balance

$$\mathbf{v}_{g,s} = \frac{1}{f\rho_{ref}}\hat{\mathbf{z}} \times \nabla p = \frac{g}{f}\hat{\mathbf{z}} \times \nabla \eta. \tag{11}$$

The appearance of geostrophic balance calls for a pressure gradient force that balances the Coriolis force. The pressure gradient force is given by a tilt in the free surface height η. Therefore, pressure gradients can be replaced by surface elevation gradients: $(\partial p/\partial x, \partial p/\partial y) = g\rho_{ref}(\partial \eta/\partial x, \partial \eta/\partial y)$. The geostrophic balance connects the dynamical part of hydrostatic pressure to the flow field.

Below the near-surface region ($z = z_1$) variations of density are no longer negligible. Integrating Eq. 9 and disregarding atmospheric pressure variations yields horizontal pressure variations of

$$\hat{\mathbf{z}} \times \nabla p = g\langle\rho\rangle\hat{\mathbf{z}} \times \nabla \eta + g(\eta - z)\hat{\mathbf{z}} \times \nabla\langle\rho\rangle. \tag{12}$$

Thus, the geostrophic balance at depth reads

$$\begin{aligned}
\mathbf{v}_g &= \frac{1}{f\rho_{ref}}\hat{\mathbf{z}} \times \nabla p \\
&= \frac{g}{f\rho_ref}[\langle\rho\rangle\hat{\mathbf{z}} \times \nabla \eta + (\eta - z)\hat{\mathbf{z}} \times \nabla\langle\rho\rangle] \\
&\simeq \frac{g}{f}\hat{\mathbf{z}} \times \nabla \eta + \frac{g(\eta - z)}{f\rho_{ref}}\hat{\mathbf{z}} \times \nabla\langle\rho\rangle,
\end{aligned} \tag{13}$$

with $\langle\rho\rangle \simeq \rho_{ref}$. Eq. 13 is determined by two terms: one is linked to variations in the free-surface height $\nabla\eta$, and the other one is linked to internal ocean density gradients $\nabla\langle\rho\rangle$. Assuming a constant ocean density, the second term in Eq. 13 would disappear and the deep-water geostrophic balance would equal the one at the surface (Eq. 11). In reality, currents and pressure gradients decrease with depth and the two terms in Eq. 13 balance each other. The second term associated with ocean density gradients states, that $\mathbf{v}_g$ varies with depth if horizontal density gradients exist. Subsequently, horizontal variations in free-surface height do not imply geostrophic flow at greater depths and as already mentioned, current velocities decrease at depth. To summarise, the free surface height η, or, in other words the sea level anomalies, are a proxy for pressure anomalies near the surface. The flow response would be the same everywhere only in the barotropic case, i.e., when the horizontal pressure gradient does not vary with depth.

2.2. Sea Level Balance in Ocean Models

The quantity η, which we referred to as the free-surface height until now, is basically the height of the sea surface relative to the geoid. Based on the hydrostatic equation (Eqs. 8) and the relation between $\nabla\eta$ and ∇p ($\nabla p = g\rho_{ref}\nabla\eta$), Storto et al. (2019) define the evolution of sea level anomalies in ocean models as follows

$$\eta = \eta_a + \eta_s + \eta_b = \frac{\overline{p_a} - p_a}{g\rho_{ref}} - \frac{1}{\rho_{ref}} \int_z^\eta \sigma(T, S)\ \mathrm{d}z + \frac{p_b}{g\rho_{ref}}, \tag{14}$$

where η_a denotes the atmospheric pressure term, η_s is the steric component and η_b indicates the mass component term. η_a is defined by variabilities in atmospheric pressure p_a around the mean atmospheric pressure $\overline{p_a}$. The effect of the atmospheric pressure term on η is small and often neglected. The steric contribution η_s is estimated from the vertical integral of the density anomaly σ and arises due to the expansion and contraction of water columns, i.e., variations in density. Positive sea level anomalies correspond to warmer and fresh water masses, whereas negative sea level anomalies conform to cool and salty water columns. The variations in density within a water column due to temperature and salinity variations are referred to as steric effects. As already mentioned in section 2, density depends on the pressure as well but is oftentimes neglected and thus not considered in Eq. 14. Steric effects account for the largest contribution to sea level anomalies in the tropics. In this study, all models are based on the NEMO ocean model and therefore adopt the Boussinesq approximation (Boussinesq, 1903) to represent the steric component of the global mean sea level. This implies the conservation of volume rather than mass and leads to an underrepresentation of the steric effect (Greatbatch, 1994) that must be considered. The last component, η_b, depends on changes in the ocean bottom pressure p_b and arises from changes in water mass within a water column while assuming a constant density ρ_{ref}. Such changes result from, e.g., expansion and melting of continental ice, upwelling and downwelling (Ekman-transport), and barotropic effects.

2.3. Dynamics of Circulation

The integrated volume transport V [Sv = 10^6 m^3/s] specifies the amount of water that is transported by the currents through a cross-sectional area and is given by

$$V = \int_{dx} \int_{dz} \mathbf{v} \cdot \mathbf{n}\ \mathrm{d}\mathbf{x}\ \mathrm{d}\mathbf{z}, \tag{15}$$

where $\mathbf{v}$ represents the current velocity, $\mathbf{n}$ is the vector normal to the strait and $\mathbf{x}$ and $\mathbf{z}$ form the area of the cross section. The vector $\mathbf{n}$ is needed, because one always deals with the transport normal to the interface. However, Eq. 15 is not able to provide information about the the direction of the transport. Wyrtki (1961) presents a derivation explaining the dynamics of currents within the Indonesian Seas in consideration of the relations between wind, sea level, and transports. In order to mathematically comprehend near-equator circulations within the Indonesian Seas, Wyrtki's treatment of the dynamics of circulation is the subject of the next paragraph.

Wyrtki starts by defining the wind as an external force and the field of mass as an internal force, and the interaction between both forces lead to deformations in the sea surface and subsequently to the onset of currents. The field of mass, the ocean surface topography, and the currents strongly depend on each other, while the wind represents an independent parameter. Therefore, to understand the origin of circulations, the interaction between the former factors must be considered. In oceanography, mass transports and the distribution of currents are of great interest, but it is difficult to derive them from observations. The interactions between the various seas in the Indonesian Archipelago can differ greatly from each other, leading to complications in the determination of transports. However, the equation of continuity can be applied to find some connections.
The stationary horizontal momentum equations form the basis of the theoretical treatment. Neglecting friction, this long-established theory allows for the computation of mass transport. However, the presupposed balance in the momentum equations between pressure gradients and the Coriolis force vanishes near the equator, and the theory fails. For this reason, friction has to be considered in order to counterbalance the pressure gradient. Moreover, friction must balance the constant supply of energy exerted by the wind stress at the surface.

The components of mass transports between the sea surface $\eta = 0$ and a depth z are given by

$$\begin{aligned} M_x &= \int_0^z \rho \; u \; \mathrm{d}z \\ M_y &= \int_0^z \rho \; v \; \mathrm{d}z, \end{aligned} \tag{16}$$

where u and v are the velocity components in the zonal and meridional direction, respectively. The stationary horizontal momentum equations thus result in

$$\begin{aligned} \frac{\partial P}{\partial x} - fM_y + rM_x &= F_x \\ \frac{\partial P}{\partial y} + fM_x + rM_y &= F_y, \end{aligned} \tag{17}$$

where r, the friction coefficient, represents the only undefined quantity. We further define

$$P = \int_0^z p \; \mathrm{d}z \quad \text{with} \quad p = \int_{-\eta}^z \rho \; g \; \mathrm{d}z, \tag{18}$$

where p is the pressure as given by the hydrostatic equation integrated between the free-surface height η and a depth z. Furthermore, the equation of continuity

$$\frac{\partial M_x}{\partial x} + \frac{\partial M_y}{\partial y} = -\rho w_z, \tag{19}$$

where w_z is the vertical velocity in depth z, declares, that the inflowing water masses must be compensated by the outflowing water masses. Using Eqs. 16-19 and given the wind stress $F_{x,y}$ as well as the distribution of mass, we can continue by computing the mass transport M without having to integrate differential equations. We can confirm that the

system has a solution at the equator ($f = 0$) in that the mass transport is determined by the wind stress and the pressure gradient, i.e., the sea level gradient.
As already mentioned, a frequent assumption is to regard density as a constant within the layer z. This simplifies Eq. 18 and it follows that

$$p = \rho\ (z + \eta). \tag{20}$$

Thus, Eqs. 17, 18 and 19 become

$$\begin{aligned} \rho g z\ \frac{\partial \eta}{\partial x} - f M_y + r M_x &= F_x \\ \rho g z\ \frac{\partial \eta}{\partial y} + f M_x + r M_y &= F_y, \end{aligned} \tag{21}$$

and

$$\begin{aligned} P &= \rho g z\ (\frac{z}{2} + \eta) \\ \frac{\partial M_x}{\partial x} + \frac{\partial M_y}{\partial y} &= -\rho w_z. \end{aligned} \tag{22}$$

The flow within the straits in the Indonesian Archipelago mostly exhibits unidirectional flow. Hence, integrating the mass transports across a channel with width b and assuming the orientation of the channel along the x-axis yields

$$\int_0^b M_y\ \mathrm{d}y = 0 \quad \text{and} \quad \int_0^b M_x\ \mathrm{d}y = V, \tag{23}$$

because there is no transport across the channel. Provided that the wind stress only depends on the x-component, one attains

$$\begin{aligned} \rho g z\ b\ \frac{\partial \eta}{\partial x} + r \rho V &= b\ F_x \\ \rho g z\ \Delta \eta_y + f \rho V &= b\ F_y, \end{aligned} \tag{24}$$

where $\Delta \eta_y$ is the difference in sea level between both coasts. Eqs. 24 describe the sought connection between wind, transport, and sea level. Furthermore, the equations state that wind stress $F_{x,y}$ directed along the channel causes a transport V in said direction, and its magnitude is regulated by the friction r. Moreover, a slope $\partial \eta / \partial x$ is able to increase the transport along the channel or slow it down to zero if it is acting against the wind. The cross slope $\Delta \eta^y$ is a product of the deflection of transport caused by the Coriolis force.

2.4. Equatorial Waves

The discussion of our results requires a brief introduction to equatorial waves, specifically eastward propagating Kelvin waves and westward propagating Rossby waves. The following section provides a rough overview of this topic, but for more details and a proper derivation,

we refer the reader to Hantel (2013) and Wheeler and Nguyen (2015). Equatorial waves exist on a range of spatial and temporal scales that propagate along the equator. Their existence depends on the restoring forces of the pressure gradient force, the Coriolis force, and gravity. Despite the proximity to the equator, the Coriolis force must be considered. Their theoretical treatment is based on the hydrostatic primitive equations. The linearization of these equations about a basic state, e.g., $u(t,x,y) = \overline{u} + u'(t,x,y)$, and assuming no mean flow $\overline{u} = 0$, yields the shallow water momentum and continuity equations

$$\begin{aligned} \frac{\partial u'}{\partial t} - \beta y v' &= -\frac{\partial \Phi'}{\partial x} \\ \frac{\partial v'}{\partial t} + \beta y u' &= -\frac{\partial \Phi'}{\partial y} \\ \frac{\partial \Phi'}{\partial t} + gH\left(\frac{\partial u'}{\partial x} + \frac{\partial v'}{\partial y}\right) &= 0, \end{aligned} \tag{25}$$

where H is the depth and because $f = 0$ at the equator the Coriolis force ($f = 2\Omega sin(\phi)$ with Ω as the angular velocity of the Earth's rotation and ϕ as the latitude) is considered in the equatorial β-plane $f(y) = f_o + \beta y$. Here, the meridional dependence of the Coriolis parameter is expressed as a Taylor series developed at a distance to the equator y. A thorough derivation of the shallow water equations can be found in Hantel (2013). To solve Eqs. 25, a wave approach in the form of a zonally propagating wave (u', v', Φ') = $\mathrm{Re}(u^o(y), v^o(y), \Phi^o(y))\ e^{i(\kappa x + \omega t)}$ is applied, where k is the zonal wave number and ω is the frequency. The amplitudes of the perturbations, denoted with the superscript o, are functions of y because we will consider boundary conditions in the North and South. Substituting the wave approach into Eqs. 25 yields

$$\begin{aligned} -i\omega u^o - \beta y v^o + ik\Phi^o &= 0 \\ -i\omega v^o + \beta y u^o + \frac{\mathrm{d}\Phi^o}{\mathrm{d}y} &= 0 \\ -i\omega \Phi^o + gH\left(iku^o + \frac{\mathrm{d}v^o}{\mathrm{d}y}\right) &= 0. \end{aligned} \tag{26}$$

We seek a single differential equation by eliminating two unknown functions. The sought-after function is $v^o(y)$ because boundary conditions in the North and South have to be considered. Therefore we continue by eliminating u^o and Φ^o to obtain a second-order differential equation for v^o

$$\frac{\mathrm{d}^2 v^o}{\mathrm{d}y^2} + \left(\frac{\omega^2}{gH} - k^2 - \frac{k}{\omega}\beta - \frac{\beta^2 y^2}{gH}\right)v^o = 0. \tag{27}$$

Taking into account that we are seeking solutions for equatorial waves, boundary conditions are required so that waves decay at large values of y. Eq. 27 is of the form of a quantum harmonic oscillator, thus, the constant part of the coefficient in parentheses has to satisfy

$$\frac{\sqrt{gH}}{\beta}\left(\frac{\omega^2}{gH} - k^2 - \frac{k}{\omega}\beta\right) = 2n + 1 \qquad n = 0, 1, 2, \ldots\ , \tag{28}$$

connecting frequency ω and a wave number k with some positive value of n. On account of the boundary conditions, not all solutions are valid, and a quantization, marked with n, exists. The relation between ω and k is known as dispersion relation. Eq. 28 is a cubic equation and yields three solutions for ω provided that n and k are defined. Combinations of n and k determine the set of solutions for possible Rossby waves. Solutions of Eq. 28 can be studied considering different approximations. At this point, we are interested in the case of low frequencies, where the term ω^2/gH in Eq. 28 vanishes, yielding

$$\omega_{Rossby} \approx \frac{-\beta k}{k^2 + \frac{(2n+1)\beta}{\sqrt{gH}}}, \tag{29}$$

with the respective phase speed c_{Rossby}

$$c_{Rossby} = \frac{\omega_{Rossby}}{k} = -\frac{\beta}{\frac{\beta(2n+1)}{\sqrt{gH}} + k^2}. \tag{30}$$

Waves corresponding to this frequency are called equatorial Rossby waves. Due to the fact that ω and k are of opposite signs, thus providing a negative phase speed, equatorial Rossby waves only propagate westwards.

The second relevant wave class is obtained by setting $v^o = 0$ in Eqs. 25, that is, no flow in the north-south direction and thus no interference with the boundary conditions

$$-i\omega u^o + ik\Phi^o = 0 \tag{31}$$

$$\beta y u^o + \frac{\mathrm{d}\Phi^o}{\mathrm{d}y} = 0 \tag{32}$$

$$-i\omega\Phi^o + gHiku^o = 0. \tag{33}$$

We substitute Φ^o in Eq. 33 with Eq. 31 and obtain the following dispersion relation

$$\omega_{Kelvin} = \sqrt{gH}k, \tag{34}$$

with the corresponding phase speed c_{Kelvin}

$$c_{Kelvin} = \frac{\omega_{Kelvin}}{k} = \sqrt{gH}. \tag{35}$$

Since c_{Kelvin} is independent of frequency, Kelvin waves are non-dispersive, implying that phase and group velocity propagate in the same direction. From Eq. 32 follows the sought differential equation for u^o

$$\frac{\mathrm{d}u^o}{\mathrm{d}y} + \frac{\beta y}{\sqrt{gH}u^o} = 0, \qquad \text{where} \qquad u^o = U^o exp(-\frac{\beta y^2}{2\sqrt{gH}}). \tag{36}$$

The sign of c_{Kelvin}, that is, the direction of motion of the wave, depends on the hemisphere and whether the boundary (coastline) lies to the north or the south. In this study,

Kelvin waves in the southern hemisphere (Indian Ocean) propagating along a northerly located coast (Sumatra, Java), implying $y < 0$ and consequently $c > 0$, thus, eastward propagating waves are of interest.

The idea that the Pacific and Indian equatorial winds provoke variability in the ITF was first discussed by Clarke and Liu (1994). They argued that the Indonesian seas serve as the intersection between two waveguides, connecting westward propagating energy from the Pacific and eastward propagating energy along the coast of Sumatra and Java from the Indian Ocean. Furthermore, they predicted interannual pressure changes in the coastal waveguides and, thus, changes in the ITF transport. Due to the lack of observations, their theory remained unconfirmed back then.
Using a wind-forced Kelvin wave model Sprintall et al. (2000) showed that equatorial Indian Ocean winds contribute to sea level variability along the south coast of Indonesia through to Ombai Strait. Moreover, anomalous wind forcing in the equatorial Indian Ocean leads to the formation of the eastward propagating and surface-confined Wyrkti Jet (Wyrkti, 1973), generating Kelvin waves as a kind of oceanic response (Sprintall et al., 2000). These anomalous wind regimes include monsoon transition phases (April-May and Oct-Nov) and Madden-Julian oscillations (Madden and Julian, 1972), which manifest themselves by westerly wind anomalies in the Indian Ocean, causing alongshore winds on the south coast of Indonesia.
Pacific wind energy likely originates from the transmission of equatorial Rossby waves generated by anomalous wind changes in the central equatorial Pacific (Clarke, 1991; Meyers, 1996). This energy propagates westwards across the tropical Pacific Ocean and contributes to sea level variability in the western Pacific, nearly in phase with ENSO. This way, the interocean pressure gradient experiences variations, and accordingly the ITF transport (Potemra, 1999). A study by Wijffels and Meyers (2004) confirmed the theory from Clarke and Liu (1994), proving that the mean seasonal cycle of sea level can be explained through Kelvin and Rossby waves generated by remote zonal winds along the equator of the Indian and Pacific Ocean.

3. Research Questions

There have been numerous studies covering the dynamics of the Indonesian Throughflow, oftentimes based on in-situ measurements (Arlindo Project, INSTANT, and MITF) and different numerical models. The fact that an appropriate number of observations are available offers the opportunity for comparisons with different Reanalysis products, which aim to investigate the model's capabilities. Simultaneously studying all relevant straits of the ITF in terms of multiple Reanalysis products has been hardly done. After all, near real-time monitoring is only possible with Reanalyses, and in order to employ them, their skills have to be evaluated. On this account, we pursue the following question

1. How well do Ocean Reanalyses depict the intensity of the Indonesian Throughflow?

   The focus lies on the observations, the Reanalysis mean, composed of five Reanalysis products (CGLORS (Storto and Masina, 2016), FOAM (MacLachlan et al., 2015), GLORYS2V4 (Garric and Parent, 2017), ORAS5 (Zuo et al., 2015), and ORAP6 (Zuo et al., 2021)) and a single, but higher resolving product, GLORYS12V1 (Lellouche et al., 2021). The aim of this question is clear it is to assess the skill of Reanalyses within the highly complex bathymetry of the Indonesian Seas by comparison with observations. Furthermore, we try to decipher whether GLORYS12V1 exhibits advantages attributed to its higher resolving grid. Therefore, a strong focus lies on the product's abilities to resolve the bathymetry in such regions with lots of islands and especially those with narrow straits and relatively deep sills (>1000 m). A successful comparison calls for a specially executed preprocessing method created within the scope of this work.

Using the results we obtained while answering the first question, we further view them in a dynamic context. This way, we are able to assess their validity and study the mean seasonal cycle of the ITF by means of observations and Reanalysis products. The introduction demonstrated the relation between pressure gradients ∇p and surface elevation gradients $\nabla \eta$, which is crucial with respect to the next question. The orientation and intensity of the pressure gradient, i.e., the sea level anomaly gradient, between the western Pacific and the eastern Indian Ocean regulate the ITF, which leads us to the second question of

2. How strongly does the Indonesian Throughflow transport depend on large-scale sea level gradients?

   Through the creation of scatter diagrams and correlation maps, we try to establish the correlation between ITF transport and the varying sea level gradient between the entrance and exit region of the throughflow. We mainly focus on Makassar Strait because the extended measurement period (2004-2017) allows for a proper analysis. Within the scope of this question, we discuss the seasonal dependency of ITF transport on the sea level gradient by means of the monsoon phases. A partition of transport into the upper (>300 m) and lower layer (<300 m) simplifies the interpretation of plots and serves to explain the current response in different depths. Furthermore, we seek to understand the behaviour of the ITF during ENSO and the consequential linkage to the SCS throughflow. The approach to understanding this dynamic is, again, based on large-scale sea level gradients.

4. Data and Methods

The following chapter introduces the employed data sets, observations, and Ocean Reanalyses and provides an overview of the applied methods. We start by defining the term mooring and continue with a presentation of the observational instruments used during the INSTANT and MITF programs. Once the observations are covered, we move on to the Reanalysis products. Here, we provide an overview of the employed products and their different components. Preprocessing the raw observational data and reanalysis data is a key element in this thesis and is therefore explained separately in sections 4.3 and 4.4 before moving on to the methods.

4.1. Moorings

Due to the inertia of the oceans, long-term measurements are required to understand processes and changes occurring within the oceans. Since the 1960s, one of the main instruments used to achieve such measurements are moorings (Meindl, 1996). Moored at selected sites around the world's oceans, they provide measurements from the seafloor to the sea surface and, depending on their configuration, information about atmospheric processes close to the surface. Based on their design, one distinguishes between two mooring types: subsurface moorings and surface moorings. A subsurface mooring is a collection of measurement devices mounted to a wire that is anchored to the sea floor and kept upright by buoyant floats, not reaching the sea surface. Surface moorings, on the other hand, consist of surface floats with a downward-hanging wire. The surface floats carry sensors that measure parameters such as wind speed and direction, relative humidity, air temperature, and barometric pressure. The instruments on the wire are mounted at fixed depths and measure the speed and direction of currents, temperature, pressure, and salinity. Both mooring types provide highly reliable and frequent measurements and are able to operate over long periods of time. Since subsurface moorings are less exposed to atmospheric influences, they are able to endure longer deployment periods without maintenance (Toole et al., 2000). During the INSTANT and MITF field programs, only subsurface moorings were deployed.

The subsurface moorings were densely equipped with instruments discussed in section 4.1 in order to resolve the properties of the ITF properly (Cowley et al., 2009). The configurations were similar in all straits, with an upward-looking ADCP that captured the upper layer (0-300 m) and single-point current meters in greater depths. Most current meters are equipped to measure temperature, pressure, and salinity as well. Moreover, instruments measuring only one quantity were also installed, primarily in the upper 300 m. The following section will give an overview of the observational instruments used during the INSTANT project. The Makassar West mooring exhibits a similar structure (Gordon et al., 2019).

Acoustic Doppler Current Profiler (ADCP)

Acoustic Doppler Current Profilers (ADCP) are designed to measure ocean currents with high precision (Institution, 2022; NOAA, 2008). Mounted to a subsurface mooring, these devices can measure the speed and direction of currents at equal intervals all the way up to

the surface or the sea floor, depending on if they are upward or downward looking. The concept of an ADCP is based on the Doppler effect and the assumption that particles suspended in the water are moving at the same speed as the water itself. During the measuring procedure, the ADCP emits high-frequency sound pulses that get reflected by moving particles in the water. Due to the Doppler effect, the received frequency is lower than the emitted frequency if the particles move away from the profiler. Vice versa, a higher frequency is registered if the particles are moving towards the profiler. The difference between the outgoing and incoming frequency is used to determine the speed and direction of the particles and hence the water around them. By tracking the transit time of the sound pulses, the current speed is measured at different depths. The instrument divides the return signal into various depth cells/bins, depending on its maximum measurement range. Each bin represents the average of the return signal for a given period. The number of bins and their length are necessary information and are provided in the data output files.

Acoustic Current Meter (ACM)

Acoustic current meters (ACM) use reciprocal acoustic transmission to measure the velocity and direction of currents (Taniguchi et al., 2021; University Rhode Island, 2021; Falmouth Scientific Inc., 2014). This way, transit times of acoustic pulses transmitted between spatially separated transducers are measured. Commonly, an ACM consists of a set of transducers that are aligned perpendicularly to each other within a frame. A pulsed or continuous acoustic signal of 1 MHz is emitted along four paths, and by measuring the difference between reciprocal transit times of the signal, current velocity and direction can be determined. The differences in time-of-arrival derive from the fact that a sound pulse traveling with the current is faster than one traveling against it. A built-in compass and tilt sensor estimate the direction of the instrument and provide current vector direction. ACMs are often combined with pressure sensors or even a CTD (conductivity, temperature, and pressure) rosette.

Vector Measuring Current Meter (VMCM)

Vector Measuring Current Meters (VMCM) were developed in the 1970s by Weller and Davis (1980) and are used to measure the two horizontal components of velocity. Due to their ability to conduct high-quality measurements in the upper ocean, VMCM sensors are used to evaluate the skill of other current meters (Hosom et al., 1999). A VMCM consists of two orthogonally mounted propellers, each of them measuring the horizontal velocity component parallel to their axis of rotation. The instrument uses a flux-gate compass to determine orientation by detecting the angle of the meridional axis to the magnetic North. Furthermore, a microprocessor facilitates the conversion from X-Y coordinates into geographic coordinates (North-South and East-West). The conversion takes place after each sampling interval (typically one hour), and once a recording interval is completed, the velocity components are averaged and stored (Gilboy et al., 2000).
The sampling interval determines the time during which the instrument records rotations of both propellers. Given the number of rotations in a sampling interval, the average horizontal shift is derived, and the aforementioned averaging yields the velocity.
Intercomparison studies (Halpern et al., 1981) have shown that VMCM sensors exhibit

high measuring accuracy even in steady flow conditions. In addition, VMCMs are able to measure temperature and pressure.

CTD Sensors

In general, CTD Sensors are used to measure conductivity (C), temperature (T), and depth (D) (SeaBird, 2018). Conductivity is used to determine salinity, and depth is a synonym for measuring pressure. However, it is worth mentioning that depth and pressure are two individual quantities and their complex relationship depends on factors such as water density and compressibility. There are two types of CTD Sensors: profiling and moored CTDs. Profiling CTDs take measurements while being lowered from a ship to get a vertical profile of the desired quantity. Moored CTDs, on the other hand, measure water quantities in one depth, providing long-term measurements. In this case, the pressure sensor is often deactivated, assuming that the deployment depth will not change. However, this can be problematic if the instrument is subject to strong mooring blow over. Precise salinity measurements require pressure recordings as well. The company's SeaBird (SBE) (SeaBird, 2016) moored CTDs use special anti-fouling techniques to keep the sensors clean and allow unimpeded measurements.
Two types of SBE instruments, SBE37 and SBE39, were used during the INSTANT program period. Depending on their deployment depth, the instruments measured salinity, temperature, and pressure.

AQUADOPP Single-Point Current Meter (ASCM)

Aquadopp single-point current meters (ASCM) were developed by Nortek in 1999 (Nortek, 2018). Their measuring principle is based on the Doppler effect, and since they require little maintenance and no calibration, long-term measurements are possible. ASCMs emit sound pulses at a certain frequency that is scattered by particles within the water. The scattered signal exhibits a frequency shift that is used to compute the current velocity along each beam. The advantage of transmitting three horizontal beams instead of two beams is the computation of an error velocity that accounts for variability during measurements (Siegel et al., 2008).
The Aquadopp is equipped with a compass and a tilt sensor to determine the orientation of the instrument. Its robust design facilitates deployments in various water bodies and depths. After the termination of the INSTANT program, no manual quality control was required.

Recording Current Meter (RCM)

Recording current meters (RCM) are based on the same principle as single point current meters, the well-known Doppler effect (Aanderaa, 2001). What sets them apart is the RCM's ability to measure temperature, as well as conductivity, and pressure. Current measurements are taken along two orthogonal axes and tilt corrected using an electrolytic tilt sensor. An internal compass determines the instrument's orientation to magnetic North. After each sampling interval, a microprocessor computes averages of current velocities and directions.

4.2. Reanalysis Products

In meteorology, Reanalyses combine model data with historical observational data using data assimilation in order to construct a spatially and temporally continuous data set, describing the past weather and climate (ECMWF, 2020). In oceanography, Ocean Reanalyses represent their equivalent for the state of the ocean. The following section introduces the Reanalysis products that were used throughout this study.

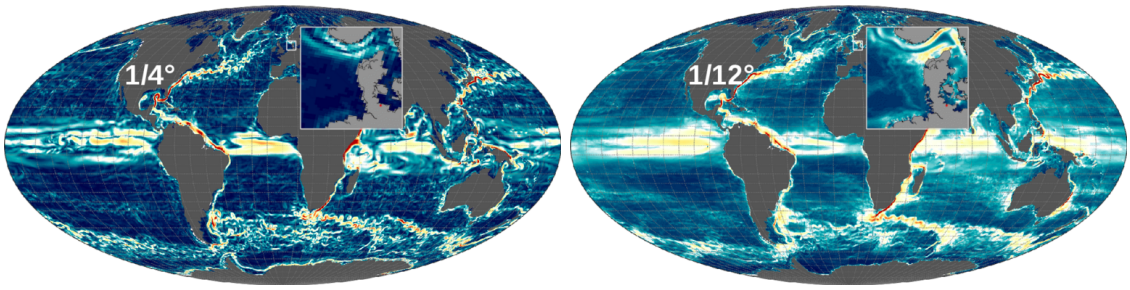

Figure 4: Tripolar grid from ORCA model configurations with a horizontal resolution of (left) $1/4° \times 1/4°$ and (right) $1/12° \times 1/12°$. The horizontal resolution equals, respectively, ∼28 km and ∼9 km at the equator (GEOMAR, 2022).

ORAS5

OCEAN5 is the operational ensemble Reanalysis-Analysis system at the European Centre for Medium-Range Weather Forecasts (ECMWF), providing global ocean and sea ice Reanalysis (Zuo et al., 2015). The OCEAN5s Reanalysis product is the Ocean Reanalysis System 5 (ORAS5), which entails 5 members and provides an estimation of the global ocean state from 1979 to the present. OCEAN5 uses the NEMO ocean model (v3.4) (Madec et al., 2008) in the ORCA025.L75 configuration (Fig. 4), indicating an eddy-permitting horizontal resolution of $0.25° \times 0.25°$ and 75 vertical levels. Thus, the horizontal resolution in the Indonesian Seas is about 28 km. The near-surface vertical resolution amounts to 1 m. The NEMO model is implemented as a tripolar ORCA grid with Arakawa C-grid staggering (Arakawa and Lamb, 1977), where individual variables are computed at different grid points. The tripolar grid computation from ORCA is based on the semi-analytical method from Madec and Imbard (1996). The implementation of a tripolar grid results in the northern hemisphere having two land-based poles, this way, the computation of ocean fluxes remains undisturbed. Regarding the impact of sea ice, the NEMO model is coupled with the Louvain-la-Neuve sea-ice model (LIM2) (Zuo et al., 2019; CMEMS, 2021b).
NEMOVAR (3D-Var Assimilation) (Mogensen et al., 2012) is the operational ocean assimilation system assimilating satellite observations of sea level anomalies, in-situ observations of sub-surface temperature and salinity, as well as sea ice concentration (SIC) and sea surface temperature (SST). The satellite-derived data for SLA is the AVISO (Archiving, Validation, and Interpretation of Satellite Oceanographic (Pujol et al., 2016)) dataset. In-situ observations are extracted from the quality-controlled UK Met Office EN4 datasets (Good et al., 2013), which include data from several instruments: XBTs, MBTs, Moorings, Argo floats, and CTDs. Note that current measurements from mooring buoys are not assimilated. Heat, momentum, and freshwater fluxes from the ECMWF ERA-Interim

Reanalysis product (Dee et al., 2011) are used to force the ocean model using CORE bulk formulas (Large and Yeager, 2004). Since 2015 atmospheric forcing is provided by ECMWFs operational NWP model (Zuo et al., 2019).

ORAP6

The Ocean ReAnalysis Pilot system-6 (ORAP6) is a new global ocean and sea-ice Reanalysis prepared by the OCEAN5 Reanalysis system (Zuo et al., 2021). Since ORAP6 is only the prototype, detailed information about the product is not available yet. Compared to ORAS5, ORAP6 uses different atmospheric forcing and a revised data assimilation system, assimilating the latest observational data sets. The model configuration remains the same as in OCEAN5, featuring a horizontal resolution of $0.25° \times 0.25°$ and 75 vertical levels. Initial evaluations have shown general improvement in comparison with ORAS5.

GLORYS2V4

The Mercator Ocean GLORYS2V4 Reanalysis system is based on the NEMO ocean model (v3.1) in the ORCA025.L75 configuration (Garric and Parent, 2017). LIM2 serves as the sea-ice model, and ERA-Interim Reanalysis products are used to force the system. An additional satellite-based large-scale correction is conducted to help counteract observed biases near the surface. Such bias corrections also account for adaptations in the observing systems. The model assimilates satellite-based SST and SLA data, in-situ observations of temperature and salinity, and sea ice concentration. Data assimilation is performed using a reduced-order Kalman Filter (Kalman, 1960). In order to employ past and future observations, the analysis is not executed at the end of an assimilation cycle but in the middle. This aims to improve the estimation of the ocean and sea-ice state.

GLORYS12V1

GLORYS12V1 is an ocean and sea ice Reanalysis provided by Mercator Ocean (Lellouche et al., 2021) and is the higher resolving version of GLORYS2V4. The system is based on the NEMO model with a horizontal resolution of $1/12°$ ($\sim$9 km at the equator) and 50 vertical levels (Fig. 4). The first 100 m includes 22 levels leading to a vertical resolution of 1 m in the upper levels and 450 m in 5000 m. Employing an ocean and sea ice Reanalysis with a horizontal resolution of $1/12°$ is particularly interesting in areas such as the Indonesian Archipelago, where sea straits are narrow and deep. The ulterior motive is to assess whether GLORYS12V1 can represent ocean parameters more accurately than the $0.25°$ Reanalysis products, especially in more narrow straits.
The ECMWF ERA-Interim atmospheric Reanalysis is used to force the model at the surface. To counteract biases in precipitation and radiative fluxes, a satellite-based bias correction is applied. The assimilation method consists of a reduced-order Kalman filter (Brasseur and Verron, 2006) combined with a 3D-Var scheme assimilating altimeter-derived sea level anomalies, satellite SSTs, sea ice concentration, and in-situ observations of temperature and salinity profiles from the CORA dataset (Cabanes et al., 2013). Another favorable feature of GLORYS12V1 is its ability to resolve inter-basin exchange with high skill.

C-GLORS (v7)

The Euro-Mediterranean Center on Climate Change (CMCC) uses the Global Ocean Physical Reanalysis System (C-GLORS) to replicate the state of the ocean (Storto and Masina, 2016). There are currently two versions available however, only C-GLORS Version 7 was used during this study. C-GLORYSv7 uses an upgraded ocean model version, NEMO-LIM2 3.6, that provides data on the aforementioned ORCA025.L75 grid. The system implements a 3D-Var data assimilation system (OceanVar) with a first guess at the appropriate time (FGAT) that assimilates in-situ profiles of temperature and salinity, altimeter sea level anomalies, SST analyses, and sea-ice concentration. The data assimilation method features an enhanced quality control scheme for observations (Storto, 2016). Furthermore, a nudging scheme assimilates SST on a daily basis (Reynolds et al., 2007). ERA-Interim Reanalysis data provides atmospheric forcing at the surface.

FOAM

The Ocean Reanalysis run at the U.K. Met Office is the Forecast Ocean Assimilation Model (FOAM) (MacLachlan et al., 2015). The system is based on the NEMO ocean model coupled with the Los Alamos sea ice model CICE (Hunke and Lipscomb, 2010), a model that is more consistent with FOAM compared to LIM2. FOAM implements surface forcing from ERA-Interim, and data are provided on a tripolar grid in the ORCA025.L75 configuration, equal to the other Reanalysis products. The model even uses specific parameterizations in the ITF area to account for strong internal tides (Koch-Larrouy et al., 2007). FOAM employs the 3D-Var data assimilation method NEMOVAR, which assimilates in-situ profiles of sub-surface temperature and salinity, altimeter data for sea surface height, and satellite observations for SSTs and sea ice concentration. Bias corrections are applied in the case of SSTs and altimeter data (Waters et al., 2013). Moreover, the model output is used to initialize the coupled ocean–ice–atmosphere seasonal and medium-range forecasting systems. Note again, velocity data in any form is not assimilated, and this holds true for each introduced product.
A summary of the introduced Reanalysis products is given in Tab. 3.

Table 3: Name (institution), resolution (horizontal and vertical), ocean model, forcing and data assimilation method for Reanalysis products.

Product	Resolution	Ocean Model	Forcing	Data Assimilation
C-GLORS (CMCC)	1/4° 75 levels	NEMO	ERA-Interim	3D-Var/FGAT
FOAM (Met Office)	1/4° 75 levels	NEMO	ERA-Interim	3D-Var/FGAT
ORAS5 (ECMWF)	1/4° 75 levels	NEMO	ERA-Interim	3D-Var/FGAT
ORAP6 (ECMWF)	1/4° 75 levels	NEMO	ERA5	3D-Var/FGAT
GLORYS2V4 (Mercator Ocean)	1/4° 75 levels	NEMO	ERA-Interim	Kalman Filter
GLORYS12V1 (Mercator Ocean)	1/12° 50 levels	NEMO	ERA-Interim	Kalman Filter

In the following, we will often refer to the term *Reanalysis mean*. The Reanalysis mean represents the mean over all 1/4° Reanalysis products, including the pilot Reanalysis product ORAP6. Aside from that, C-GLORS, FOAM, GLORYS2V4, and ORAS5 have all been selected to contribute to the Copernicus Marine Service Global Reanalysis Ensemble Product (GREP) (Desportes et al., 2017). GLORYS12V1 with the 1/12° horizontal grid is considered separately.

4.3. Observational Data

Observational data used throughout this thesis were measured during the INSTANT field program from August 2003 to December 2006 and the MITF program from December 2006 to August 2011 and August 2012 to August 2017 (Tab. 1 and 2). The INSTANT raw data sets are available under `http://www.marine.csiro.au/~cow074/index.htm`. The data sets provide, amongst other relevant information, velocity, temperature, salinity, and pressure measurements in various depths. Data from Lifamatola Passage was inaccessible and is not considered in this thesis. The Timor Sill mooring from the first deployment parted early in August 2004, leaving only one instrument at the bottom. Data from the mooring was later recovered and is available to August 2004. During the mooring second deployment, the ADCP only measured in a small number of bins close to the instrument, restricting the available data to ∼300-1900 m.
The extension of the Makassar West mooring data is available under `http://ocp.ldeo.columbia.edu/res/div/ocp/projects/MITF/cm_data/`. The data sets for each deployment period are already preprocessed and gridded, but detailed documentation is not provided. We assume data was handled similarly as described by Gordon et al. (2008). Furthermore, MITF data only extends to about 700 m depth, whereas INSTANT Makassar Strait data extends to ∼1400 m. The single mooring was equipped with an upward-looking ADCP in ∼450 m and an adjacent downward-looking ADCP. Since only the West mooring was active during the MITF program, the velocity data at the East mooring location is estimated using a Linear Regression Model. The model is based on the high correlation in velocity (r = 0.98) between East and West mooring during the INSTANT period. We apply the same approach to the Lombok West mooring, where data is unavailable after June 2005 due to an early mooring parting.
Data output from individual instruments that exhibited significant gaps or stopped working entirely were generally not considered. It is worth noting that three years' worth of observations limit a thorough time series analysis, and the interpretation of intraseasonal phenomena can be biased. The reason for the temporary measurement periods lies in the fact that the deployment of moorings and their maintenance is expensive.

Preparatory work includes, first and foremost, the determination of sampling rates for each individual instrument. Sampling rates depend on the instrument and range between 10 minutes to 2 hours. Therefore, all data files are resampled onto a 2-hour time stamp. The pressure measurements provide important information regarding the mooring's current vertical position and reveal the extent of mooring blow-over it was subject to. Due to water being in constant motion, the mooring is not stationary and is not always in an upright position. The mooring can shift horizontally and vertically downward while always being fixed to the ground. This is referred to as mooring blow-over and needs to be accounted for in the preprocessing routine.

The preprocessing routine entails various steps and aims to create cross sections of along strait velocities (ASV) for each strait. After handling data gaps and resampling the data onto a common time base, we prepare data sets for each mooring and each variable. This includes stacking the data files according to their mounting depth and interpolating them onto the vertical levels (z-levels) provided by the Reanalysis products. In this way, the requirements for a clean comparison with Reanalyses are satisfied. Gaps were filled using linear interpolation or constant velocity equal to the shallowest measured velocity, i.e., the nearest neighbour (Sprintall et al., 2009).
Measurements from ADCPs require special treatment to account for mooring blow-over. We determine the actual measuring depths by subtracting the ADCPs range of bins from its location at each time stamp, as given by the pressure time series. We choose the smallest measured pressure value and assume it to be the moorings set value. The range of bins indicates the distances in which the instrument measures, or, in other words, the mid bin depth. The range of bins is a parameter of its own. In the case of no available pressure measurements, the pressure fluctuations from the nearest instrument are added to the instrument's preassigned mounting depth.

As with all velocity measuring instruments, the output only provides zonal u and meridional v velocity components. Therefore, data sets were constructed separately for the u and v components. The ASV is a quantity that combines u and v components to produce a velocity vector normal to the strait. This is achieved by generating a zonal vector $\vec{u}$ and a meridional vector $\vec{v}$ that represents the direction of the u and v components as measured by the instrument. We implement this by setting up two vectors originating from the mooring location and adding $0.5°$ along the zonal and meridional direction. The ASV can be seen as a projection of $\vec{u}$ and $\vec{v}$ onto the vector normal to the strait $\vec{n}$

$$\vec{w} = \frac{\vec{w} \cdot \vec{n}}{||\vec{n}||^2} \, \vec{n}, \tag{37}$$

where $\vec{w}$ serves as a substitute for both, $\vec{u}$ and $\vec{v}$. By calculating the absolute of each projection vector, their length, and accordingly, the contribution from each component to the flow is determined. Depending on the orientation (N-S or E-W) of the strait, the contribution from one component exceeds the other. Finally, the absolute values are multiplied with their corresponding u and v measurements, and the sum yields the along strait velocities. At this point, all gridded data sets have a temporal resolution of 2 hours, which are then converted into monthly means. It is also worth mentioning that according to the pressure data, the instruments barely measured at their mounting depth due to substantial mooring blow over.

To estimate the integrated transport through each strait, the observations are laterally interpolated between the moorings and extrapolated to the sidewalls. This requires a bathymetry and the land-sea mask from the Reanalysis products serves as such. Within this simulated bathymetry, the mooring point observations are linearly inter- and extrapolated within 10 m bins to the sidewalls while assuming a drop-off to zero flow at the sidewalls (Gordon et al., 2008). Bathymetric products have a lot of issues in regions with many islands, and especially those with narrow straits, such as occurs in Indonesia, where multi-beam measurements that might be included in the products are rare. In addition, the transport estimates in narrow passages can be very sensitive to the chosen bathymetry. We circumvent the

selection of a suitable bathymetry and choose the land-sea mask from Reanalysis to achieve a fair comparison. Since we are working with two different Reanalysis resolutions (1/4° and 1/12°), two bathymetries are available. The result is a cross section of along strait velocities.

Temperature and salinity data from moorings are retrieved in a similar way. After selecting the instruments that measured temperature, salinity, and pressure and dealing with time gaps, the data files are stacked according to their mounting depth. Pressure data provides information on the current location of the measuring device. Subsequently, the stacked data sets are interpolated onto the Reanalysis depth levels and averaged into monthly means. Note that temperature and salinity measurements are only available for the INSTANT program, constraining the data sets to approximately three years. Regarding salinity measurements, a maximum of two instruments per mooring delivered data.
One major difference between the current preprocessing method and the temperature preprocessing method concerns the extrapolation to the sidewalls. We still employ the land-sea mask from the Reanalysis products for the cross-passage inter- and extrapolation, but there is no need for a drop-off to zero towards the sidewalls.

4.4. Reanalysis Data

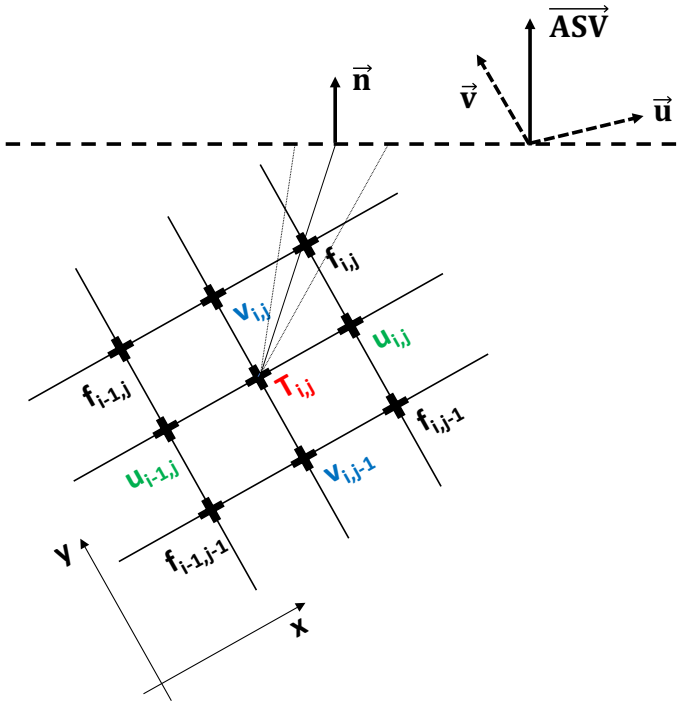

Figure 5: Schematic of the Arakawa C-grid in horizontal view with scalars (e.g., temperature $T_{i,j}$) at the cell center and vector components (e.g., velocity $u_{i,j}$, $v_{i,j}$) at the cell edges. Vorticity $f_{i,j}$ is defined at the corners of the cells. Dashed black line represents the reference line, $\vec{n}$ the vector normal, $\vec{u}$ and $\vec{v}$ the direct vectors, and $\overrightarrow{ASV}$ the desired along strait velocity vector.

Since all Reanalysis products use Arakawa C-grid staggering, the definition of a velocity vector at each grid point is not straightforward (Fig. 5). Employing an Arakawa C-grid means that the u and v velocity components are not calculated at the grid center but at

the West/East edges and the North/South edge of the cell, respectively. Scalar quantities, such as temperature T, are located in the center of the grid.
The procedure yielding cross sections of ASV is similar to the one applied to the observations. We start by finding the indices of the grid points closest to the desired cross section. This cross section is referred to as the reference line (Fig. 5). The next step includes the generation of vectors normal to the reference line $\vec{n}$ at each u, v, and T grid point. This is done with the implementation of three cross products that project the u, v, and T grid points on the native grid onto the reference line. Similar to the observational data preprocessing, direct vectors $\vec{u}$ and $\vec{v}$ are computed and subsequently, using Eq. 37 and the vector normal to the reference line $\vec{n}$, the projection vectors. Thus, the ASV vector $\overrightarrow{ASV}$ is calculated by projecting the velocity vectors onto the normal vector $\vec{n}$ and multiplying them with the amount of the vector going through the strait. The final step is to regridd the values onto the T points on the reference line. The output provides a gridded data set with, depending on the width and depth of the strait and the resolution of the Reanalysis product, x horizontal grid points, and z depth levels.

Similar to the observations, the transport through each strait is computed using lateral extrapolation. The extrapolation method is equivalent to that of the observations. The cross sections of along strait velocities can be constructed using two different methods. We either use the grid points x nearest to the mooring locations or employ all horizontal grid points. Using the nearest neighbours gives a more equitable comparison between observations and Ocean Reanalyses. In more narrow straits, we interpolate the nearest neighbours onto the actual mooring location. By employing all horizontal grid points, we can assess the full capabilities of each Reanalysis product. Due to the fact that grid points close to shelves occasionally exhibit deformed and unrealistic vertical profiles, the second nearest neighbour to the mooring location was employed.
Employing the nearest neighbours (NN) means taking the vertical profiles at the fixed grid points that are closest to the actual mooring locations to perform the cross-passage extrapolation. Using the interpolation method (INT) implies that we take the two fixed grid points closest to the mooring site and interpolate them towards the site. Depending on the product's capabilities to resolve the vertical profiles at each grid point, we chose either method.

Temperature data from Reanalysis products are available all the way up to the sea surface, covering the whole Reanalysis period. The cross-passage extrapolation is analogous to the one applied to the observations, and again two different methods are applicable.

One major advantage with Reanalysis data is the ability to retrieve data from every wanted strait. Solely the start and end coordinates of the desired cross section must be specified to determine the reference line. Thus, the Reanalyses permit the analysis of the volume transport budget within the Indonesian Seas. Furthermore, we can examine the ITF transport in the outflow passages beyond the INSTANT period.

In addition to the Ocean Reanalysis products, we make use of the ERA5 monthly mean 10m wind product with a horizontal resolution of $0.25° \times 0.25°$ (Hersbach et al., 2019).

4.5. Satellite-derived Data

To study physical processes relevant to the ITF, we employ gridded satellite-retrieved SST and SLA. Due to shipping traffic and fishing temperature and salinity measurements were only taken below 100 m. Therefore, the ESA SST CCI global sea surface temperature reprocessed product (Merchant et al., 2019) was used to interpolate the mooring observations towards the sea surface. The product has a high resolution of 1/20° (∼5 km grid resolution) and produces daily averages at 20 cm depth for the global oceans. The interpolation toward the sea surface facilitates the comparison with Reanalysis products, which are available at each grid point.
Satellite-retrieved gridded sea level anomalies are taken from the Copernicus Climate Change Service (CMEMS, 2021a), with a spatial and temporal resolution of 0.25° × 0.25° and daily. Time periods all complement the moored data.

As indicators of ENSO events, we employ the NINO3.4 SST index (NOAA, 2021), a product of NOAA Earth System Laboratory providing monthly means. Definitions of ENSO events correspond to the classifications made by Trenberth (2020).

4.6. Methods

The following section provides an overview of the methods used in this thesis. They can be divided into two parts: the first part focuses on employed methods to compare Reanalysis data with observations, while the second part deals with methods that help analyse variabilities of the ITF transport and its interaction with the large-scale sea level gradient.

One of the first tasks was the comparison of vertical velocity profiles. The aim here is to evaluate how well Ocean Reanalyses and observations agree based on a point-by-point comparison. This is done by comparing the vertical structure and the velocity maxima. Because Reanalysis data is available at every horizontal grid point within a strait and observations only at the mooring site, we use a nearest neighbour approach or interpolation. Many times interpolation did not deliver satisfying results, especially near the surface and subsurface sidewalls, and individual adjustments had to be made. Besides, ADCP data in the surface layer can be subject to surface reflection contamination and is oftentimes handled by disregarding the first ∼40 m (Sprintall et al., 2009; Gordon et al., 2008). By examining the Reanalysis profiles at different grid points, we get a first impression of their strengths and weaknesses. Resampling the mean vertical profiles into seasonal profiles enables the assessment of seasonal variabilities. This is especially useful when we focus on the seasonal cycle of ITF transport.

After performing the cross-passage extrapolation and adapting the extrapolated ASV to the bathymetry in each strait, we compared values of mean volume transport using Eq. 15. The mean volume transport is the integral over the constructed cross sections. We have again two options for computing the reanalysis-based volume transports: we either take the integral over the cross section containing all horizontal grid points, or we take the integral over the cross section containing only the nearest neighbours/interpolated profiles. This way, we can quantify how much information is lost by only observing selected sites in the strait. At the same time, it is possible to evaluate if the choice of mooring locations captures the transport through the strait well. Regarding the $\mathbf{z}$ component in Eq. 15, the greatest depth level in each strait is predetermined by the depth of the lowest current meter.

In order to understand variabilities in the ITF, we plot the time series of volume transports for each strait. To further highlight agreements and differences between Reanalysis products and observations, we compute the Pearson correlation coefficient r (adapted from Rodgers and Nicwander, 1988), given by

$$r = \frac{\sum_{i=1}^{N}(x_i - \overline{x})(y_i - \overline{y})}{\sqrt{\sum_{i=1}^{N}(x_i - \overline{x})^2 \sum_{i=1}^{N}(y_i - \overline{y})^2}}, \tag{38}$$

where N denotes the number of months, x_i represents the observational time series, y_i the Reanalysis time series, and $\overline{x}$ and $\overline{y}$ their means, respectively. The correlation coefficient indicates the linear correlation between two sets of data. In addition, we calculate the Root Mean Square Error (RMSE) (adapted from Stanski et al., 1990) between the observations and the Reanalysis products

$$\mathrm{RMSE} = \sqrt{\frac{1}{N}\sum_{i=1}^{N}(x_i - y_i)^2}. \tag{39}$$

Not unexpectedly, the time series exhibit a strong seasonal cycle. We remove the seasonal cycle by splitting the time series into climatologies and anomalies (adapted from Hantel and Haimberger, 2016). If we subtract the climatology from the original time series, anomalies remain. The climatologies are obtained by averaging the same months (e.g., all Januarys) over several years

$$x_k^{\mathrm{clim}} = \frac{12}{N}\sum_{i=0}^{N/12-1} x_{k+12i}, \tag{40}$$

where k is the number of months in a year, resulting in x_k^{clim} having 12 values, one for each month. The anomalies are thus given by

$$x_i^{\mathrm{ano}} = x_i - x_k^{\mathrm{clim}}. \tag{41}$$

Eqs. 40 and 41 apply to the Reanalysis time series as well. Ideally, the computation of anomalies requires time series of at least 30 years. The 3-year INSTANT period cannot deliver a representative climatology and thus, the computation of anomalies is not recommended. However, we consider anomalies in the case of the 13-year-long Makassar time series and certainly in the case of the temporally consistent Reanalysis time series.

Computing cross-correlations is part of the basic techniques in time series analysis. The cross-correlation serves as a useful tool for the quantification of any occurring shifts between the observations and the Reanalysis products. Instead of just computing cross-correlations, we also compute significant barriers to assess their significance. We execute this by generating two artificial time series sets of autoregressive processes using the observations and drawing several random samples. We use autoregressive processes of order one AR(1) (von Storch and Zwiers, 2001)

$$X_i = \alpha\ X_{i-1} + Z_i, \tag{42}$$

where α is the damping rate, X_i represents the time series of a random variable, and Z_i is drawn from a Gaussian normal distribution. That followed, we compute cross-correlations between the time series from both sets for every lag, yielding i cross-correlations for each lag. Finally, we calculate the 2.5% and 97.5% percentile of the cross-correlations at each lag. This way, we can determine if the correlation between observations and Reanalyses is explained by a real signal of if it is just random. If the cross-correlation falls outside of the significance barriers, the correlation is, with a certain probability, real. The choice of α in Eq. 42 specifies the probability. The cross-correlation (adapted from von Storch and Zwiers, 2001) between two data sets for a given lag τ reads

$$\rho_{xy}(\tau) = \frac{\gamma_{xy}(\tau)}{\sigma_x \sigma_y} \tag{43}$$

$$\gamma_{xy}(\tau) = E((x_i - \overline{x})(y_{i+\tau} - \overline{y})), \tag{44}$$

with the cross covariance function $\gamma_{xy}(\tau)$ that determines the linear relation between two time series at lag τ. σ_x and σ_y are the standard deviations of the considered time series. The lag refers to the offset between the two series, and its sign determines which series is shifted. As the lag increases, the number of possible matches decreases because the series no longer overlap towards the ends.
Since we are interested in intraseasonal phenomena that are known to influence the ITF, the mean seasonal cycle delivers useful information. In straits where the deployment period lasted only three years, i.e., the INSTANT period, the seasonal cycle is however, not as representative. Thus, the results have to be considered with caution.

To get a deeper understanding of the differences between observations and Reanalyses and their spatial distribution, we employ Hovmoeller diagrams (Hovmoeller, 1949). The axes of Hovmoeller diagrams usually depict temporal and spatial information, and the contour values of quantities such as velocity, temperature, or pressure are presented through color shading. Observational and Reanalysis data are plotted individually, but we also examine difference plots. We focus on a depth versus time representation while integrating over either ASVs. Here, the calculation of the RMSE is useful, but unlike Eq. 39, we take the difference between the temporal means and divide them by the number of depth levels. This yields the RMSE of the mean profiles.

In order to assess relations between the ITF transport in different straits and the large-scale sea level gradient, we create scatter diagrams. In the course of the following methods, we primarily focus on anomalies. Scatter diagrams serve as a convenient tool to study the correlation between two variables. Moreover, the diagrams can be used to investigate cause-and-effect relationships. This is why we employ them to analyse the impact the interocean pressure gradient has on the seasonal cycle of ITF transport. The large-scale sea level gradient is considered the difference in sea level anomalies between the western equatorial Pacific and the eastern tropical Indian Ocean. The partition of the ITF transport into an upper layer (<300 m) and a lower layer (>300 m) simplifies the interpretation of physical processes. Furthermore, we can use scatter plots to assess the behaviour of ITF transport during ENSO events.
Determining the areas we refer to as the western Pacific and eastern Indian Ocean (Fig. 2) requires the computation of correlation maps. We correlate the integrated transport with the SLA at every grid point and analyse the resulting correlation patterns. The method also highlights key regions for both inflow and outflow. We further verify the results with the computation of regression maps. Instead of determining the correlation, we depict linear regression coefficients at every grid point. In addition, the regression of integrated transports on the 10 m surface wind is computed.

5. Results and Discussion

For structural reasons, we split the following chapter into two parts. The first part presents the results obtained from the comparison between observations and Reanalysis products. We aim to provide explanations for occurring differences and similarities. The second part focuses on the seasonal cycle of ITF transport and its connection to the Pacific to Indian Ocean pressure gradient. In the course of this, we will concentrate on the ITF's connection to the Australian-Indonesian Monsoon and ENSO events.

Throughout this thesis, we will distinguish between a *short* and *long* Makassar Strait data set. The *short* data set contains the observations obtained during the INSTANT Program (2004-2006). This time frame is consistent with the observations in the outflow passages and favors a more accurate comparison. Once we focus on variabilities in the ITF and its seasonal cycle, we merge the INSTANT and MITF period into a *long* data set (2004-2017). We consider the fact that the MITF data sets have different maximum measuring depths.

5.1. Comparison of Observations and Reanalyses

5.1.1. Cross sections (INSTANT)

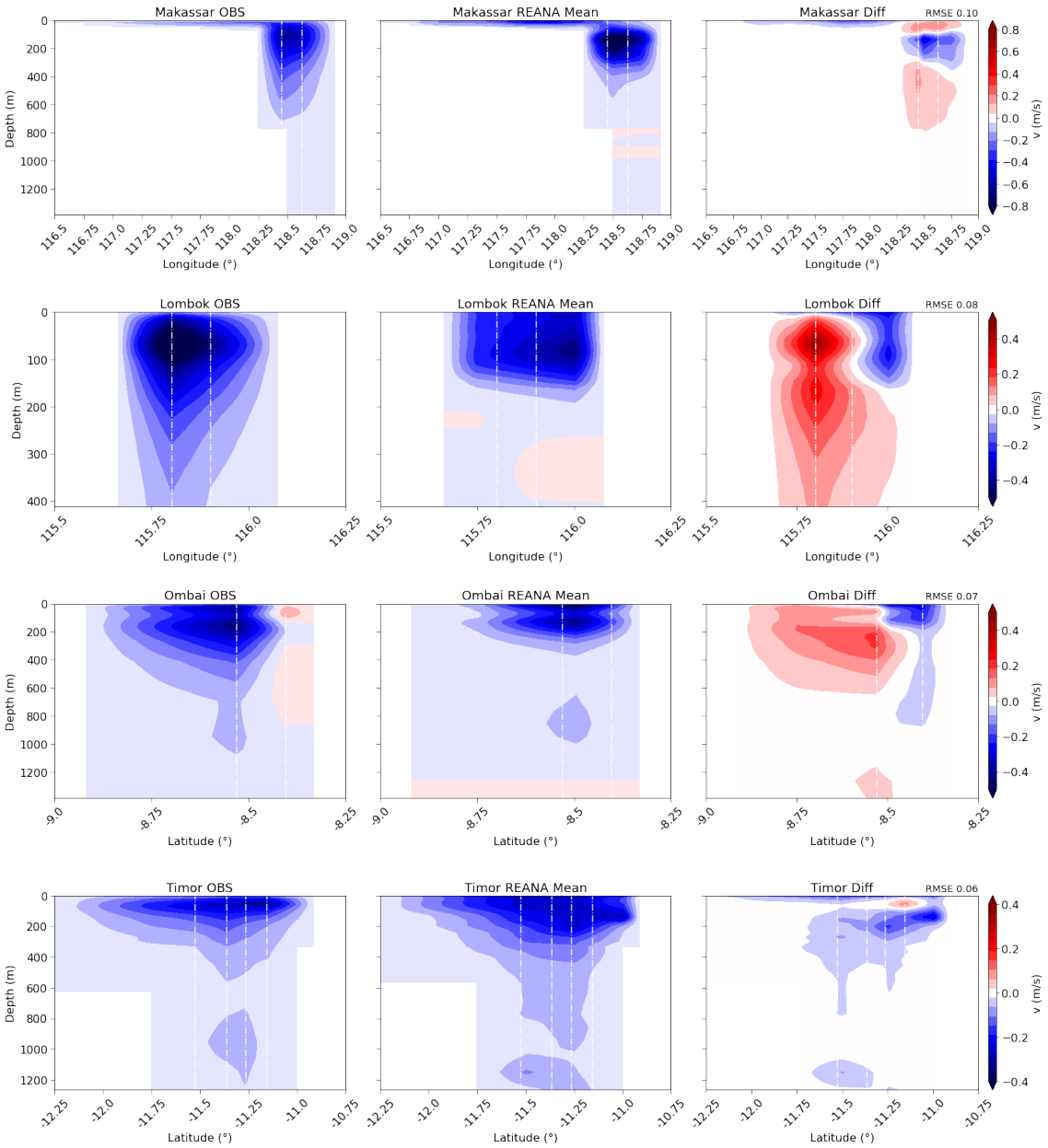

Figure 6: Mean ASV cross sections in Makassar Strait, Lombok Strait, Ombai Strait, and Timor Passage as given by the 1/4° bathymetry. The first column demonstrates observations (INSTANT Program, 2004-2006), the second column the Reanalysis Mean, and the third column their differences. RMSE between Reanalysis mean and observations are given in the top right corner. Negative values indicate southward-directed velocities (toward the Indian Ocean). White dash-dot lines represent mooring locations. Note the change in depth and velocity scales.

Figs. 6 show the mean ASV cross sections for the 3-year INSTANT period using the extrapolation methods introduced in section 4.3. Each observation plot displays the whole information we received from the moorings. The Reanalysis mean plots in Figs. 6 were

generated using all horizontal grid points. The vertical range of the Reanalysis mean plots was accordingly adapted. The sign convention throughout this thesis is such that negative values indicate southward-directed (northward-directed) transport, i.e., towards the Indian Ocean (Pacific). The comparatively low RMSE values between the Reanalysis products and the Reanalysis mean (Figs. A36-39) justify the mere comparison between the observations and the Reanalysis mean.
In Makassar Strait, the strongest southward flow is not within the warm sea surface layer but within the cooler thermocline around 110 m. The depth of the maximum varies with season. The Reanalysis mean displays a slightly vertically shifted maximum in ∼140 m. Evidently, this is where the greatest differences occur. While the Reanalysis mean is able to capture the structure of the mean velocity profile, it tends to overestimate its magnitude. This holds true for all products, with FOAM and GLORYS2V4 exhibiting the least vertical structure (Figs. A40). Moreover, we find that the Reanalysis products are still able to provide notable information over the westward shallow shelf. Table 4 provides the corresponding integrated transport estimates. The observed integrated transport (-10.7 Sv) undermatches the value found by Gordon et al. (2008) (-11.6 Sv) by about 1 Sv. Due to the lack of documentation, we are unable to compare procedures in the preprocessing routine. Estimating the transport over the extended Makassar Strait time series yields a mean value of -9.9 Sv between 0 and 700 m. Quantitatively, the Reanalysis mean transport (-11.5 Sv) is in good agreement with the literature value. Focusing on the transport between 118.25°E and 118.9°E, i.e., the Labani Channel, the observed transport decreases to -9.9 Sv, and the Reanalysis mean transport becomes -9.5 Sv. According to that, approximately 1-2 Sv are missed by only observing within Labani Channel. Naturally, the Reanalysis mean exhibits a higher discrepancy because it tends to overestimate velocities and provides information in an area where observations only possess extrapolated information. The third column in Table 4 displays integrated transport estimates using only the nearest neighbours or the interpolated profiles. In the case of Makassar Strait, the nearest neighbour method was chosen. A comparison between all three values indicates that most of the transport happens within Labani Channel, and using the nearest neighbours is in good agreement with the observed transport estimate. Accordingly, the choice of mooring locations seems to capture the transport through Makassar well. Note that the nearest neighbours are the only two grid points within Labani Channel.

Velocity increases towards the west in Lombok Strait, with this side of the strait also displaying the most variability. The observed velocity maximum is located in approximately 70 m, while the Reanalysis mean maximum appears in ∼90 m. Furthermore, the Reanalysis mean is not able to capture intensification in the west. The difference plot verifies this statement. As a matter of fact, none of the Reanalysis products capture the stronger westward flow (Fig. A41).
The reason for the higher located velocity maximum lies in the fact that Lombok Strait is rather shallow and thus stronger influenced by the wind surface stress. The Reanalysis mean adequately represents an intensified surface flow while also displaying weak northward velocities (max. -0.44 m/s) in greater depths. The moorings display effective velocities down to 450 m, whereas the Reanalysis mean lacks substantial information below ∼200 m. Regarding integrated transport estimates, we find a mean value of -2.6 Sv (Tab. 4), which coincides with transport estimates found by Sprintall et al. (2009). The Reanalysis mean underestimates this value by about 1 Sv, yielding a mean transport of -1.5 Sv. The Reanalysis mean does not capture the ITF core and underestimates velocity in

greater depths, partly explaining the difference of 1 Sv. Lombok Stait is rather narrow, and the 1/4° bathymetry provided by the Reanalysis land-sea mask is unable to resolve characteristics of the topography. This likely explains the small discrepancy between the Reanalysis mean and the Reanalysis mean using only the interpolated profiles (-1.1 Sv). In the case of Lombok Strait, the interpolation method did not cause any shelf-induced problems. Employing the nearest neighbour method would yield the same result as the Reanalysis mean because there are only two horizontal grid points within Lombok Strait.

In Ombai Strait, two ITF cores are noticeable: a surface core and a stronger subsurface core located at about 180 m. These findings are coherent with the literature (Sprintall et al., 2009). The Reanalysis mean is able to capture both maxima, however, they are slightly upwards-shifted compared to the observations. The fact that the flow on the northern side of Ombai Strait is directed eastwards, i.e., towards the Banda Sea, is evident in the observations. The Reanalysis mean, on the other hand, is unable to reproduce this property and displays an increased eastward flow in the North instead. Ombai Strait is slightly broader than Lombok Strait, but still, only two horizontal grid points provide information. Furthermore, the vertical resolution of the Reanalysis mean is - similar to Lombok Strait - limited. The Reanalysis products CGLORS and FOAM (Figs. A42) exhibit substantial vertical resolution down to ∼1000 m. The remaining products capture the two core structure, but information deteriorates below 400 m. Moorings provide information down to 1500 m. The difference plot supports the fact that the Reanalysis mean resolution is vertically limited and unable to capture the eastward flow in the North of Ombai Strait. We find a mean integrated transport of -5.3 Sv, which is in good agreement with the values attained by Sprintall et al. (2009) (-4.9 Sv). By looking at the Reanalysis products and their suppressed vertical structure in Figs. A42, it becomes evident why the Reanalysis mean is unable to achieve a higher mean transport (-3.5 Sv). In accordance with the mooring locations, the integrated vertical profiles account for a greater mean transport of -4.1 Sv. This underlines the fact that the flow, as represented by the products, intensifies towards the North.

In Timor Passage, the ITF is strongly bound to the surface within the upper ∼200 m. The surface flow is strongest towards the North near Timor Roti (Tab. 1) as suggested by Figs. 6. A secondary weak maximum is centered around 1000 m. The deeper core is linked to the Indonesian Intermediate Water carried by the ITF (Talley and Sprintall, 2005). The moorings provide information down to 1800 m, but the 1/4° bathymetry cannot resolve depths below ∼1250 m in Timor Strait.
Overall, Timor displays little upper ocean variability compared to Lombok and Ombai, which is likely a cause of its segregation from the equatorial Indian Ocean and associated Kelvin wave activities (Sprintall et al., 2009). This will be addressed later on.
The strongly concentrated surface flow is also evident in the Reanalysis mean. Velocities of ∼ -0.2 m/s extend to 200 m, whereas the observed maximum remains confined to the surface, possibly explaining the maximum differences in 150 m. Moreover, the Reanalysis mean displays substantial vertical structures down to ∼1250 m. This proves that the Reanalysis products are generally able to capture the ITF's vertical structure, even in greater depths, as long as the channel is broad enough. Apart from CGLORS and FOAM, the products display similar capabilities regarding resolution in greater depths (Figs. A43). CGLORS and FOAM lose some of those capabilities as the passage tightens. Nonetheless, a comparison with Lombok and Ombai Strait suggests that the 1/4° products are better at

resolving the broader straits of Makassar and Timor.
We find a mean transport of -6.7 Sv in Timor Passage. The discrepancy between this value and the one found by Sprintall et al. (2009) of -7.5 Sv may partly be attributed to small differences in the extrapolation method and the choice of bathymetry. The Reanalysis mean transport of -8.9 Sv overestimates the observed transport and also the literature value. This supports the fact that the performances of the 1/4° products generally increase in broader straits, especially concerning the resolution of the bathymetry, albeit overestimating velocities. Using only the interpolated profiles, the Reanalysis mean increases to -9.9 Sv.
According to the definition of Sprintall et al. (2009), Timor Passage is not bordered by a sidewall at its southernmost point. Instead, it is bordered by the Ashmore Reef, however, to perform the extrapolation, we still assume a drop-off to zero towards the South. The transport over the Australian shelf can be estimated with Reanalyses. The Reanalysis mean estimates an integrated transport of -10.0 Sv between Timor (123°E; 10.65°S) and Australia (123°E; 17.0°S), yielding a transport of -1.1 Sv over the shelf. This rather low transport results from the fact that westward-directed flow within Timor Passage is mostly compensated by eastward transports over the shelf.
So far, reanalysis-based full-field integrated transports overestimated observational transports in the broader straits of Makassar and Timor and underestimated transports in the narrow straits of Lombok and Ombai. 1/4° products (∼28 km) have a hard time catching abrupt changes in ASV cross sections.

Table 4 presents the mean estimated transports in each strait as given by the observations and Reanalysis products. According to Tab. 4, we find an observed ITF inflow of -10.7 Sv through Makassar Strait, that is unevenly compensated by a combined stronger outflow of -14.6 Sv through Lombok Strait, Ombai Strait, and Timor Passage. The Reanalysis mean arrives at an inflow of -11.5 Sv and an outflow of -13.9 Sv. Considering the 1/12° bathymetry corresponding to GLORYS12V1, the observed inflow decreases towards -9.9 Sv and is again unevenly balanced by a greater outflow of -13.6 Sv. The imbalance increases with GLORYS12V1 reaching an inflow and outflow of -9.5 Sv and -15.2 Sv, respectively. By definition of the continuity equation (Eq. 19), the ITF inflow from the western Pacific must be compensated by the outflow into the eastern Indian Ocean. However, Tab. 4 only covers the major inflow and outflow passages within the Indonesian Archipelago, disregarding a number of secondary passages. Furthermore, budgets based on Reanalyses are impacted by data assimilation and unresolved mixing (Balmaseda et al., 2013).
A table of transport estimates for each Reanalysis product can be found in the Appendix Tab. A6.

Table 4: Comparison of mean integrated ITF transport estimates during the INSTANT Program (2004-2006). Transport averages are given in Sverdrup, with negative values indicating southward-directed transport (towards the Indian Ocean). The upper (lower) panel refers to the 1/4° (1/12°) bathymetry. Third column refers to full-field integrated transports. Fourth column displays integrated transports using the NN/INT-method.

Strait	OBS (1/4°)	REANA Mean (all)	REANA Mean (NN/INT)
Makassar	-10.7	-11.5	-10.5
Lombok	-2.6	-1.5	-1.1
Ombai	-5.3	-3.5	-4.1
Timor	-6.7	-8.9	-9.7

	OBS (1/12°)	GLORYS12V1 (all)	GLORYS12V1 (NN/INT)
Makassar	-9.9	-9.5	-11.2
Lombok	-2.6	-2.5	-2.5
Ombai	-5.1	-4.0	-3.4
Timor	-5.9	-8.7	-9.7

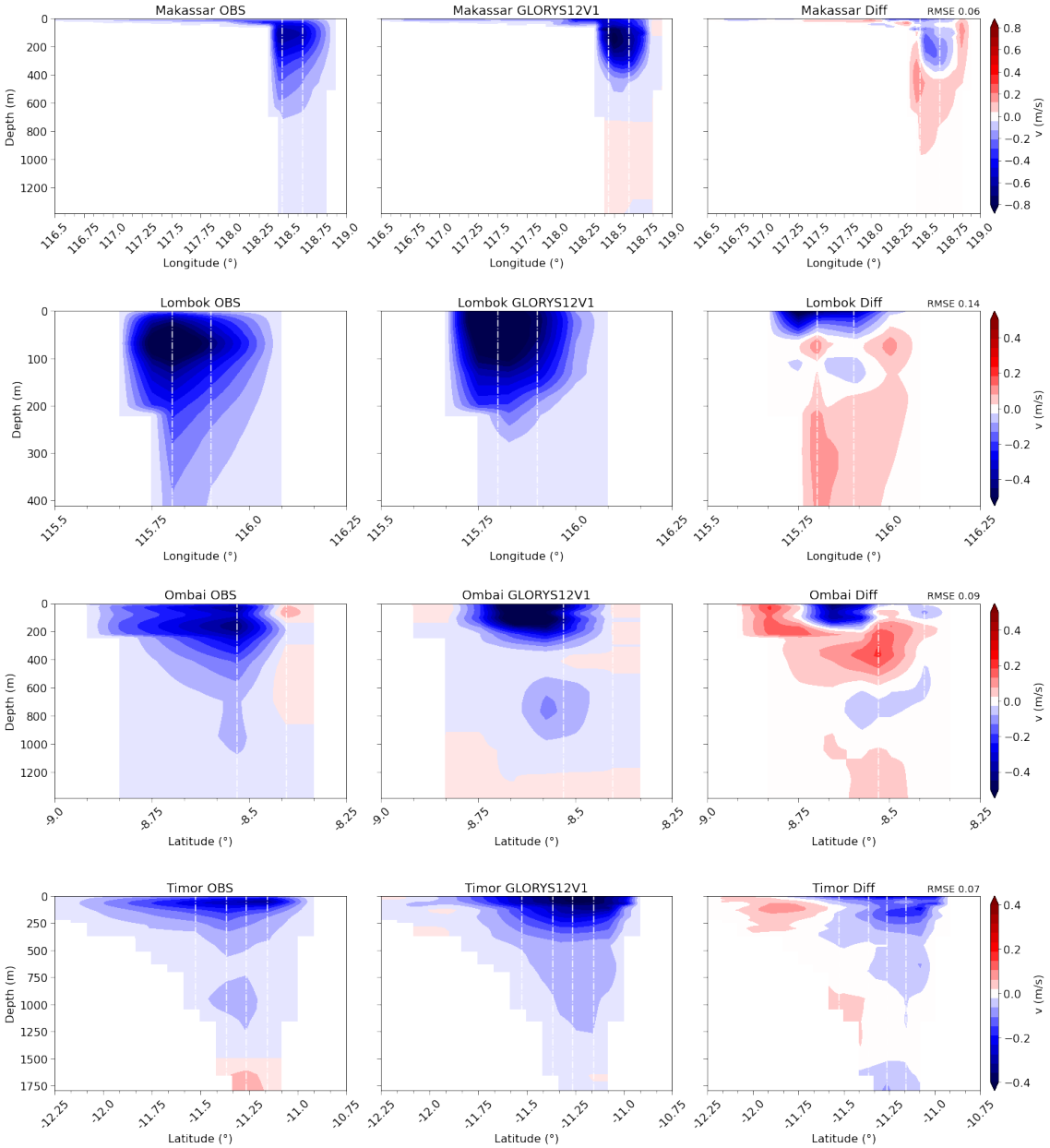

Figure 7: Mean ASV cross sections in Makassar Strait, Lombok Strait, Ombai Strait, and Timor Passage as given by the 1/12° bathymetry. The first column demonstrates observations (INSTANT Program, 2004-2006), the second column GLORYS12V1, and the third column their differences. RMSE between GLORYS12V1 and observations are given in the top right corner. Negative values indicate southward-directed velocities (toward the Indian Ocean). White dash-dot lines represent mooring locations. Note the change in depth and velocity scales.

Figs. 7 show cross sections of mean ASV using the 1/12° bathymetry. Instead of comparing the observations to the Reanalysis mean, we now employ the higher resolving Ocean Reanalysis, GLORYS12V1. The minor ticks in each plot highlight the difference in resolution compared to Figs. 6. Overall, we achieve a more detailed representation of the bathymetry using the 1/12° land-sea mask. As a result, the straits become more narrow. White spaces are left intentionally, further highlighting the differences in resolution. GLORYS12V1 is able to capture properties that the Reanalysis mean could not resolve.

In Makassar Strait, explicitly the Labani Channel, the 1/12° land-sea mask apprehends its structure in more detail. In addition, GLORYS12V1 reproduces the velocity maximum in the West. However, the Reanalysis still overestimates the observations displaying velocities of up to -0.9 m/s. In contrast, velocity maxima captured by the observations move around ∼ -0.6 m/s. Although the ITF core shifts towards the West, the vertical resolution does, at first glance, not improve by a lot. By comparing the Reanalysis mean with GLORYS12V1 in the deepest layers (∼ 1250 m), we find that GLORYS12V1 still generates velocities on the order of 10^{-3} m/s, while the Reanalysis mean decreases towards orders of 10^{-5} - 10^{-9} m/s. GLORYS12V1 is in good agreement with magnitudes represented by the observations in deeper layers, albeit exhibiting a more northern component.
The lower panel in Tab. 4 corresponds to the cross sections depicted in Figs. 7. Compared to the 1/4° bathymetry values (upper panel), the transports for both observations (-9.9 Sv) and GLORYS12V1 (-9.5 Sv) decrease. At this point, it is worth mentioning that the GLORYS12V1 NN transport was not estimated using two nearest neighbours but the second nearest neighbour in the case of the west mooring. The second nearest neighbour was employed after we noticed a shelf-induced artifact that manipulated the nearest neighbour at 118.12°E. This, in turn, may slightly manipulate the GLORYS12V1 NN (-11.2 Sv) transport, but given a horizontal grid spacing of 9 km, the comparison remains reasonable.

The 1/12° land-sea mask improves the topography in Lombok Strait as well. As discussed in Figs. 6, the 1/4° Reanalyses are not able to reproduce the stronger westward flow within Lombok Strait. Figs. 7 demonstrate that GLORYS12V1 adequately represents this intensification while also capturing the intensified surface flow. Furthermore, the vertical resolution increases, extending the ITF core down to ∼280 m. The improved agreement between the observed and the reanalysis-generated cross section is reflected by the transport estimates. The observed transport (-2.6 Sv) remains unchanged, whereas GLORYS12V1 achieves a higher and thus similar transport of -2.5 Sv. In fact all three values, including the GLORYS12V1 INT transport of -2.7 Sv, agree fairly well.

The two core structure within Ombai Strait is not as clearly represented by GLORYS12V1 as by the Reanalysis mean. It seems as though the maxima exist, however, merging into one another. The consideration of the mean vertical profile reveals that the surface core exceeds the subsurface core. This is not in accordance with the observations nor the Reanalysis mean. Contrary to the observations and the Reanalysis mean, where both cores are centered around 8.5°S, GLORYS12V1 displays a rather centered flow. This is highlighted by the strong negative surface maximum in the difference plot.
The observations indicate the presence of an eastward-directed flow to the North of Ombai Strait. The Reanalysis mean was unable to capture this effect, whereas GLORYS12V1 can. The weak core between ∼600 and 1000 m increases with GLORYS12V1, with flow dropping to a minimum between ∼400 and 500 m. We also find this behaviour with the Reanalysis mean, although displaying a weaker deep core. Both the Reanalysis mean and GLORYS12V1 display values on the order of 10^{-2} m/s in ∼1300 m, with GLORYS12V1 capturing stronger variabilities. Again, magnitudes agree well with the observations, but velocity values turn positive towards the sea floor. This is represented by the light pink shading in deeper levels and resembles what we found in Makassar Strait.
The observed mean transport of -5.1 Sv (Tab. 4) barely deviates from the 1/4° transport value. The vertically shifted ITF cores do not influence the integration over the cross section, yielding an increased GLORYS12V1 transport of -4.0 Sv. Moreover, the merged

velocity cores are visibly more pronounced compared to the Reanalysis mean in Figs. 6.

As shown in Figs. 6, the 1/4° bathymetry limits the vertical resolution in Timor Strait to a depth of ∼1250 m. Within the 1/12° bathymetry, data are available to a depth of ∼1750 m. This way, observations from the deep-reaching Timor Sill mooring are visible. Below ∼1500 m, mean ASV are directed eastward, towards the Timor Sea. According to Sprintall et al. (2009), the eastward-directed deep flow exits back into the Indian Ocean below ∼1300 m.
The impact of the Australian shelf in the South of Timor Passage was not nearly as good resolved in the 1/4° bathymetry as it is with the 1/12° bathymetry. The ITF core in GLORYS12V1 remains bound to the surface within the upper 200 m exhibiting greater velocities compared to the Reanalysis mean. Sections of eastward-directed flow are indicated over the visible part of the Australian shelf. Similar to the Reanalysis mean, the ITF structure is definite down to ∼1250 m, where the channel becomes even narrower. GLORYS12V1 reproduces some of the eastward-directed ASV below 1500 m, however, velocities are mainly negative.
Integrated transport estimates are in fairly good agreement with the Reanalysis mean transports. The more detailed bathymetry and small sections of eastward-directed velocities decrease the GLORYS12V1 transport to -8.7 Sv. Then again, using only the interpolated profiles at the mooring locations, the transport increases to -9.6 Sv. We find this to be the case in the 1/4° bathymetry with the Reanalysis mean as well. This suggests that the choice of mooring locations coincides with the area of maximum ITF transport.
The conclusion that Reanalyses overestimate transports in broader straits and lean towards underestimation in narrow straits is only partly true regarding GLORYS12V1.

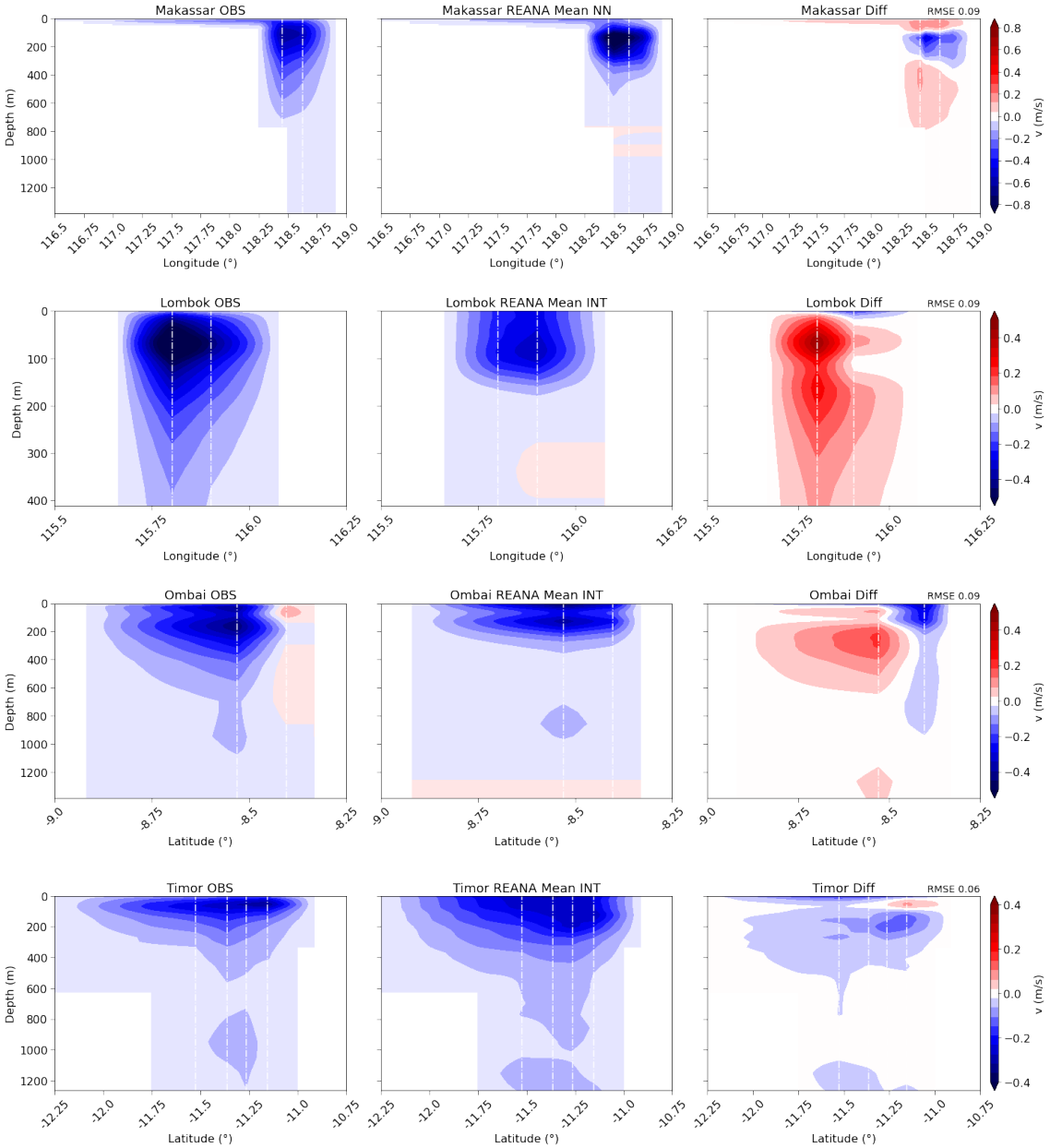

Figure 8: Mean ASV cross sections in Makassar Strait, Lombok Strait, Ombai Strait, and Timor Passage as given by the 1/4° bathymetry. The first column demonstrates observations (INSTANT Program, 2004-2006), the second column corresponding velocities using the NN/INT-methods, and the third column their differences. RMSE between NN/INT cross sections and observations are given in the top right corner. Negative values indicate southward-directed velocities (toward the Indian Ocean). White dash-dot lines represent mooring locations. Note the change in depth and velocity scales.

Figs. 8 and 9 display the most fair comparison between observations and Reanalyses. The first column corresponds to the results in Figs. 6 and the second column shows the respective reanalysis-based cross sections using the NN/INT-method.
Moorings in Makassar Strait measured higher velocities to the West of Labani Channel, and although there is an explicit overestimation in the Reanalysis mean, it mimics this behaviour. Since mean integrated transports between observations (-10.7 Sv) and the Reanalysis mean (-10.5 Sv) exhibit a high agreement, overestimation is most likely compensated by stronger

vertical flow in the observations. Reanalyses often struggle with capturing asymmetries in narrow passages, but this is not the case here. Apart from the overestimation, the most striking drawback in Reanalyses is the vertical resolution.

Contrary to Makassar Strait, the Reanalysis mean struggles to capture the dominant flow to the West of Lombok Strait. Figs. A41 confirm that the flow increases towards the East in all Reanalysis products, thus, this is not a result of the extrapolation. Accordingly, the difference pattern does not change considerably compared to Figs. 6 apart from the discrepancies in the East. The underestimation of current velocities and the lack of vertical resolution yield a difference in the transport of -1.5 Sv. Considering that we find an observed transport of -2.6 Sv, such a difference is substantial.
According to the difference plot, positive velocities in greater depths are too weak to impact the total transport.

Consequences of the extrapolation are visible in Ombai Strait. The already surface-confined flow is extended horizontally by the extrapolation. Furthermore, 1/4° Reanalyses do not capture the eastward-directed flow in the North, yielding a negative maximum in the difference plot. The lack of vertical resolution in most Reanalysis products (GLORYS2V4, ORAS5, and ORAP6) creates the area of positive velocities in the difference plot and is ultimately most likely the reason for the decrease in transport (Δ $\sim$1.2 Sv). However, due to the horizontal extension of the flow, the resulting transport (-4.1 Sv) surpasses the full-field transport value (-3.5 Sv). Due to the fact that the moorings are closely located, the NN method is not a viable option.

Similar to Figs. 6 the RMSE remains low in Timor Passage. The RMSE is mainly composed of differences in the North, where the Reanalysis mean locates the ITF core in a slightly larger depth, as indicated by the difference plot. We find the reanalysis-based core extending towards $\sim$200 m, whereas the observations display an enclosed maximum in $<$100 m. The difference plot further implies that the Reanalyses overestimate velocities in the South.
Contrary to the other straits, the Reanalysis mean reproduces distinct flow extending to $\sim$1000 m depth. However, when compared to observations, these appear to be too strong. The overestimation of velocities above 600 m leads to a substantial discrepancy in the mean integrated transport (Δ $\sim$3 Sv). Besides, velocities are already higher in Reanalyses, and the fact that the INT-method extrapolates four vertical profiles instead of two, causes a strong overestimation. We also notice that the deep-reaching velocities ($\sim$1000 m) correspond to the Timor South Slope mooring, and this also resonates with the observations. According to the later to be discussed Figs. 12, the Timor Ashmore mooring also contributes to the higher speeds. The increase in velocity around 1200 m in the Reanalysis mean is likely to be distorted by the extrapolation, but its representation speaks for the Reanalyses.

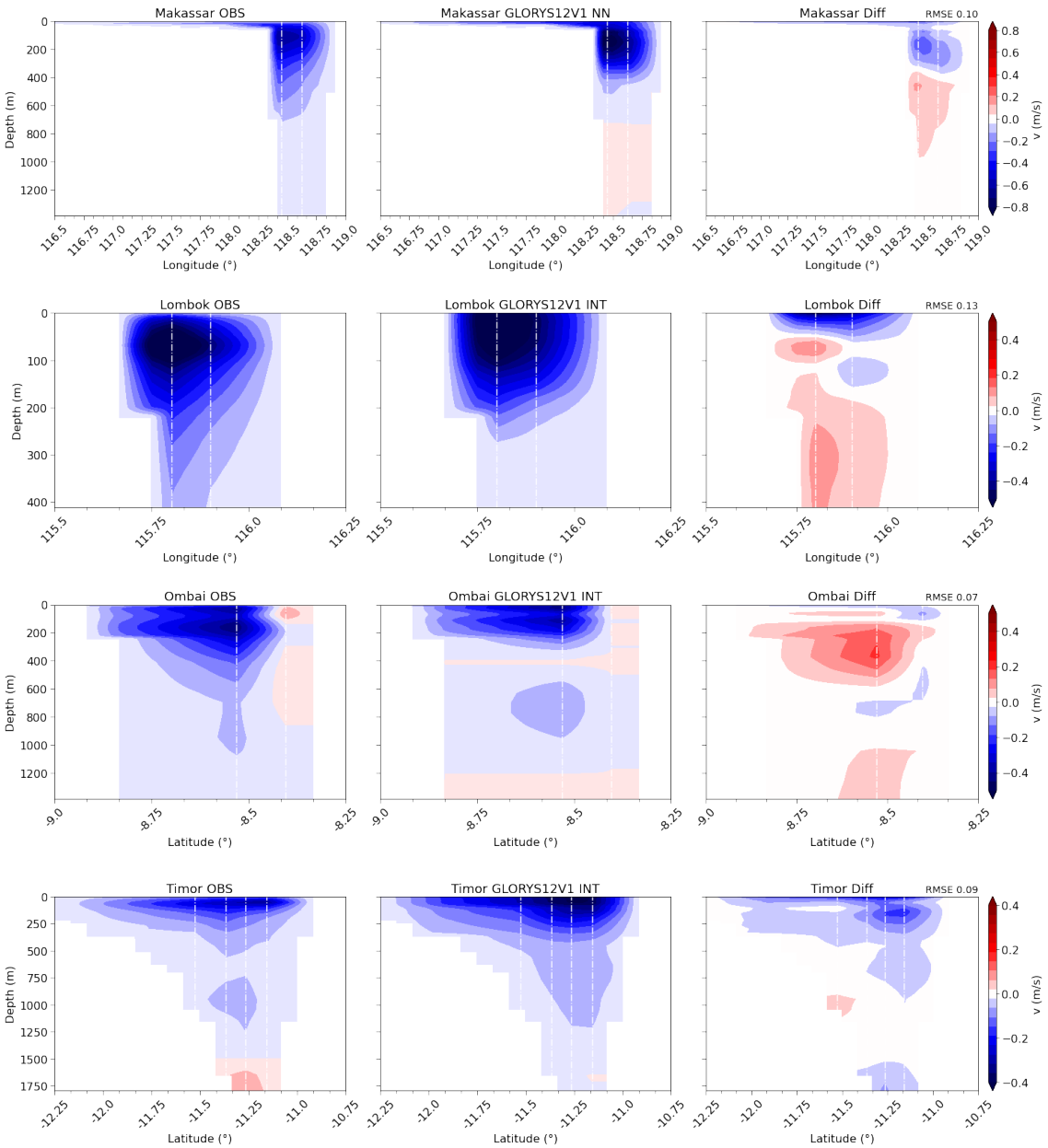

Figure 9: Mean ASV cross sections in Makassar Strait, Lombok Strait, Ombai Strait, and Timor Passage as given by the 1/12° bathymetry. The first column demonstrates observations (INSTANT Program, 2004-2006), the second column corresponding velocities using the NN/INT-methods, and the third column their differences. RMSE between NN/INT cross sections and observations are given in the top right corner. Negative values indicate southward-directed velocities (toward the Indian Ocean). White dash-dot lines represent mooring locations. Note the change in depth and velocity scales.

Figs. 9 display the same comparison as Figs. 8 using the 1/12° bathymetry and GLORYS12V1.

The difference pattern in Makassar Strait resembles the one in Figs. 6 (full-field cross section) with Reanalyses overestimating velocities in the upper 400 m and observations exhibiting stronger velocities to ∼1000 m. These also arise because velocities in GLORYS12 turn positive below the sill depth of ∼700 m. The westward located ITF core is spatially well represented by the second nearest neighbour at 118.5°E but is still too strong. As

a result, the integrated transport is overestimated by 1.3 Sv even though observations hold an advantage in the vertical. Besides, the flow over the western shelf must not be underestimated in the Reanalyses. We also have to consider the fact that the ADCP measures velocity in 10 m intervals (first 400 m) while GLORYS12V1 generates data on 22 vertical levels within the first 100 m. Afterwards, the vertical spacing increases steadily.

According to the difference plot, the INT-method yields a pronounced surface-intensified flow in Lombok Strait. We have found the same to be true in the full-field cross section (Figs. 7). Thus, high velocities occur near the sea surface while the observed ITF core occurs at 80 m depth. Although the vertical resolution increases with GLORYS12V1 (Figs. 8), the red shaded area highlights the weak velocities below ∼250 m. However, these do not seem to have a strong influence on the integrated transport, indicated by a difference of 0.1 Sv.

We have already established the fact that GLORYS12V1 accurately reproduces the weak positive velocities in the North of Ombai Strait. As shown by the difference plot, positive velocities are slightly stronger in the observations. Furthermore, we find the two core structure to be more pronounced using the INT-method, however, both cores are underestimated by GLORYS12V1. Only again in ∼800 m does GLORYS12V1 reproduce more striking negative velocities that even surpass the observations.
We did not expect much improvement here compared to Figs. 7 because the INT-method does not change information available in the vertical. The underestimation of GLORYS12V1 is underlined by a 1.7 Sv decrease in transport.

Regarding Timor Strait, the full-field transport (-8.7 Sv) already overestimated the observed transport by 2.8 Sv (Figs. 7). Using the INT-method, the flow to the south is not slowed down and thus yields an even higher integrated transport of -9.7 Sv. As specified by the difference plot, the maximum of the flow is accurately located to the North of the strait where the passage deepens, but it is overly pronounced. The visibly higher velocities extend to a depth of 1250 m and thus do not detect the individual deeper maximum in around 1000 m. We will address the positive velocities towards the sea floor later on but hold onto the fact that magnitudes are of the order 10^{-6} - 10^{-8} m/s in GLORYS12V1 and mostly negative. Positive velocities in the observations are of the order 10^{-2} - 10^{-3} m/s and are primarily captured by the deep-reaching Timor Sill mooring. Such narrow and deep sites are also extremely difficult to represent for actual bathymetry products.

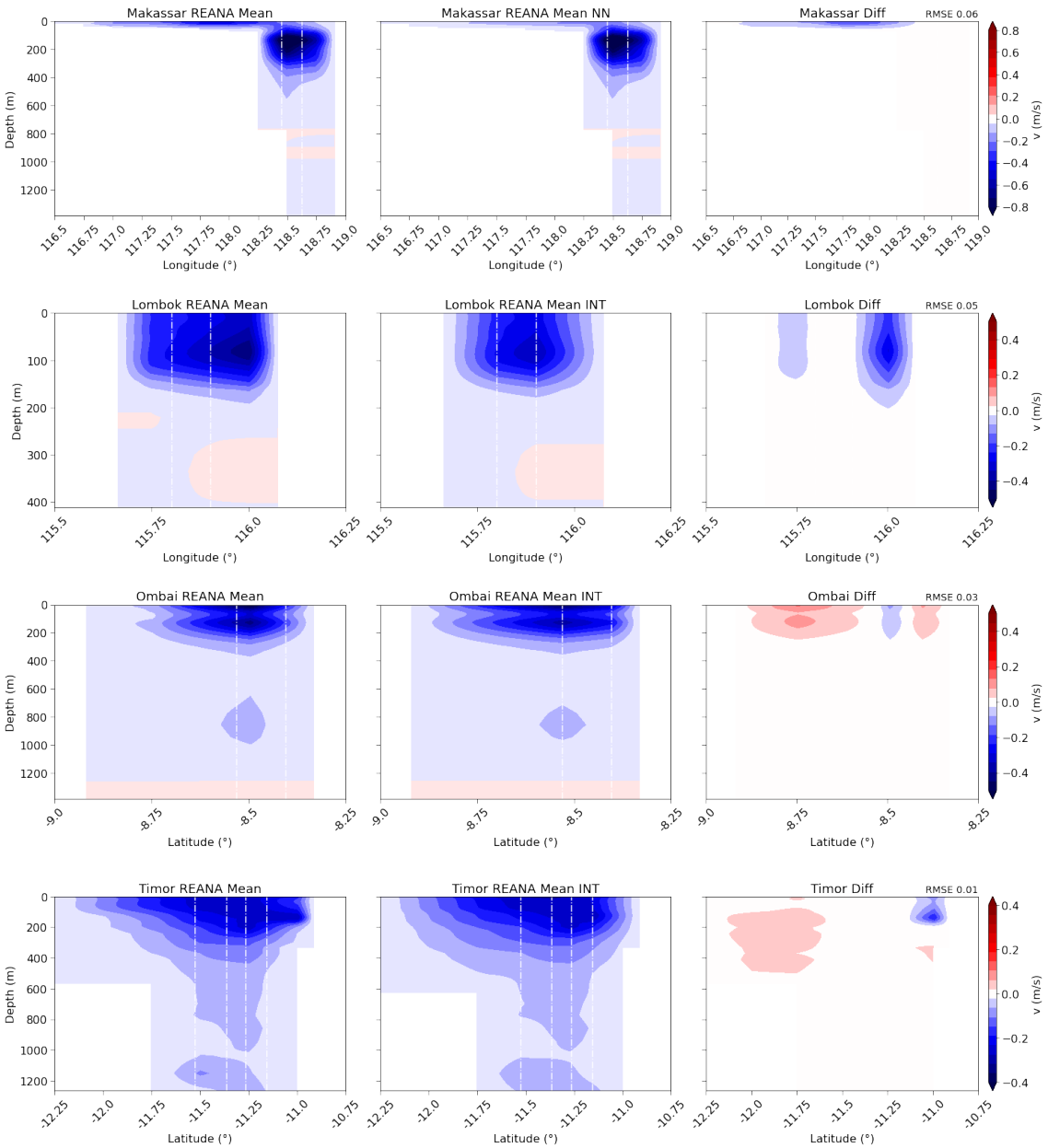

Figure 10: Mean ASV cross sections in Makassar Strait, Lombok Strait, Ombai Strait, and Timor Passage as given by the 1/4° bathymetry. The first column demonstrates Reanalysis mean full-field integrated transports (2004-2006), the second column corresponding velocities using the NN/INT-methods, and the third column their differences. RMSE between full-field and NN/INT cross sections are given in the top right corner. Negative values indicate southward-directed velocities (toward the Indian Ocean). White dash-dot lines represent mooring locations. Note the change in depth and velocity scales.

Figs. 10 display the cross sections that are used to compute the integrated transports in Table 4. The first column of cross sections in Figs. 10 equals the second column in Figs. 6. In order to create the cross sections in the second row, we merely consider the nearest neighbours (NN) or integrated profiles (INT) in the extrapolation. In addition, we show their differences in the third column and the corresponding RMSE. The aim of Figs. 10 and 11 is to quantify how accurately the transport through cross sections is captured by only observing at selected sites.

As expected, differences between full-field cross sections and the NN-method vanish within Labani Channel in Makassar Strait. Ticks shown on the x-axis indicate the available horizontal grid points. Thus the only two grid points representing the channel are also the nearest neighbours providing identical information within Labani Channel. Apart from small discrepancies over the shelf resulting in a RMSE of 0.06 m/s, the cross sections are identical. Choosing the NN-method decreases the mean transport by 1 Sv to -10.5 Sv drawing it closer to the observed transport of -10.7 Sv. We conclude that the vast majority of the transport through Makassar is captured by only observing at two sites in Labani Channel.

Considering Lombok Strait, the INT-method shifts the ITF core more towards the middle of the strait. This is ultimately clear regarding the centered mooring locations at 115.8°E and 115.9°E. Moreover, the shift is visible in the difference plot. The mooring's close locations are also the reason for choosing the INT-method over the NN-method. The mean integrated transport decreases from -1.5 Sv to -1.1 Sv considering only the interpolated profiles. This is a result of the weaker currents in the areas around the moorings. Disregarding the fact that the Reanalysis mean misleadingly locates the ITF core in the East, we find that the INT-method reproduces the cross section inadequately. Moreover, the structure does not conform with the observations either. We also have to take into account the fact that there are only two grid points (Δx $\sim$28 km) available in the $\sim$35 km wide strait. Both of them are located closer to the sidewalls rather than to the mooring locations.

Circumstances reverse in Ombai Strait, where the mean transport increases with the application of the INT-method. As before, due to the strait's narrow width and the short distance between the moorings, we apply the INT-method. In doing so, the difference plot confirms the arising increase in velocity towards the South in the upper $\sim$300 m. The extension is underlined by the fact that the mean transport increases from -3.5 Sv to -4.1 Sv.
Considering all grid points, the weak vertical profile at 8.75°S traps the flow towards the North. The INT-method, on the other hand, strongly depends on the vertical profile at 8.5°S and generates thus a stronger transport. So far, we conclude that a third mooring located towards the South could help to fix the ITF core's position. Nonetheless, the choice of mooring locations is comprehensible because observations and the full-field cross section find maximal transport around 8.5°S.

Considering Timor Passage, the INT-method reproduces the cross section accurately. This is highlighted by a low RMSE of 0.01 m/s. Taking all grid points into consideration, we arrive at a transport of -8.9 Sv, whereas the INT-method increases this value to -9.7 Sv. With the employment of four interpolated profiles in a passage featuring six grid points, one would possibly assume a higher agreement. However, the moorings all lie within the deep-reaching channel, which is captured by only two grid points. Similar to Ombai Strait, the remaining grid points help shape the main ITF core. Thus, there are two relevant grid points incorporated in the full-field transport but four grid points in the INT-method. Nonetheless, the cross-passage structure seems to be captured well by observing at several sites.
We assume that the resolution of the 1/4° bathymetry is too coarse to state whether the NN-method/INT-method generally leads to an overestimation or underestimation of the integrated transports. This applies in particular to the more narrow straits of Lombok and Ombai.

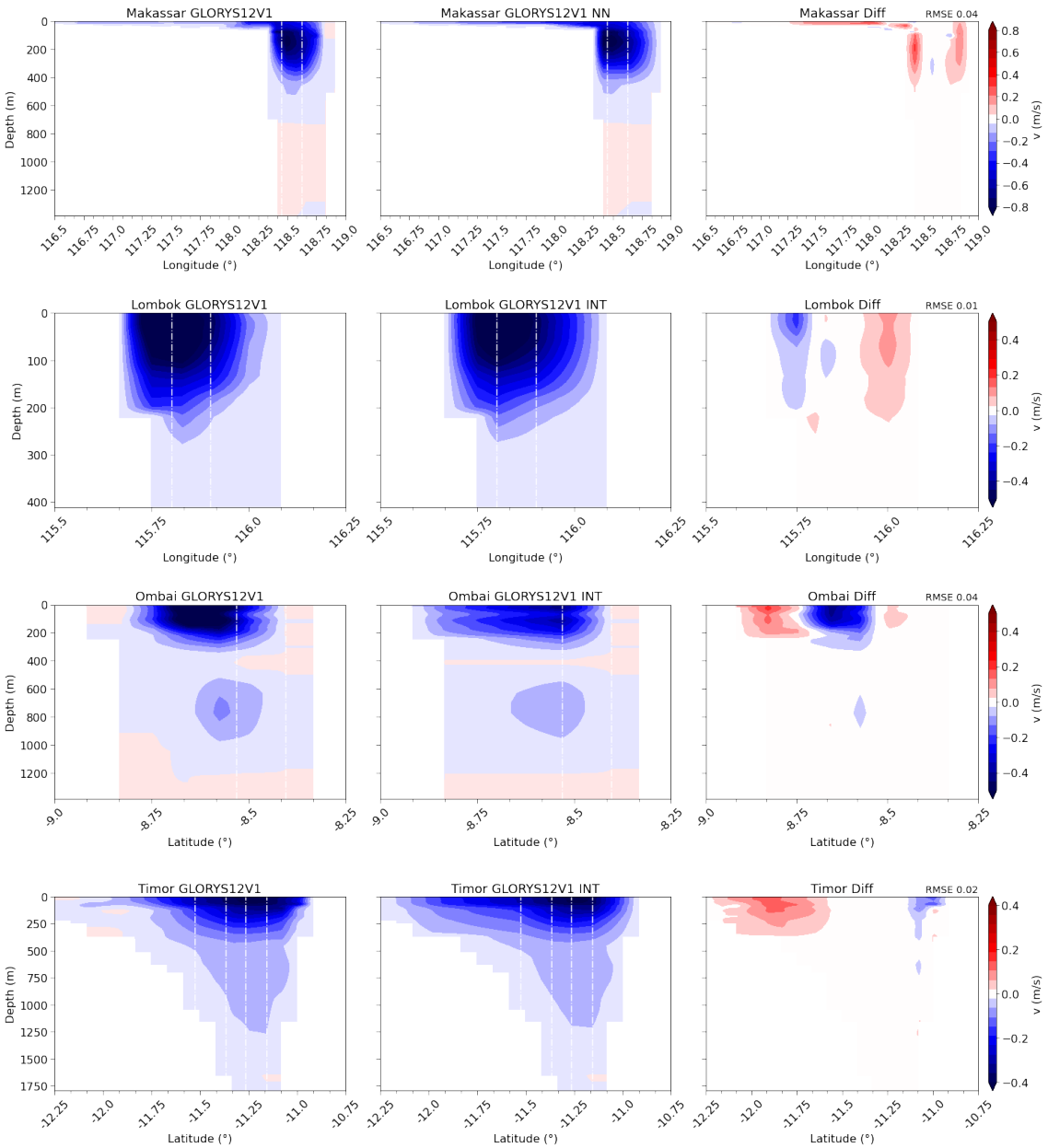

Figure 11: Mean ASV cross sections in Makassar Strait, Lombok Strait, Ombai Strait, and Timor Passage as given by the 1/12° bathymetry. The first column demonstrates GLORYS12V1 full-field integrated transports (2004-2006), the second column corresponding velocities using the NN/INT-methods, and the third column their differences. RMSE between full-field and NN/INT cross sections are given in the top right corner. Negative values indicate southward-directed velocities (toward the Indian Ocean). White dash-dot lines represent mooring locations. Note the change in depth and velocity scales.

As previously demonstrated, we can analyse the differences between full-field and extrapolated cross sections with respect to the higher resolving Reanalysis, GLORYS12V1. Figs. 11 show this comparison displaying the same composition as Figs. 10.
Contrary to the Reanalysis mean, GLORYS12V1 features six horizontal grid points within Labani Channel. Thus, the nearest neighbours (second nearest neighbour for the west mooring) at 118.5°E and 118.66°E yield a better match with the mooring locations at 118.45°E and 118.63°E. Indicated by the difference plot and an increase in the mean

integrated transport, from -9.5 Sv to -11.2 Sv (Tab. 4), the NN-method does, however, overestimate the full-field transport. The missing information from the grid points to the east of Labani Channel leads to an extension of the flow.

We find strong improvements with GLORYS12V1 in Lombok Strait. GLORYS12V1 finds the ITF core to the east and, given the more eastward located moorings, the INT-method reproduces the strong core accurately. The identical integrated transports of -2.5 Sv support this statement. The high agreement is further highlighted by a RMSE of 0.01 m/s.

In Ombai Strait, GLORYS12V1 shows similar behaviour to the Reanalysis mean in Figs. 10. Missing information south of 8.75°S extends the upper layer flow towards the south. However, the INT-method seems to disregard the central flow maximum leading to a transport decrease from -4.0 Sv to -3.4 Sv. Something that is not immediately clear considering the Reanalysis mean is the reason for the choice of the northern mooring location. With GLORYS12V1, we are able to retrace this choice which aims to capture the inflow in the northern regions.

In Timor Strait, we find a slightly poorer correspondence between the full-field cross section and the INT-method regarding GLORYS12V1. As with Makassar, integrated transport increases by choice of the INT-method. The INT-method extrapolates higher velocities to the south, there where the flow is otherwise decelerated by existing grid points. In view of GLORYS12V1, we find the following relation: the NN-method and, accordingly the INT-method tend to overestimate the transport in broad channels as extrapolation yields too high ASV values towards the sidewalls. In the much more narrow straits, Lombok and Ombai, the INT-method tends towards underestimating the integrated transport.

5.1.2. Vertical Profiles (INSTANT)

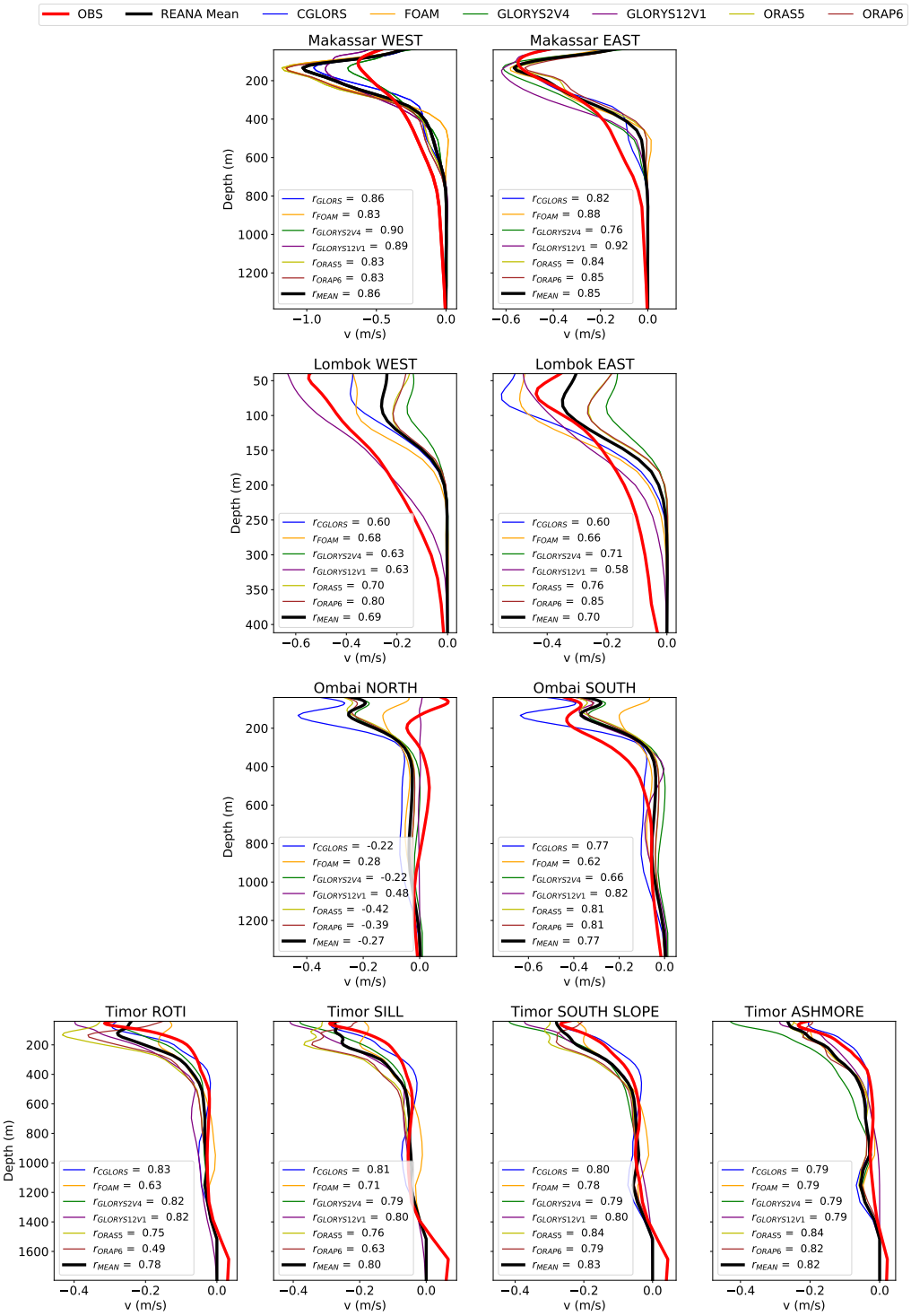

Figure 12: Mean ASV profiles (m/s) for Makassar Strait, Lombok Strait, Ombai Strait, and Timor Passage. Corresponding correlation coefficients are given by the legends in the lower left. Note the change in depth and velocity scales. Negative values indicate southward/westward-directed velocities (toward the Indian Ocean).

With respect to Figs. 8 and 9 we can compare mean vertical profiles of ASV. Table 4 displays integrated transport estimates using only the nearest neighbours or interpolated vertical profiles (third column). Here, we take a closer look at these profiles. The mean vertical profiles for Makassar Strait, Lombok Strait, Ombai Strait, and Timor passage are illustrated in Figs. 12. Moreover, mean vertical profiles are suitable presentations for discussing the advantages and disadvantages of the Reanalysis products.
In Makassar Strait, we consider the nearest neighbours to the west and east mooring. Regarding the 1/4° products, these are 118.5°E and 118.75°E, respectively. The nearest neighbours in GLORYS12V1 are 118.42°E and 118.66°E. The west mooring was exposed to higher currents according to Gordon et al. (2008). We find a maximum mean velocity of -0.63 m/s in ∼110 m in the observations. The Reanalysis mean displays a stronger maximum of -1.05 m/s in ∼130 m. GLORYS2V4, exhibiting a maximum velocity of -0.72 m/s in this very depth, displays the highest correlation with the observations ($r_{GLORYS2V4}$ = 0.90). Their high accordance is underlined by the fact that GLORYS2V4 and the observations both arrive at a mean transport of -10.7 Sv (Tab. A6). Its higher resolving version GLORYS12V1 yields an even higher velocity maximum of -0.87 m/s in ∼130 m as well, while the correlation hardly decreases. Here, we use the second nearest neighbour at 118.5°E, which coincides with the nearest neighbour from the 1/4° products. As shown in Figs. 8, the 118.5°E grid point is located to the east of the actual mooring location. The chosen grid point is thus closely located next to the reanalysis-generated ITF core, explaining the high mean ASV. With GLORYS12V1, the 118.5°E grid point is also situated within the core.
From a magnitude point of view, the agreement between observations and Reanalysis products improves with respect to the east mooring location. Note the change in velocity scales. We find a maximum value of mean ASV of -0.55 m/s in ∼110 m in the observations. The Reanalysis mean displays a similar maximum of -0.58 m/s, albeit in ∼130 m. This particular vertical shift appears at both mooring sites. The correlation coefficients register an overall weak decrease in correlation with the east mooring. While GLORYS2V4 displays now the weakest correlation ($r_{GLORYS2V4}$ = 0.76), the correlation between observations and GLORYS12V1 increases ($r_{GLORYS12V1}$ = 0.92), partly due to the noticeable agreement above ∼100 m.
Below ∼400 m, observations provide stronger mean ASV, indicating their advantage over Reanalysis products in greater depths. The information in greater depths might compensate for some of the strong velocities displayed by the products in the thermocline, causing the relatively small difference in mean transport values (Tab. 4).

The spread between observations and Reanalysis products increases in Lombok Strait. Again, observed ASV are stronger towards the West, coinciding with Figs. 8. We find an observed maximum of -0.56 m/s in ∼50 m, while GLORYS12V1, exhibiting a similar upper profile structure, increases towards the surface. Other than in broader straits, we find that the Reanalysis products tend to underestimate velocities. Unlike the observations, the Reanalysis mean displays higher velocities in the East, which we addressed in Figs. 6 and 8. This is also where the correlation between observations and Reanalyses increases. ORAP6 displays the highest correlations of 0.8 and 0.86 for West and East, respectively. Furthermore, the Reanalysis products indicate a weak subsurface maximum in ∼90 m, which also increases towards the East. Here, CGLORS (-0.56 m/s) and FOAM (-0.49 m/s) surpass the observed maximum of -0.44 m/s. Note the fact that the velocity scale decreased. We also find this subsurface maximum in the observations in around ∼70 m, similar to the

depth of the CGLORS maximum. The strong observed decrease towards the surface is most likely a result of using interpolation to fill NaN values near the surface. However, the 1/4° products also display a decline in velocity, despite having no NaN values. According to that, the almost constant flow between 0-100 m in Figs. 8 and 9 tend to result from the western vertical profiles.
Interestingly, GLORYS2V4 and GLORYS12V1 exhibit completely different structures and magnitudes. While GLORYS2V4 underestimates the observations, GLORYS12V1 tends towards overestimation above ∼170 m. Nonetheless, GLORYS2V4 displays stronger correlations in the East ($r_{GLORYS2V4} = 0.71$). The correlation coefficients deviate from each other by a maximum of 0.08 but do not provide a clear indication of where profiles agree better. As with Makassar Strait, the observations provide stronger mean ASV in greater depths.

Even though the two moorings in Ombai Strait are separated by only 14 km, the vertical profiles of ASV are completely different from each other. The northern mooring features both an eastward-directed surface flow and a westward-directed subsurface maximum of -0.05 m/s in ∼200 m. Apart from GLORYS12V1, the Reanalysis products all exhibit a similar vertical structure, albeit stronger. We attribute this to the fact that the GLORYS12V1 ASV profiles at 8.33°S and 8.41°S, used to create the profile at the mooring site (8.402°S), display velocities close to zero and partly even positive. After all, the northern mooring lies at a distance of 8 km from the coast, decreasing the 1/4° product capabilities and thus their ability to reproduce weak offshore flow. The Reanalysis profiles are strongly influenced by the vertical profile at 8.5°S because the profile at 8.25°S is near zero. We considered using the nearest neighbours and ended up with profiles around zero, similar to GLORYS12V1. The correlation coefficients underline the fact that this is not an ideal comparison. GLORYS12V1, with the highest correlation coefficient of 0.48, demonstrates its capabilities within narrow straits.
Since the southern mooring is located at 8.53°S, the 1/4° products are again strongly influenced by the profile at 8.5°S. This demonstrates the difficulty of handling only four grid points in a narrow strait. However, the correlations between observations and Reanalyses strongly improve. The correlation between observations and GLORYS12V1 increases to 0.82, closely followed by ORAS5 (0.81) and ORAP6 (0.81). We find both an observed surface maximum (∼20 m) and an equally strong subsurface maximum of -0.44 m/s in ∼165 m. The Reanalysis mean and GLORYS12V1 replicate this structure, albeit with vertically upward shifted maxima of -0.37 m/s and -0.38 m/s, respectively. The generally weaker maxima become noticeable considering mean integrated transports in Tab. 4. At the same time, the interpolated vertical profiles in Ombai North are clearly the reason for the higher Reanalysis mean INT value. Obvious outliers are represented by CGLORS and FOAM, which according to Figs. A42 have a considerable vertical resolution but completely deviate in terms of magnitude.

There are noticeable discrepancies between the Reanalysis products in the upper 200 m of Timor Passage. This holds especially true for Timor Roti and Timor Sill. While GLORYS12V1 and GLORYS2V4 indicate surface intensified flow, the remaining products exhibit distinct subsurface maxima of up to -0.44 m/s. GLORYS12V1 and GLORYS2V4 also reveal high correlations of 0.82 in Timor Roti. We find an observed maximum of -0.32 m/s in ∼60 m. ORAS5 and ORAP6 are responsible for shifting the weaker Reanalysis mean maximum (-0.28 m/s) towards a depth of ∼120 m. FOAM follows a vertical structure, unlike any other product. Moreover, the observations correlate highest with CGLORS

($r_{CGLORS} = 0.83$). This remains true for Timor Sill, where we find an observed maximum of -0.29 in ∼60 m. CGLORS displays a maximum of -0.29 m/s in a slightly greater depth of ∼70 m. The correlation with the Reanalysis mean increases, albeit the double subsurface maxima structure in ORAS5 and ORAP6. Also, note the increasing spread between those products toward the surface at all four mooring sites. This spread already exists in the original profiles, suggesting a connection to the difference in atmospheric forcing. We addressed the observed minimum below ∼1400 m in Figs. 7, and the present profiles prove that Reanalyses do not capture it. Besides, 1/4° products provide information down to a depth of 1265 m at all mooring sites. GLORYS12V1 captures depths of ∼ 2000 m in Roti, Slope, and Sill, and with the Timor Sill mooring measuring in depths of 1800 m, the vertical limit of the comparison is determined.
Similar to Timor Sill, GLORYS2V4 and GLORYS12V1 display strong surface intensified profiles at Timor South Slope, while ORAS5 and ORAP6 maintain two subsurface maxima. Nonetheless, their correlation with the observations steadily increases towards the South of the strait. We find an observed ASV maximum of -0.27 m/s in ∼55 m which is again well captured by CGLORS (-0.27 m/s in ∼60 m). The correlation between observations and the Reanalysis mean further increases, suggesting that the performance of the 1/4° products improves towards the middle of the strait, where they are no longer influenced by the coast or shelves.
Apart from GLORYS2V4, discrepancies between Reanalysis products are lowest at Timor Ashmore. However, this is mainly due to generally weaker velocities. Note that to the South of the Ashmore mooring, there is no coastline but the Ashmore Reef. The observed maximum decreases down to -0.24 m/s as well and deepens (∼70 m). As with Timor South Slope, the highest correlation with observations bears ORAS5, which also agrees with the observed maximum in ∼70 m. All 1/4° products follow a distinct second deep sea maximum in around 1200 m, marking the origin of the maximum we found in Figs. 6. This is also the case with the Timor South Slope mooring, where the agreement with the observations is even higher.

Overall, we find cross-strait differences in the strength of the flow in almost every strait. In Makassar, the western side is stronger than the east, in Lombok the western side is stronger than the east, and in Ombai, the southern side carries nearly all the ITF. These discrepancies are also evident from the mean cross sections of ASV in Figs. 6 and 7. Oftentimes, the Reanalyses struggle to get the asymmetries in the flow through the straits. After consulting Dr. Janet Sprintall, she confirmed that this is not an uncommon problem in models. Besides, small-scale properties such as the eastward-directed flow in the North of Ombai Strait are almost impossible to reproduce with 1/4° products. This is where GLORYS12V1 holds an advantage.

5.1.3. Performance Test (INSTANT)

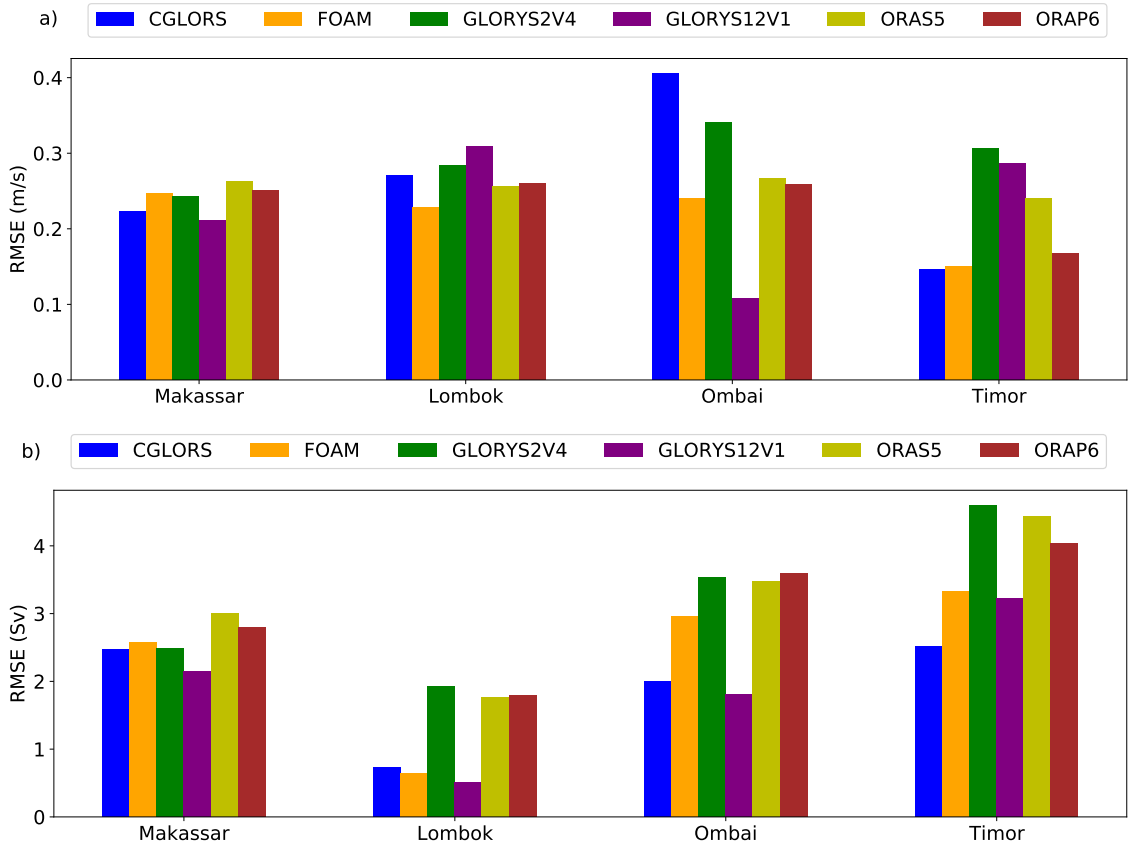

Figure 13: Reanalyses performance. a) Time-averaged RMSE of vertical velocity profiles and b) RMSE of monthly averaged full-field integrated transports between observations and Reanalysis products in the observed straits (Makassar, Lombok, Ombai, and Timor) during the INSTANT period from 2004-2006.

In an attempt to find the strait where Reanalysis performances are highest, we compute the RMSE between observations and Reanalyses. We choose two different ways of representation: 1) RMSE computed across the depth of time-average observed and reanalysis-based velocity profiles (Figs. 12) and determination of the average in each strait (Fig. 13a)

$$RMSE_{ASV} = \sqrt{\frac{1}{n}\sum_{i=1}^{n}(\overline{OBS} - \overline{REANA})^2}, \tag{45}$$

where $\overline{OBS}$ and $\overline{REANA}$ refer to temporally-averaged ASV profiles, and n denotes the number of vertical layers. 2) RMSE computed over time of monthly mean integrated volume fluxes (Fig. 13b). Here, we make use of full-field integrated transports

$$RMSE_{Transport} = \sqrt{\frac{1}{m}\sum_{i=1}^{m}(OBS - REANA)^2}, \tag{46}$$

where OBS and $REANA$ refer to time series of monthly transports, and m indicates the number of months.

Considering Fig. 13a and thereby ASV profiles product performance is generally highest in Timor followed by Makassar. Compared to Timor, there is little variability between the Reanalyses products in Makassar, with GLORYS12V1 (0.21 m/s) performing best. Note that we employ the nearest neighbours in Makassar and interpolated profiles in Lombok, Ombai, and Timor. Due to the higher resolution in GLORYS12V1, the nearest neighbours are automatically located closer to the mooring locations, yielding a better agreement.
The situation reverses in Lombok Strait, where we find the highest RMSE in GLORYS12V1 (0.31 m/s), whereas FOAM (0.25 m/s) scores best. The high RMSE is most likely a result of the overly strong surface intensified flow we find in GLORYS12V1 (Figs. 7). The availability of four horizontal grid points (in GLORYS12V1) does not lead to an improvement, and GLORYS2V4 (0.28 m/s) outperforms GLORYS12V1. While products like CGLORS (0.27 m/s), ORAS5 (0.25 m/s), and ORAP6 (0.26 m/s) are able to mimic the shape of the observed vertical profiles, FOAM (0.25 m/s) most likely manages to keep up in terms of magnitude as well.
There is high variability between the products in Ombai Strait. CGLORS (0.41 m/s), strongly overestimating velocities in the particularly relevant upper ∼200 m (Figs. A42), scores worst. A clear advantage holds GLORYS12V1, which has four horizontal grid points at its disposal, whereas the 1/4° products capture only two. That being said, narrower spacing between grid points evidently yields more representative profiles. We assume this to be the case in Lombok Strait as well. Furthermore, GLORYS12V1 detects the region of eastward flow in the North, there where one of the moorings was anchored. The 1/4° products strongly overestimate this region, with FOAM (0.24 m/s) coming closest and thus scoring the second best RMSE. Differences between GLORYS2V4 (0.39 m/s) and GLORYS12V1 (0.1 m/s) are highest in Ombai Strait.
Figs. 12 already highlighted notable correlations and minor discrepancies in magnitude between observations and CGLORS at each mooring location in Timor. As a matter of fact, CGLORS (0.14 m/s) and FOAM (0.15 m/s) portray a similar flow regime as represented in Figs. A43, already implying similar performance skills. GLORYS2V4 (0.31 m/s) and its higher resolving version GLORYS12V1 (0.29 m/s) both generate strong surface intensified flows, increasing the RMSE in the near-surface layer.
The fact that ORAS5 and ORAP6 share the same origin, albeit with different atmospheric forcings, is reflected by their similar performance scores throughout the straits. Even if only by a margin, ORAP6 seems to perform better in deeper straits (Makassar, Ombai, and Timor).

The clear advantage GLORYS12V1 holds over the 1/4° products, shows in Fig. 13b. The placement in product performance barely changes in Makassar. Note that the observed and reanalysis-based integrated ITF transports are strongest in Makassar. The relatively high RMSE we find in ORAS5 (3.0 Sv) is connected to the strong mean transport (Tab. A6) and most likely a cause of the strong westerly ASV profile in Figs. 12.
The comparatively high scores in Lombok Strait are partly a result of its small mean transport. Both the vertical profiles in Figs. 12 and the mean integrated transports in Tab. A6 confirm the underestimation we find with ORAS5 (1.77 Sv), ORAP6 (1.79 Sv), and especially GLORYS2V4 (1.93 Sv), which leads to high RMSE. The strong surface intensified flow we find in GLORYS12V1 (0.51 Sv) influences the temporal RMSE to a lesser extent, yielding a notable performance nonetheless. The advantages in CGLORS (0.73 Sv) and FOAM (0.65 Sv) can be understood by looking at Figs. A41, where their similar cross sections are displayed, and furthermore, their common features with GLORYS12V1

regarding the strong surface flow.
Considering Ombai Strait and its similar width to Lombok Strait, we find an equally well representation by GLORYS12V1 (1.8 Sv). In contemplation of Figs. A42, CGLORS (2.0 Sv) is the only product imitating the two core ITF structure and the deep-reaching higher velocities around 8.5°S. They can also be found in FOAM (2.96 Sv) but with an extenuated upper layer flow. As before, discrepancies between ORAS5 and ORAP6 remain small not only in Ombai Strait but also in general, with ORAS5 exhibiting a minor advantage in narrow straits while ORAP6 dominates in broader straits. Their performance skills are thus dependent on whether temporally-averaged ASV profiles or transport time series are investigated. In addition, abilities to capture the cross-sectional distribution of velocities seem to play a more prominent role in $RMSE_{Transport}$, whereas a low $RMSE_{ASV}$, requires the reproduction of velocity asymmetries within the straits.
Given that the average integrated transport in Timor is about 4 Sv less than in Makassar, RMSE are comparatively high. GLORYS12V1 (3.21 Sv), still exhibiting an advantage, is, however, outperformed by CGLORS (2.52 Sv). This is supported by the accurate agreement between the observed and reanalysis-based mean transports in Tab. A6. Furthermore, CGLORS and also FOAM are the only two products that distinguish between the upper layer flow and the weaker maximum in greater depths.
While differences between the related products GLORYS2V4 and GLORYS12V1 remain small in Fig. 13a, we find more severe deviations regarding the temporal RMSE. Differences between Figs. 13a and 13b are nothing out of the ordinary because, while the nearest neighbours and interpolated profiles conform with the observed profiles, the remaining grid points might lead the monthly integrated transports towards an over- or underestimation. That being said, Fig. 13a rather conforms with the NN-method/INT-method, while Fig. 13b considers all horizontal grid points.

5.1.4. Seasonal Cycle (INSTANT)

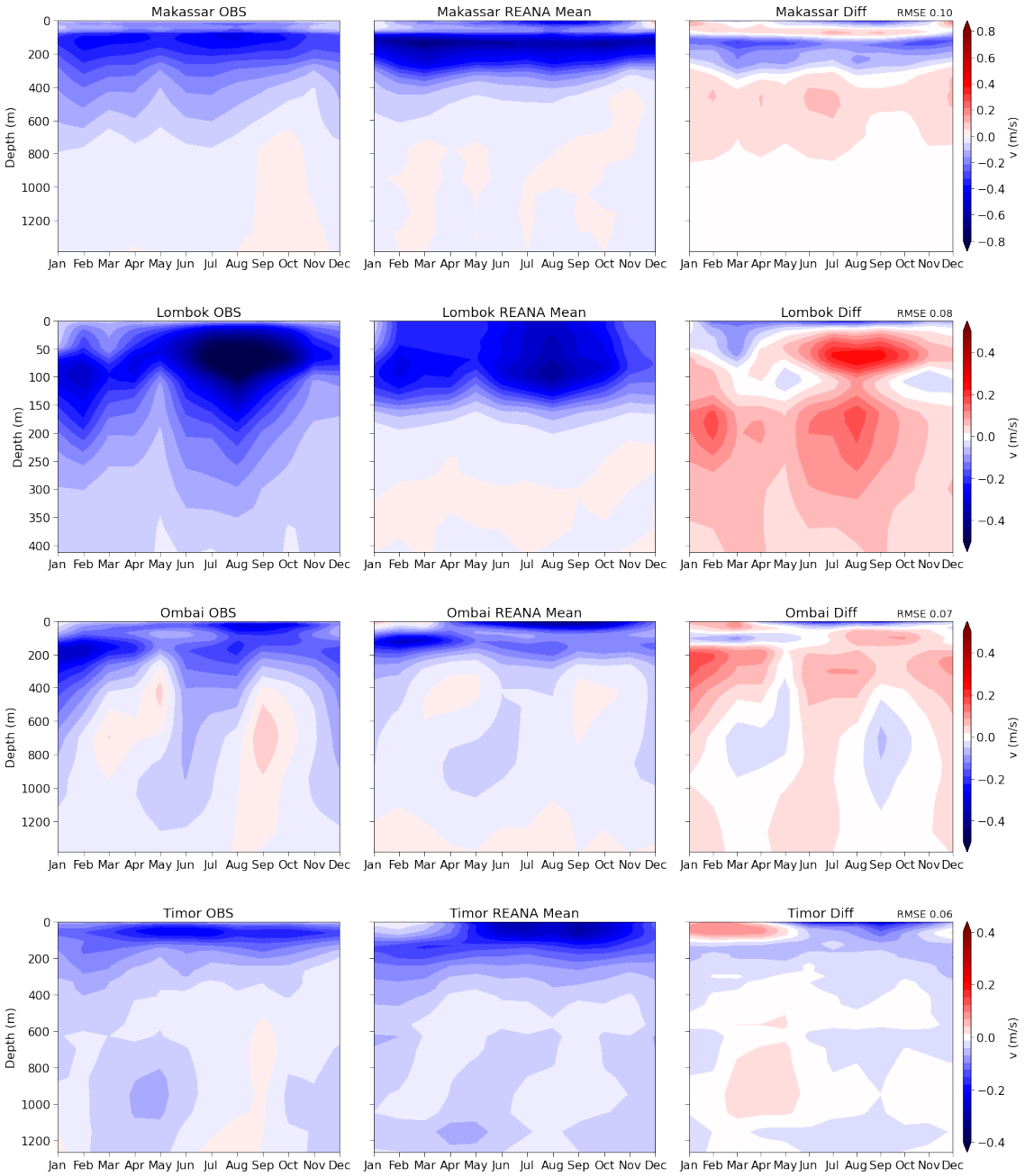

Figure 14: Seasonal cycle of ASV for Makassar Strait, Lombok Strait, Ombai Strait, and Timor Passage as given by the 1/4° bathymetry. The first column demonstrates observations (INSTANT Program, 2004-2006), the second column the Reanalysis Mean, and the third column their differences. RMSE between the Reanalysis mean and observations are given in the top right corner. Negative values indicate southward transport (toward the Indian Ocean). Note the change in depth and velocity scales.

Similarly to Figs. 6 and 7 we introduce the seasonal cycle of ASV within Makassar Strait, Lombok Strait, Ombai Strait, and Timor Passage, covering the INSTANT period from January 2004 to December 2006. Again, we analyse both bathymetries, 1/4° (Figs. 14) and 1/12° (Figs. 15). The Hovmoeller representation reveals seasonally dependent activities

even in deeper layers.

The apparent thermocline maximum around 110 m and 140 m for the observations and the Reanalysis mean, respectively, is clearly represented in the seasonal cycle in Makassar Strait. We mentioned earlier that the profile varies with season. Generally, the thermocline maximum increases during the southeast monsoon (June/July/August/September) and decreases during the northwest monsoon (December/January/February/March), which is confirmed by the observations in Figs. 14. The Reanalysis mean reproduces this seasonal cycle near the surface in the upper 80 m rather than within the thermocline. Minimum transport in May and the even stronger reduction in November (absolute seasonal minimum) have been attributed to the effect of Kelvin waves generated during the monsoon transition months, April-May and October-November (Sprintall et al., 2000). These waves develop in the equatorial Indian Ocean and propagate along the coast of Sumatra and Java to the ITF outflow passages. By way of Lombok Strait, they can impact the ITF in Makassar Strait by reducing the flow or even reversing it (Pujiana et al., 2013). The weak reversal is displayed by the distinct light pink shading in the observations, however, only during October/November. Furthermore, Kelvin waves seem to appear in deeper layers first before influencing the ITF in the upper layer. By comparison, the Reanalysis mean detects weak northward transports in deeper layers, however, displaying a differing structure. There is slight evidence of the appearance of Kelvin waves in the monsoon transition months.
Maximum transport occurs towards the end of each monsoon phase, visible during March-April in the observations and during March in the Reanalysis mean's thermocline. The maximum at the end of the SE monsoon is not as pronounced in this representation. The difference plot highlights the shift of the thermocline maximum between observations and the Reanalysis mean. In addition, the Reanalysis mean lacks information below ∼400 m, however, both of these facts have been found in previous results.

We find a similar seasonal cycle within Lombok Strait with maximum transport during the SE monsoon and minimum transport during the NW monsoon. After all, Lombok Strait is the direct exit passage for water masses transitting through Makassar Strait. Furthermore, maximum flow during boreal summer occurs around 50 m, whereas the main flow shifts vertically downward to ∼100 m depth during the NW monsoon. The result is a weak surface flow in boreal winter. The maximum transport during boreal summer is visible in the Reanalysis mean, albeit weaker and vertically shifted (∼100 m). The reduction in surface flow during the NW monsoon is barely reproduced by the Reanalysis mean. As a matter of fact, the Reanalysis mean overestimates the generally weaker flow during the NW monsoon and strongly underestimates the overall stronger flow during the SE monsoon.
Lombok Strait represents the first entrance section for Kelvin waves propagating from the equatorial Indian Ocean along the coast of Sumatra and Java into the Indonesian Seas. Accordingly, we find a reduction of flow in May and an even higher reduction in November with a distinct upward phase propagation. However, this is barely represented in the Reanalysis mean, and the difference plot reveals an overall underrepresented deep layer flow.

Ombai Strait displays a similar vertical phasing as Lombok Strait in the seasonal cycle: the surface and subsurface flow are out of phase during the monsoon phases. This is even more pronounced within Ombai. During the NW monsoon the main ITF core is subsurface, extending from 100 to ∼400 m. However, the core shifts toward the surface during the SE

monsoon. The Reanalysis mean captures the vertical phasing and displays an even stronger surface maximum during the SE monsoon, though a weaker and less vertically expanding subsurface maximum during the NW monsoon. In addition, the surface flow even reverses. Sprintall et al. (2009) state that some of the Kelvin wave energy evoking reductions in Lombok Strait, and as far as Makassar Strait, moves further along the Nusa Tenggara island chain to Ombai. Kelvin waves are represented by the distinct upward phase propagation in the observations. From March to May, the reversed flow is found between 300 and 900 m and from August to October between 400 and 1400 m. According to Sprintall et al. (2009), the difference in phase propagation is related to the circulation around Sumba Island, to the West of Ombai. Depending on the pathway the waves are following around the Island, vertically different phase propagation patterns occur. With such fairly local effects, the limits of the Reanalysis products can be assessed. We find that the Reanalysis mean reproduces the phase propagation pattern, however, less pronounced.

Within Timor Passage, observations display a generally steadier flow in the upper layer. We find minimum flow from December to February and maximum flow from April to July. Furthermore, the flow seems to be out of phase between Ombai and Timor. During the SE and NW monsoon, when the ITF transport in Ombai is strong, Timor transport is reduced. When the transport through Ombai Strait is at a minimum in the monsoon transition periods, Timor transport increases, suggesting that the Kelvin waves partly control the seasonal cycle of ITF transport as also found by Sprintall et al. (2009). This concept is also referred to as gating (Sprintall et al., 2019). Besides, according to Peña-Molino et al. (2022), transport in Timor Passage is regulated by the inflow from Makassar Strait and storage capacity in the surrounding seas. Makassar transport increases in June, and thus we expect the flow in the upper layer in Timor to increase as well. However, the flow seems to decrease again, and at the same time, a Kelvin wave signal appears in greater depths. Sprintall et al. (2009) and Peña-Molino et al. (2022) attribute this signal to Kelvin wave energy grazing Ombai Strait and propagating further into Timor Passage.
The Reanalysis mean, on the other hand, follows the upper vertical phasing we found in Ombai Strait, exhibiting considerably weak flow from January to March. The positive maximum in the difference plot signals this. Overall, seasonal variability is clearly greater in Ombai and Lombok, while these are also in phase.

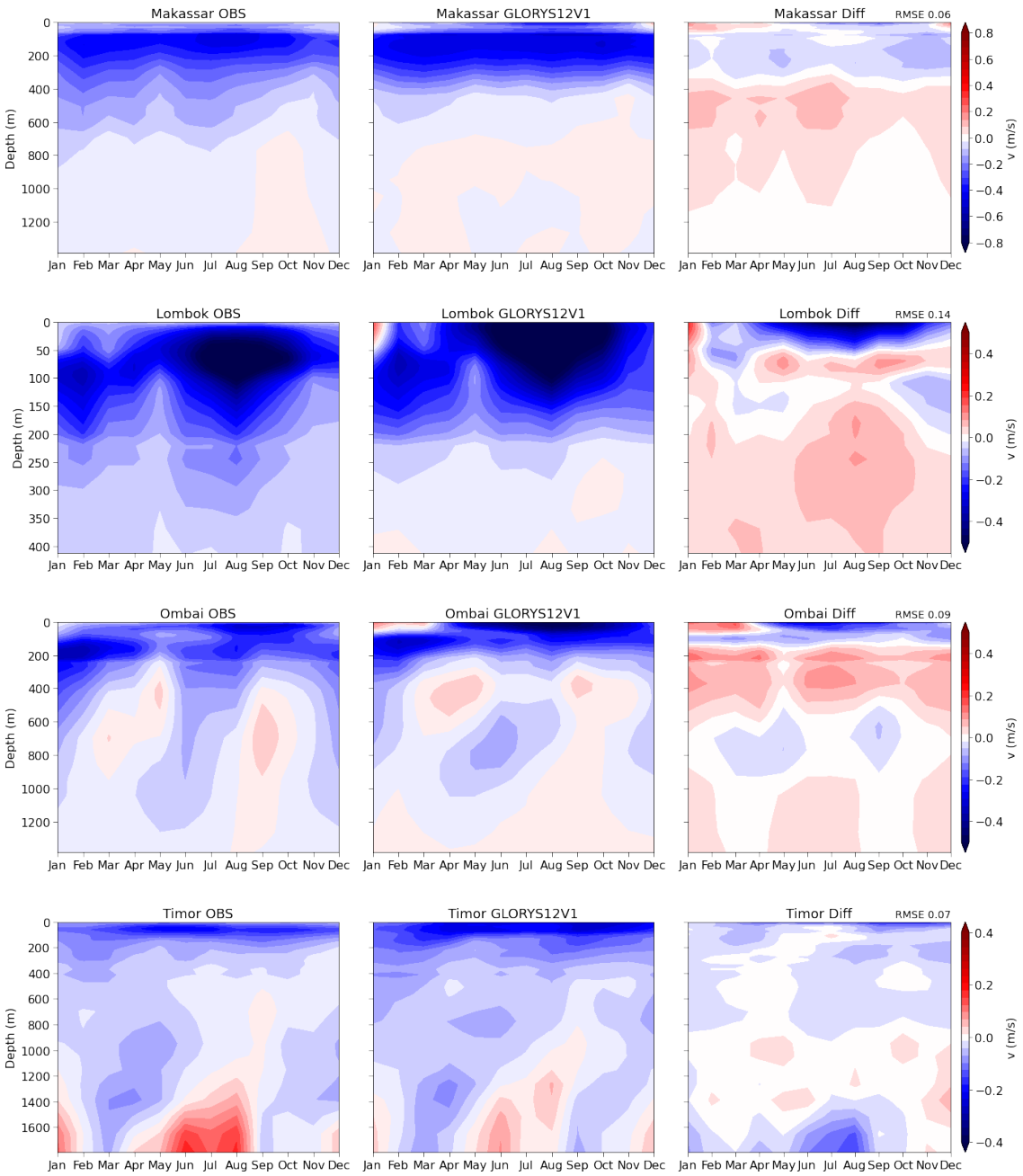

Figure 15: Seasonal cycle of ASV for Makassar Strait, Lombok Strait, Ombai Strait, and Timor Passage as given by the 1/12° bathymetry. The first column demonstrates observations (INSTANT Program, 2004-2006), the second column GLORYS12V1, and the third column their differences. RMSE between GLORYS12V1 and observations are given in the top right corner. Negative values indicate southward transport (toward the Indian Ocean). Note the change in depth and velocity scales.

Highlighting the advantages GLORYS12V1 entails regarding the seasonal cycle is the subject of the following section. We compare observations within the 1/12° bathymetry with GLORYS12V1 while also discussing apparent improvements with respect to the Reanalysis mean.

The 1/12° mask highlights the second maximum in Makassar Strait during the SE monsoon more distinctly. Similar to the Reanalysis mean, GLORYS12V1 exhibits a more distinct

surface maximum during the SE monsoon. The reduction of the flow in May and November is also only slightly indicated by GLORYS12V1. It does, however, generate more deep-sea activity. Regarding the difference plot, we find a similar pattern as in Figs. 14, that is, an overestimation of velocities in GLORYS12V1 in the thermocline and weak flow below ∼400 m.

Compared to the Reanalysis mean, the structure of the seasonal cycle pattern in Lombok Strait considerably improves regarding GLORYS12V1. The subsurface maximum during the NW monsoon and the higher located maximum during the SE monsoon are both reproduced by GLORYS12V1. High discrepancies at the surface correspond to the already mentioned surface intensified flow in GLORYS12V1. Besides, measurements from the ADCP can be subject to reflections at the surface, thus, data within the first ∼40 m must be interpreted with caution. The weak northward signals in greater depths are placed more discretely, indicating some Kelvin wave-induced activity around October. Another upward-reaching minimum in May coincides with the one found in the observations. The vertical structure below ∼200 m is still underrepresented in Reanalyses.

The vertical structure of the seasonal cycle in Ombai Strait hardly changed with GLORYS12V1, but the intensity increased. Both Lombok and Ombai denote an eastward-directed flow near the surface in January. In Ombai Strait, this even extends to March. Although the observed flow decreases, there is no visible reversal during the NW monsoon. Kelvin wave activity seems to be more strongly represented by GLORYS12V1 compared to the Reanalysis mean.

Note the extension of the depth scale from 1250 m to 1800 m in Timor Passage. With the 1/12° bathymetry, we are able to analyse the deep sea seasonal cycle as well. The ITF core remains within the upper ∼200 m in GLORYS12V1, however, the temporal distribution improved. The upper vertical phasing does not correspond to Ombai Strait anymore, but to the increased flow within Makassar Strait, although with an approximately 1-month lag. Supported by the difference plot, there is now a better agreement between observations and Reanalyses.
In Figs. 14, we mentioned the transferred effect of Kelvin waves in Timor Passage. The distinct northward transport in greater depths, and especially below ∼1400 m, can be attributed to this energy. According to Sprintall et al. (2009), some of the eastward propagating Kelvin wave energy is guided along the sill depth of Savu Sea, between Ombai and Timor, causing the flow to reverse. GLORYS12V1 accurately reproduces the deep reversals towards the internal seas in boreal summer, albeit at weaker speeds. Besides, there is an apparent lag of 1-2 months between the positive maxima near the sea floor and the actual monsoon transition months (April/May and October/November). This is true for both the observations and GLORYS12V1. According to Drushka et al. (2010), it is possible that Kelvin waves do not reach Timor Passage until June at depths below 1500 m.

5.1.5. Mean Seasonal Cycle (INSTANT)

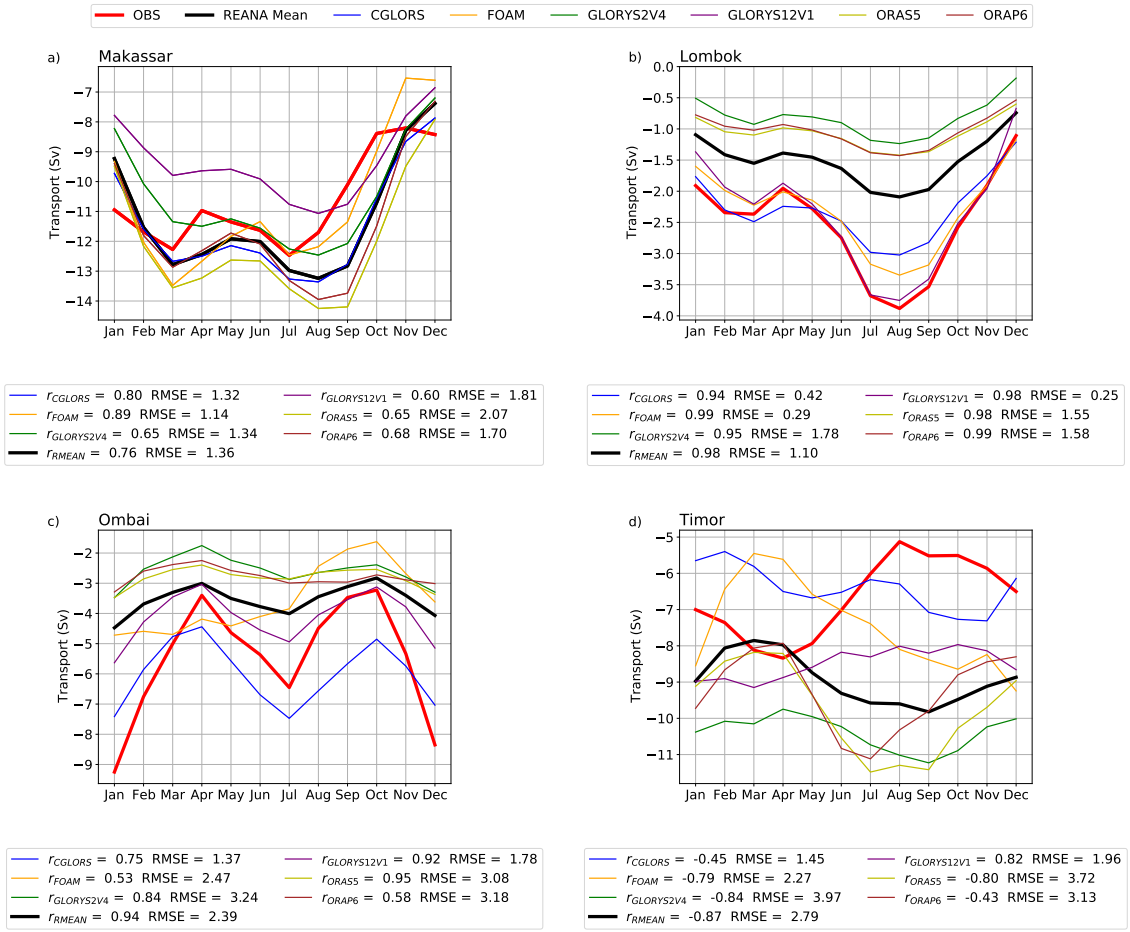

Figure 16: Mean seasonal cycle of ITF transport in a) Makassar Strait, b) Lombok Strait, c) Ombai Strait, and d) Timor Passage as represented by observations and Reanalysis products during the INSTANT program (2004-2006). Monthly time series are filtered with a 3-month moving average. Negative values indicate southward-directed transport (toward the Indian Ocean). Subjacent boxes display Pearson correlation coefficients r and RMSE.

Figs. 14 and 15 display the seasonal cycle of ASV in each strait. At this point, we want to focus on the mean seasonal cycles of integrated volume fluxes. For reasons of comparability, seasonal cycles in Figs. 16a-d cover the INSTANT period from 2004 to 2006, which means that we average over three months (e.g., three Januarys) at most. This is crucial to remember when interpreting the data in Figs. 16a-d. Table 5 displays corresponding seasonal fluctuations.

The seasonal cycle of ITF transport depends strongly on the Australian-Indonesian monsoon and, thus, on variabilities in sea level between the western Pacific and the eastern Indian Ocean. Focusing on the main ITF inflow passage, Makassar (Fig. 16a, Tab. 5), we gather that sea level differences must increase during boreal summer (SE monsoon), yielding a period of maximum transport, peaking in July (-12.5 Sv). Minimum transports prevail in boreal winter (NW monsoon), indicating minor sea level differences. We find this to be reproduced by all Reanalysis products. Absolute minimum transports in April (-10.9 Sv) and November (-8.2 Sv) correspond to monsoon transition periods and are better estimated

by the Reanalyses in April/May. The apparent time lag of one month - predominant in July/August - between the products and observations will be addressed in the next section. As measured by correlation coefficients r and RMSE, 1/4° products generally capture the seasonal cycle more accurately compared to GLORYS12V1. Not only do we find a decrease in correlation, but integrated transports are noticeably underestimated from January to August. That being said, the majority of the coarser resolving products tend to overestimate volume fluxes during most of the year, albeit less strongly. Merest deviations occur in FOAM (RMSE = 1.14 Sv), exhibiting high correlations as well. We also find that Reanalyses generate more extreme transport values during boreal winter and summer, with ORAS5 taking the lead in summer and GLORYS2V4 in winter.

There is a distinct partition between products in Lombok Strait (Fig. 16b, Tab. 5). While GLORYS2V4, ORAS5, and ORAP6 tend to underestimate the seasonal cycle throughout the year, we find less RMSE-based discrepancies with CGLORS and FOAM, and especially GLORYS12V1. Note that this is consistent with our findings in Fig. 13b. Overall, the seasonal cycle follows that of Makassar: maximum transport during boreal summer and minimum transport in boreal winter, with peak transports occurring in December (-1.1 Sv) and August (-3.9 Sv). After all, Lombok represents the direct outflow passage into the Indian Ocean. We find significant correlations (r = [0.94; 0.99]) with all products. The accurate reproduction in GLORYS12V1 (Min -0.7 Sv; Max -3.8 Sv) speaks in favor of its ability to resolve narrow straits more rigorously. Focusing on the 1/4° products, we find FOAM to score the highest correlations while also exhibiting a low RMSE (Min -1.2 Sv; Max -3.3 Sv).
Contrary to Makassar, observations display the highest transport values in boreal winter and summer. The monsoon transition periods are much more pronounced in April/May (-1.9 Sv) with accurate representation in FOAM (-2.0 Sv) and GLORYS12V1 (-1.9 Sv).

The seasonal cycle in Ombai Strait (Fig. 16c, Tab. 5) features distinct episodes of relaxation during the monsoon transition months, April (-3.4 Sv) and October (-3.2 Sv). These have been attributed to the passage of Kelvin waves. As shown in Figs. 12, vertical profiles at Ombai North and Ombai South are completely different from each other. While flow above ∼100 m at Ombai North is eastward throughout the year, it is westward at Ombai South, suggesting complex phasing across the strait. Maximum transport occurs during the NW monsoon (Max in January -9.3 Sv), when both Ombai North and Ombai South detect a strong subsurface maximum. During the SE monsoon, when surface and subsurface maxima compensate each other at Ombai North, Ombai South displays two equally strong maxima in the upper 200 m. The result is a period of maximal transport in summer (Max in July -6.5 Sv) which is, however, weaker than during the winter months. Since both of these profiles determine the cross-passage ASV structure and, thus, the integrated transports, we try to base our explanations on them.
Overall, Reanalyses support our observational-based findings, with the highest correlations in ORAS5 (r = 0.95) and the most accurate scaling in CGLORS (Min -7.4 Sv; Max -7.5 Sv). However, CGLORS makes the exception of overestimating integrated transports between April and November. The remaining products tend to underestimate the seasonal cycle throughout the year. FOAM (r = 0.53) gravitates towards a negative correlation during the first half of the year while adapting from July onwards with absolute minimum transport in October (-1.6 Sv). Apart from CGLORS, the highest transport values are dominated by observations.

Mean seasonal cycles strongly deviate in Timor Passage (Fig. 16d, Tab. 5). Furthermore, correlation coefficients between observations and most Reanalysis products indicate a negative correlation. Observed (Reanalysis mean) minimum transports occur from August to October (February to April) with maximum transports between March and May (July to September), implying a reversed seasonal cycle. Considering the different seasonal patterns in the upper layer ($< \sim$200 m) flow, we discussed in Figs. 14, we can trace back the origin of such strong deviations.
Observed transport is at a minimum in August to September (Min in August -5.1 Sv). Sprintall et al. (2009) have partly attributed this to Kelvin wave-induced deep sea reversals that are hardly resolved by the 1/4° products. During the monsoon transition periods of April/May (-8.3 Sv) and October/November (-5.9 Sv), when transport through Ombai is at a minimum, Timor transport increases. Following this path of comparing Ombai and Timor, we further find that minimum transports in July/August and December/January (-6.5 Sv) correspond to high ITF transports in Ombai. This behaviour underlines what we examined in Figs. 14.
GLORYS12V1 displays a particularly weak seasonal cycle, ranging from -7.8 to -8.9 Sv. The by far highest correlation exists between observations and GLORYS12V1 ($r = 0.82$). Considering the low variability in GLORYS12V1, we cannot exclude the fact that this is the reason for such a high correlation. The significance test using significance barriers, introduced in chapter 4.6, yields a 90% (lag = 0) probability of being explained by a real signal. However, this result must be interpreted with caution as we are dealing with short time series. At this point, the Timor Strait time series exhibits the downside of working with short time series.

Table 5: Makassar, Lombok, Ombai, and Timor integrated transports by season during the INSTANT observational period. Transport averages are given in Sverdrup (Sv = 10^6 m^3/s) with negative values indicating southward-directed transport (towards the Indian Ocean).

Makassar	DJF	MAM	JJA	SON
OBS	-10.5	-11.9	-11.5	-8.9
REANA Mean	-9.7	-12.7	-12.4	-10.9
GLORYS12V1	-7.9	-10.6	-9.7	-9.5

Lombok	DJF	MAM	JJA	SON
OBS	-1.9	-3.4	-2.2	-2.7
REANA Mean	-1.1	-1.9	-1.5	-1.6
GLORYS12V1	-1.4	-3.4	2.1	-2.6

Ombai				
OBS	-7.9	-5.4	-4.3	-4.0
REANA Mean	-4.0	-3.7	-3.3	-3.1
GLORYS12V1	-4.9	-4.5	-3.5	-3.5

Timor				
OBS	-7.0	-6.1	-8.1	-5.6
REANA Mean	-8.6	-9.5	-8.2	-9.5
GLORYS12V1	-8.4	-7.9	-8.3	-7.9

5.1.6. Cross correlation Makassar (INSTANT+MITF)

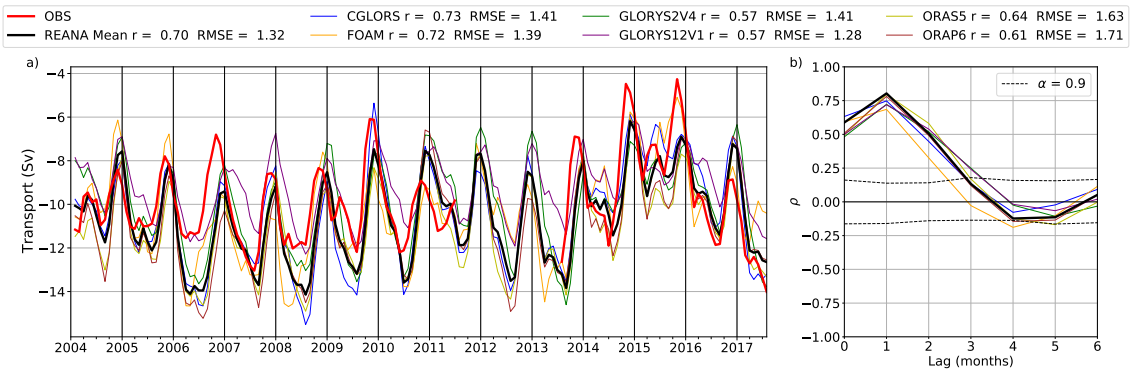

Figure 17: a) Full-depth integrated transport (Sv) through Makassar Strait between 2004-2017 (INSTANT and MITF program) as represented by observations and Reanalysis products. Legend displays Pearson correlation coefficients r and RMSE. Negative values indicate southward-directed transport (towards the Indian Ocean). b) Corresponding cross correlations over six lags. Black dashed lines represent significance barriers, generated from two pairs of 300 AR(1) processes with $\alpha = 0.9$.

As already mentioned with regard to Fig. 16a, we analyse the apparent time lag of one month in Makassar Strait. The seasonal cycle in Fig. 16a covers the 3-year INSTANT period, however, the lag appears in the extended time series as well. This is clearly visible in Fig. 17a, where we employed a three-month moving average to smooth the time series. In view of correlation, such a lag raises the question of randomness. To answer this question, we assess the significance of the correlation using the method described in section 4.6. Due to the repetition brought forward by the seasonal cycle, we focus on the first seven months. The cross correlation between observations and Reanalysis products is highest at lag = 1, displaying maximal values of $\rho_{max,ORAS5} = 0.79$ and $\rho_{max,ORAP6} = 0.78$. We find this lag within all Reanalysis products, even CGLORS ($\rho_{max,CGLORS} = 0.75$), which, according to the correlation coefficient ($r_{CGLORS} = 0.73$) and RMSE (1.41 Sv), reproduces observations best. Averaged over 48 months and using a high damping coefficient of $\alpha = 0.9$, the upper ρ_u and lower ρ_l significance barriers correspond to 0.165 ($\sigma^2 = 2.5{\cdot}10^{-4}$) and -0.166 ($\sigma^2 = 2.2{\cdot}10^{-4}$), respectively. The AR(1) generated significance barriers mark the area of significant cross correlations above the 95% confidence level and indicate that apart from GLORYS2V4 and GLORYS12V1, correlations become insignificant after lag = 2. FOAM and ORAS5 exceed the lower barrier one more time at lag = 4 and lag = 5, respectively. Summarising the information we gain from Figs. 17, cross correlations between observations and Reanalyses at lag = 1 are, in fact, based on a real signal.

5.1.7. Anomaly Time Series (INSTANT+MITF)

Before analysing the transport through Makassar and its connection to the sea level gradient and ENSO, we focus on differences and commonalities between observations and Reanalyses in anomaly time series.

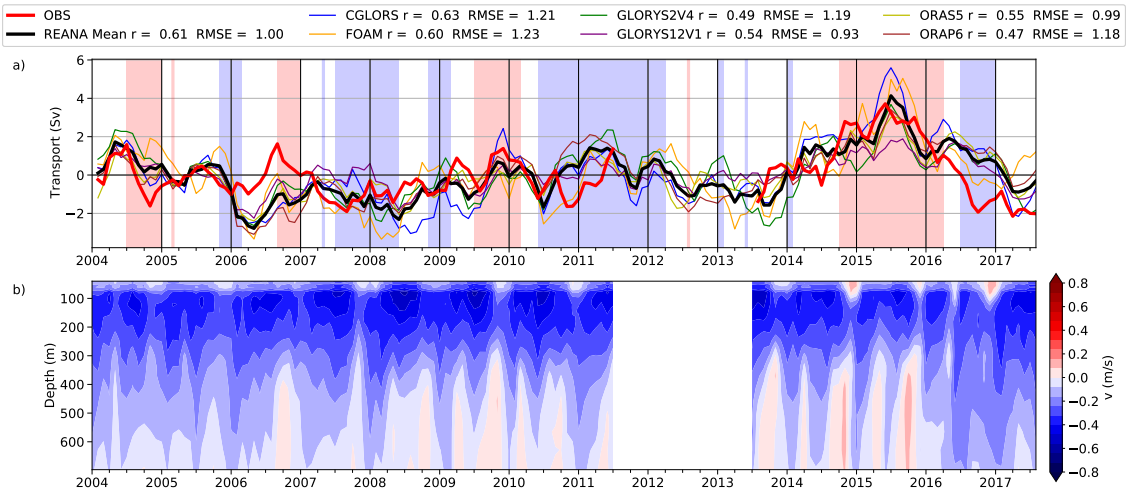

Figure 18: a) Time series of full-depth integrated transport anomalies between 2004 and 2017 as represented by observations and Reanalysis products. Red and blue shading, respectively, indicate El Niño and La Niña periods as defined by the NINO3.4 index. Legend denotes Pearson correlation coefficients r and RMSE. b) Vertical distribution of ASV (m/s) as represented by observations between 2004 and 2017. Negative values indicate southward-directed transport (towards the Indian Ocean). Note the data gap in observations between August 2011 and August 2013.

Fig. 18a shows the anomaly time series for the combined INSTANT (2004-2006) and MITF (2006-2011 and 2013-2017) periods. The corresponding Hovmoeller diagram illustrates the vertical spatial distribution of ASV. Note that the Hovmoeller diagram does not display anomalies.

Naturally, the correlations between observations and Reanalysis products decrease when considering anomalies. Guided by the mean seasonal cycle in Fig. 16a, we expect peaks (troughs) to occur in boreal winter (summer). The southward-directed flow is most intense during boreal summer and subsurface (Fig. 18b).

Considering both correlation coefficient (0.45) and RMSE (1.56 Sv), GLORYS12V1 yields the overall best match. The magnitude and direction of transport partly deviate strongly between observations and individual products. During the INSTANT period, in the second half of 2004, observations display negative anomalies decreasing to -1.6 Sv, while the Reanalysis mean features positive anomalies around 0.4 Sv. GLORYS12V1 follows the course of negative anomalies, although on a much smaller scale.

Throughout 2006 Reanalyses display merely southward-directed transport anomalies with peak transport in April (-2.8 Sv), while observed anomalies turn northward in July and minimal in September (1.6 Sv). Nevertheless, the Reanalysis mean captures the tendency toward weaker and northward transport during the monsoon transition month of September. As discussed in Figs. 14 and 15, Reanalyses struggle with the representation of minimum transport in monsoon transition months, especially the 1/4° products. Anomalies remain negative during the persistent La Niña conditions until the beginning of 2009. We find this period of constant southward transport in both, observations and the Reanalysis mean,

with generally little discrepancies. The strong southward-directed transport in CGLORS in the second half of 2008 runs against the course of the observations, pulling the mean further from the observations. GLORYS12V1 exhibits minor southward-directed transport during monsoon transition months in 2007 and again in boreal winter. While we frequently notice reversed signs between CGLORS and FOAM transport anomalies, the distinct lag in 2008 between them is uncommon. Observations and CGLORS disperse again in the first half of 2009. Discrepancies are maximal (1.5 Sv) at the beginning of the maximum transport phase (SE monsoon) in June. After observations undergo the expected trough in summer, both observations and CGLORS turn positive, with CGLORS achieving a transport minimum in November. During the strong La Niña event in 2011/2012, when transport is expected to be mostly southward-directed, all Reanalysis products display the opposite behaviour. Albeit its different course from observations, FOAM starts by displaying strong southward-directed transports anomalies. Throughout the period of missing observations, the Reanalysis mean is mostly northward directed. GLORYS12V1 displays extremely weak anomalies during this time.
Observations expectedly turn northward in October 2013, while we find a delayed increase in the Reanalysis mean, most likely caused by GLORYS2V4. Once again, Reanalysis products, excluding ORAP6 and GLORYS12V1, display stronger northward-directed transport while observed anomalies turn southward. The beginning of 2014 marks the date of strictly positive anomalies considering the Reanalysis mean. Observations feature southward-directed transport anomalies during boreal summer before the onset of the strong El Niño event in 2015/2016 turns transport anomalies northward. Such a distinct and long-lasting ENSO signal seems to be reproducible by all products. As before, GLORYS12V1 remains in a range of low transport anomalies but is still positive. Peak northward-directed anomalies are led by CGLORS (5.6 Sv in July), which also applies to the El Niño event in 2009/2010. The one-month time lag between observations (3.7 Sv in June) and Reanalyses is also clearly represented. With the end of the El Niño event, observed transport anomalies steadily turn southward and remain negative during the following La Niña phase. Apart from FOAM, Reanalysis anomalies do not turn southward before January 2017.

5.2. Dependence on large-scale sea level gradients

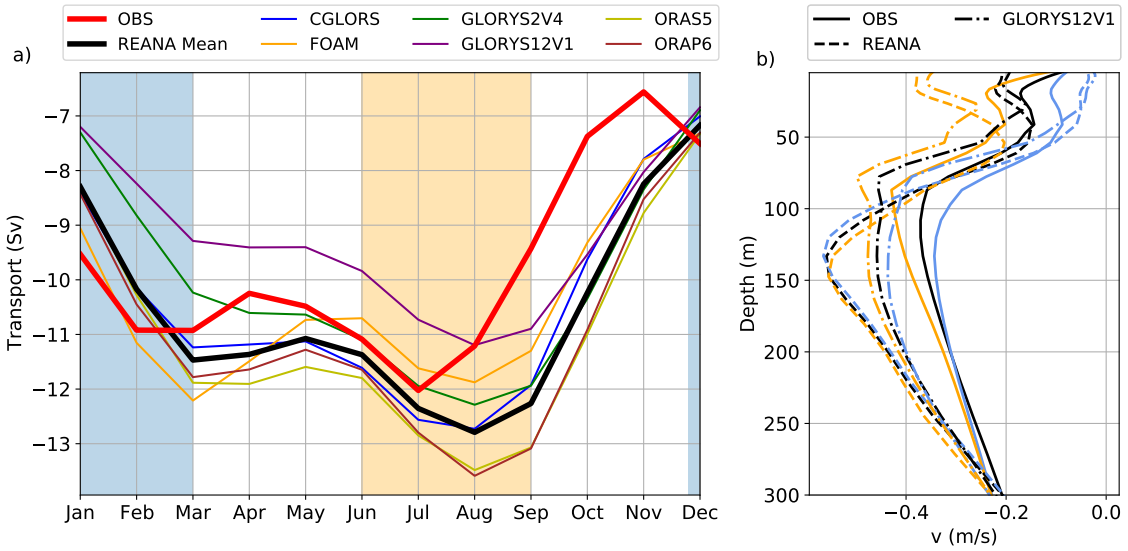

Figure 19: a) Mean seasonal cycle of ITF transport in Makassar Strait as represented by observations and Reanalysis products between 2004 and 2017. Monthly time series are filtered with a 3-month moving average. Blue and orange shading, respectively, indicate northwest monsoon months (December–March) and southeast monsoon months (June–September). b) Mean vertical profiles (black) of ASV as represented by observations (continuous lines), Reanalysis mean (dashed lines), and GLORYS12V1 (dash-dot lines). Blue and orange lines, respectively, denote average profiles over northwest monsoon months and southeast monsoon months. Negative values indicate southward-directed transport (toward the Indian Ocean). Note that only the first 300 m (upper layer) are shown.

The following chapter deals with the second major research question: How strongly does the Indonesian Throughflow transport depend on large-scale sea level gradients? Herefore, we consider the mean seasonal cycle as represented by the extended Makassar measuring period (Fig. 19a). We find that there is a strong seasonal dependence between ITF transports through Makassar Strait and the Australian-Indonesian monsoon, thus, the employment of long-term measurements is appropriate. Furthermore, we consider the mean sea level and the wind regime during the two different monsoon phases in Fig. 2a and b. At this point, the encircled areas in the western Pacific and the eastern Indian Ocean are of interest.
As with Fig. 16a, we find maximum ITF transport in boreal summer during the SE monsoon and minimum transport during boreal winter when the NW monsoon prevails. Absolute minimum transports in the monsoon transition months (April/May and October/November) represent the intrusion of Indian Ocean Kelvin waves into Makassar, which act to reduce ITF transport.
However, the wind regime during the NW monsoon (Fig. 2a) does not necessarily indicate that transport is at a minimum in boreal winter. If anything, it seems like the wind favors a northward-directed transport through Makassar Strait. Similarly, the southeastern wind regime during the SE monsoon does not seem to favor maximum transport in boreal summer. The reason for this counterintuitive behaviour, lies in the fact that the Makassar Strait vertical profile is not a surface intensified profile but a thermocline intensified profile. We have already established this with regard to Figs. 12. Mean velocity maxima are found in ∼100 m, indicating that the flow is more or less independent of wind stress at the surface. Subsequently, there is another mechanism responsible for the regulation of ITF transport. Fig. 2a demonstrates that the mean sea level decreases in the ITF's entrance region during

the NW monsoon and increases off of the coast of Java, the exit region. A northward-directed sea level gradient establishes, decelerating the ITF in Makassar Strait or even reversing it. The opposite holds during the SE monsoon: mean sea level increases in the entrance region while decreasing south of Java. As a result, a southward-directed sea level gradient arises, yielding maximum transport in boreal summer. We aim to confirm this behaviour with monsoon-dependent vertical profiles, as shown in Fig. 19b. We find that transports are generally stronger during the SE monsoon (yellow shading and lines) while also exhibiting more pronounced near-surface maxima. Near-surface maxima are not shown in Figs. 12 and have not been addressed so far. Observations and the Reanalysis mean display near-surface maxima in ∼20 m with -0.25 m/s and -0.38 m/s, respectively. The overestimation of magnitude with respect to Reanalyses has been addressed. GLORYS12V1 features a near-surface maximum (-0.36 m/s), as well, however, closer to the surface in already ∼10 m. The situation reverses in greater depths, where the depth of maximum velocities (∼80 m) in observations (-0.43 m/s) and GLORYS12V1 (-0.52 m/s) coincide, while the Reanalysis mean maximum occurs in ∼150 m (-0.56 m/s). Maxima of the black mean vertical profiles are in accordance with the depths in Figs. 12.
Focusing on the NW monsoon (blue shading and lines), ASV profiles mostly weaken, near-surface maxima almost vanish, and velocity maxima deepen. This is in accordance with a general decrease in transport during the NW monsoon. Observations still indicate a weak near-surface maximum (-0.11 m/s) in ∼20 m, whereas the Reanalysis mean does not exceed values of -0.05 m/s. Once again, the behaviour reverses, considering the thermocline maxima. Observations and GLORYS12V1 feature maxima in ∼120 m (-0.34 m/s) and ∼150 m (-0.44 m/s), respectively, whereas the Reanalysis mean displays an equally strong NW monsoon-maximum (-0.57 m/s) in shallower depths of ∼130 m. The vertical shift in thermocline maxima between observations and the Reanalysis mean is something we have found in the short mooring data sets as well (Figs. 12).

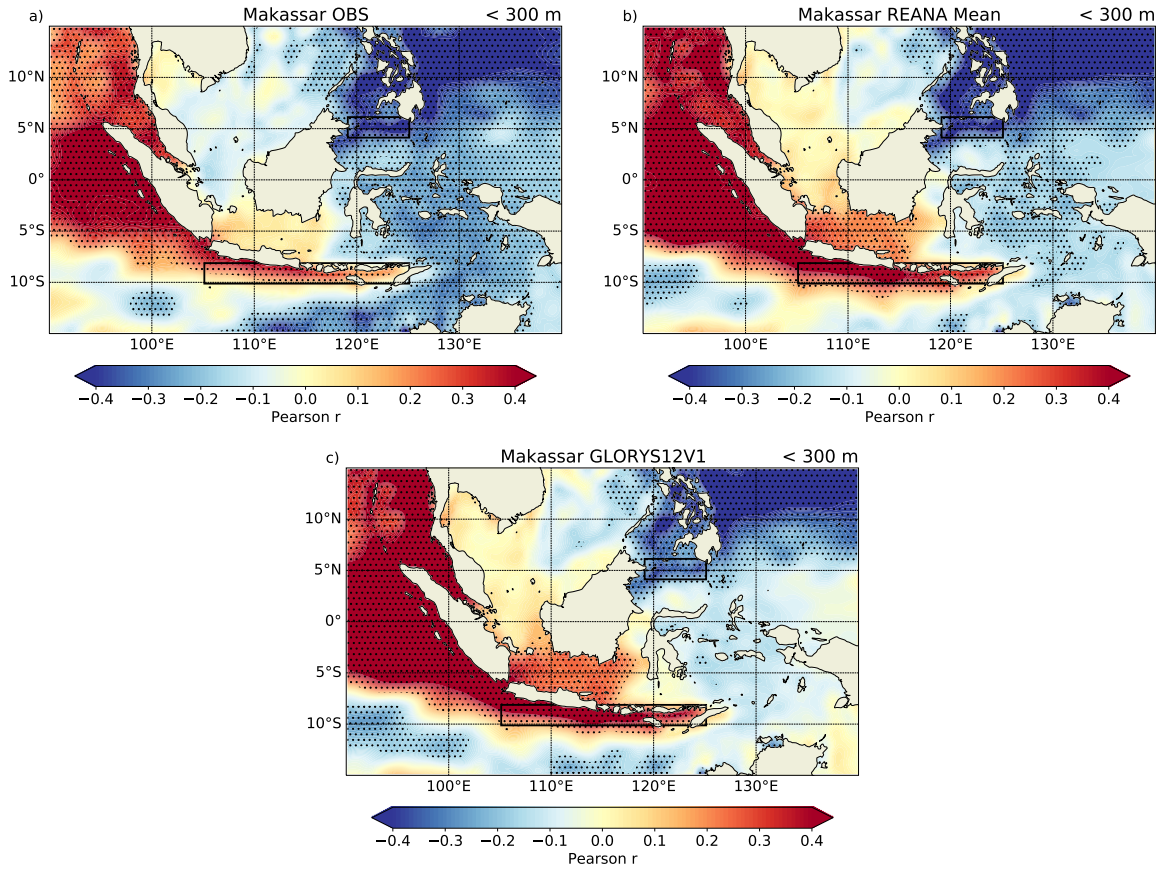

Figure 20: Correlation maps (90°E - 140°E; 15°N - 15°S) expressing correlation between integrated transport anomalies (0-300 m) through Makassar Strait and mean sea level anomalies as represented by a) observations, b) the Reanalysis mean, and c) GLORYS12V1. Anomalies cover the period from 2004 to 2017 at zero lag. Blueish (redish) values denote negative (positive) correlations. Encircled areas correspond to entrance (119°E - 125°; 4°S - 6°S) and exit (105°E - 125°E; 8°S - 10°S) regions. Stippling indicates significant correlation coefficients above the 95% confidence level.

To further underline the fact that the seasonal cycle of ITF transport relates to the sea level gradient between the western Pacific and the eastern Indian Ocean, we analyse correlation maps (Figs. 20) between volume transport anomalies in Makassar and sea level anomalies. Note that Makassar transport does not account for the total ITF transport, however, measurements from Makassar Strait provide the longest data series to compute possible correlations.

Through rigorous testing, we find that correlations are most pronounced when considering the upper 300 m of ITF transport through Makassar. The water column partition is consistent with that applied by Pujiana et al. (2019) and helps simplify the analysis. For this reason, we will first focus on the layer between the surface and 300 m, which is referred to as the upper layer. Based on the correlation patterns, we are able to modify the predetermined entrance and exit regions (Figs. 2a and b) towards regions displaying higher correlations. The exit region was only slightly adjusted, covering a more narrow band, while the entrance region decreased in size and moved eastwards. Generally, correlation patterns in Figs. 20 show similar areas of maximum positive and negative correlation, respectively, off of the coast of Sumatra and Java and in the western Pacific. The convention is such that positive (negative) anomalies correspond to higher sea levels in the entrance region (exit region). A positive (negative) correlation implies southward-directed ITF transport if mean

sea level anomalies are negative (positive) and northward-directed transport if anomalies are positive (negative). If we combine this statement with Figs. 20, we find that negative correlations within the entrance region indicate southward-directed (northward-directed) transport if mean sea level anomalies are positive (negative). This is consistent with our description of the large-scale sea level gradient in Fig. 19a.
In the case of observations (Fig. 20a) and the Reanalysis mean (Fig. 20b) negative correlation coefficients reach -0.44 within the entrance region. Considering GLORYS12V1, correlation is less pronounced in the Sulawesi Sea with maximum negative coefficients of -0.37. Contrariwise GLORYS12V1 displays high positive correlations of 0.57 within the exit region, and observations and the Reanalysis mean, 0.39 and 0.48, respectively. It should be noted that while Reanalyses generate temporally consistent data sets, observations lack data between August 2011 and August 2013.
Note also the different correlation patterns in the outflow straits of Lombok, Ombai, and Timor. While significant positive correlations dominate Lombok and Ombai Strait, correlation coefficients turn negative in Timor Passage and are even significant in Fig. 20a. We also show correlation maps correlating transport anomalies (0-300 m) through Ombai (Fig. 44a) and Timor (Fig. 45a) to sea level anomalies, delivering redundant information compared with Figs. 20. Since the outflow passages were only monitored during the INSTANT program, we employ Reanalysis products for this purpose.
Furthermore, we find that ITF transport through Makassar is highly correlated with sea level anomalies over the equatorial Indian Ocean ($r_{RMEAN} \sim 0.6$), where the Wyrtki Jet is generated and subsequently equatorial Kelvin waves that propagate towards the eastern coast and modify the sea level. With regard to Figs. 14 and 15 the effect of Kelvin waves on the ITF has been established. In the western Pacific, maximal negative correlations ($r_{RMEAN} \sim 0.5$) coincide with the westward approaching NEC, which varies with ENSO. Moreover, White et al. (2003) have associated this area with equatorial Rossby waves that influence the ITF from the west by modifying the pressure head. Indonesian Seas show rather weak correlations with Makassar transport, in which we find positive correlations in the Java Sea and moderate but significant negative correlations in the Banda Sea, the Arafura Sea, and the Timor Sea. Correlations in the Java Sea are also significant in Figs. 20b and c. Reanalysis mean and GLORYS12V1 display both positive and negative correlations within the South China Sea, while observations show primarily negative correlations.
Overall correlations remain moderate, even if only the upper layer is considered. Nonetheless, we use the adjusted encircled regions for the computation of sea level difference anomalies in order to understand how the throughflow is affected by both oceans. Therefore, sea level differences refer to the differences between the encircled entrance and exit regions in Figs. 20.

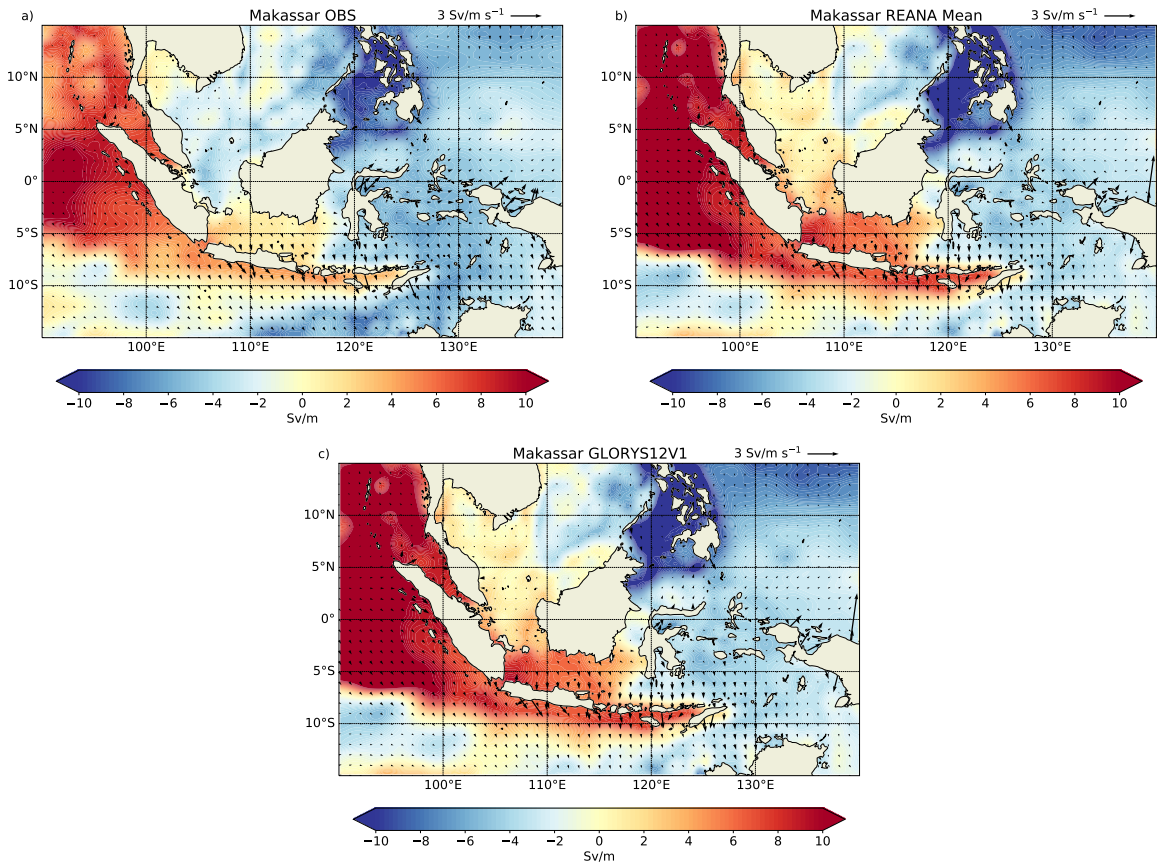

Figure 21: Regression maps (90°E - 140°E; 15°N - 15°S) expressing the dependence of monthly integrated transport anomalies (0-300 m) through Makassar Strait on mean sea level anomalies as represented by (a observations, (b the Reanalysis mean, and (c GLORYS12V1 at zero lag. Anomalies cover the period from 2004 to 2017. Blueish (redish) values denote negative (positive) regression coefficients (Sv/m). Black arrows display the regression of monthly integrated transport anomalies (0-300 m) on 10 m surface wind anomalies. Their length and orientation denote, respectively, speed and direction.

In addition to Figs. 20, we compute the regression of integrated transport anomalies in the upper layer (<300 m) through Makassar Strait onto satellite-retrieved sea level anomalies at every grid point in Figs. 21. Aside from that, the corresponding regressed field of wind anomalies is shown. We find similar color patterns between Figs. 20 and 21. Negative regression coefficients around the ITF's entrance region indicate a decrease in transport with decreasing SLA. This is highly plausible because a decrease in SLA in the entrance region implies the onset of a northward-directed pressure gradient, acting to reduce ITF transport. The exit region, off of the coast of Java and the Nusa Tenggara island chain, registers positive regression coefficients, denoting an increase in northward-directed transport with rising sea level anomalies. Higher sea level anomalies within the exit region slope the mean sea level towards the western Pacific, implying stronger northward transports. The regression maps also show the inversed relation between Ombai Strait and Timor Passage. Information from the regressed wind regime is most pronounced between 5°S and 10°S across the entrance region and points southward. Otherwise, wind arrows remain mostly inconspicuous, underlining the fact that the integrated transport through Makassar is not strongly influenced by surface wind stress. The differences in data sets are similar to the ones in Figs. 20, that is, coefficients are higher with respect to Reanalysis products. Nevertheless, a qualitative agreement in the spatial distribution of coefficients between all

data sets emerges.
Considering full-depth integrated transports, regression coefficients turn negative within the exit region in Fig. 21a and generally decrease by an order of magnitude. In the case of the Reanalysis mean, regression coefficients off of the coast of Java and Nusa Tenggara only slightly decrease, providing almost redundant information. The same applies to GLORYS12V1, except coefficients within the entrance region decrease as well.

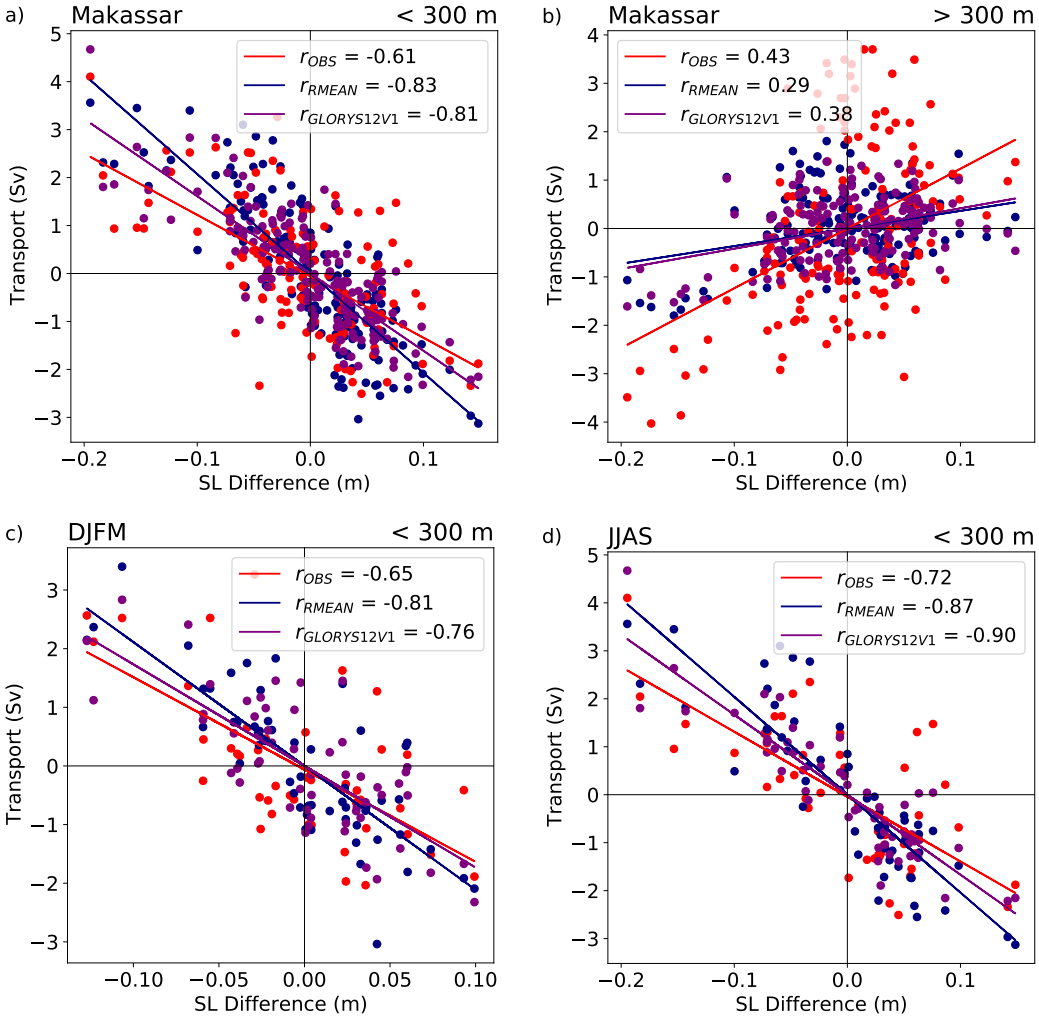

Figure 22: Scatter plots relating (a, (c, (d upper layer (0-300 m) and b) lower layer (300-700 m) integrated transport anomalies through Makassar Strait to sea level difference anomalies as represented by observations, Reanalysis mean, and GLORYS12V1 between 2004-2017 at zero lag. Scatter plots represent (a, (b all months and specifically (c northwest monsoon and (d southeast monsoon months. Legends denote Pearson correlations coefficients r.

Figs. 22 present scatter plots of monthly averages of Makassar transport anomalies versus monthly mean sea level difference anomalies between the western Pacific and the Indian Ocean. Again, we focus on the comparison between observations, Reanalysis mean, and GLORYS12V1 in the upper layer (<300 m) and lower layer (>300 m) separately. Positive transport anomalies indicate northward-directed flow, while negative transport anomalies refer to southward-directed flow. Regarding sea level differences, positive values imply higher sea level anomalies in the Pacific, while negative values can be attributed to higher

Indian Ocean sea level anomalies. Sea level differences are negative between November and May and turn positive in June until October. The seasonal cycle of sea level differences is consistent with the seasonal cycle of transport, discussed in Figs. 16.
Correlations between transport anomalies in the upper layer and sea level differences (Fig. 22a) are negative, with the Reanalysis mean exhibiting the strongest correlations of r_{RMEAN} = -0.83. Observations, featuring many outliers, and GLORYS12V1 reveal correlations of r_{OBS} = -0.61 and $r_{GLORYS12V1}$ = -0.81, respectively. Figs. 20 already suggested the presence of weaker correlations regarding observed transports, especially within the exit region.
We find that negative transport anomalies correspond to positive sea level differences, indicating southward-directed transport if mean sea level anomalies are higher in the Pacific. Furthermore, plotted slopes highlight the connection between positive (e.g., northward-directed) transport anomalies and negative sea level differences, which refer to higher mean sea level anomalies in the Indian Ocean.
To assess relations during the northwest (DJFM) and southeast monsoon (JJAS), we group transport and sea level difference anomalies and assign them accordingly. Since ITF transport in Makassar is at a maximum in boreal summer, significant correlations are governed by the anomalies during JJAS (Fig. 22d). In addition, positive transport anomalies are as high as 5 Sv, and negative sea level differences reach -0.2 m as opposed to the DJFM period. Correlations regarding observations and GLORYS12V1 increase by about 10% (r_{OBS} = -0.72 and $r_{GLORYS12V1}$ = -0.90), whereas the Reanalysis mean attains r_{RMEAN} = -0.87. As suggested by Pujiana et al. (2019) lower correlations during boreal winter likely echo the impact of interannual variations in the South China Sea and subsequently the Java Sea on the large-scale sea level gradient (Fig. 22c). We register the strongest decline in GLORYS12V1 ($r_{GLORYS12V1}$ = -0.76), while observations and the Reanalysis mean score values of r_{OBS} = -0.65 and r_{RMEAN} = -0.81.
Correlations in the lower layer (>300 m, Fig. 22b), covering all months, are weakly positive and correspond to r_{OBS} = 0.43, r_{RMEAN} = 0.29, and $r_{GLORYS12V1}$ = 0.38. In consideration of full-depth transports (0-700 m) negative correlations decrease towards r_{RMEAN} = -0.62 and $r_{GLORYS12V1}$ = -0.60 with a major decrease in observations, r_{OBS} = -0.06. The strong degression suggests that transport anomalies in the lower layer (<300 m) are generally opposite to the upper layer (>300 m), canceling each other out. In order to verify this assumption, we consider the anomaly time series of upper-layer transport and lower-layer transport separately.

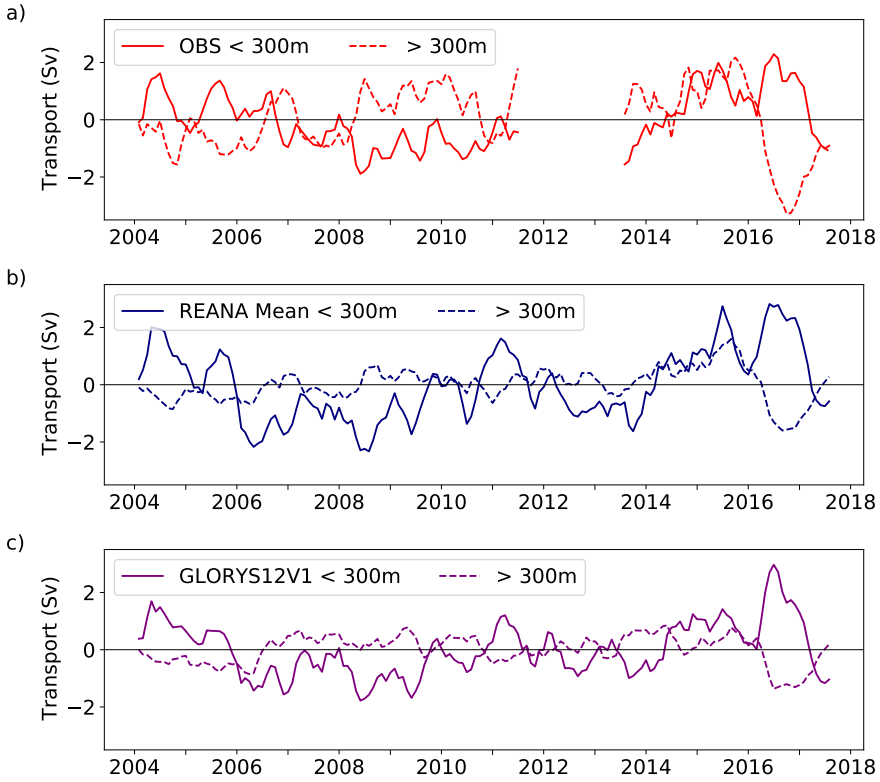

Figure 23: Monthly time series of integrated transport anomalies through Makassar Strait in the upper layer (continuous lines) and lower layer (dashed lines) as represented by a) observations $r_{maxlag=-1} = -0.37$, b) Reanalysis mean $r_{maxlag=-1} = -0.30$, and c) GLORYS12V1 $r_{maxlag=-1} = -0.45$ between 2004-2017.

The 2004-2017 time series of integrated transport anomalies for the upper (<300 m) and lower layer (>300-700 m) are shown in Figs. 23. They imply that transport anomalies in the lower layer are generally opposite to the upper layer, displaying a distinct signal in 2016/2017. Within the scope of Figs. 14 and 15 we discussed the intrusion of Kelvin waves into Makassar Strait, which typically influences the ITF in the lower layer. Peaks of positive transport in the lower layer during monsoon transition months represent their appearance. By comparing Fig. 18a with Figs. 23 we find similar courses between full-depth integrated transport anomalies and upper layer anomalies ($r_{OBS} = 0.5$), indicating that most of the transport occurs within the upper 300 m. The Reanalysis mean ($r_{RMEAN} = 0.9$) and GLORYS12V1 ($r_{GLORYS12V1} = 0.8$) reproduce this instance.
Observations display almost equally strong upper layer and lower layer transport with peak transport anomalies of -3.3 Sv in the lower layer in October 2016. The Reanalysis mean and GLORYS12V1, on the other hand, exhibit comparatively weak transport in the lower layer reaching values between [-1.6;1.6] Sv and [-1.4;0.9] Sv, respectively. This coincides with earlier findings of Reanalysis products not being able to resolve as highly in greater depths. Thus, we find weaker transport in lower layers compared to the observations. Another comparison with Fig. 18a connects the period of positive transport anomalies in both, upper and lower layers, to the strong El Niño event of 2015/2016. However, upper and lower transports remain opposite to each other. This period of positive transport anomalies is also apparent in the Reanalysis mean and, albeit somewhat weaker, in GLORYS12V1.
In 2016/2017, although we find a series of negative transport anomalies in the lower layer or, in other words, an increase in ITF transport, the full-depth integrated transport is

remarkably reduced (Fig. 17, (Pujiana et al., 2019)). Negative transport anomalies in the lower layer are less intense in the Reanalysis mean and GLORYS12V1. The overall reduction of total ITF transport underlines the fact that the upper 300 m supply about 73% of the total transport in Makassar Strait (Gordon et al., 2019).

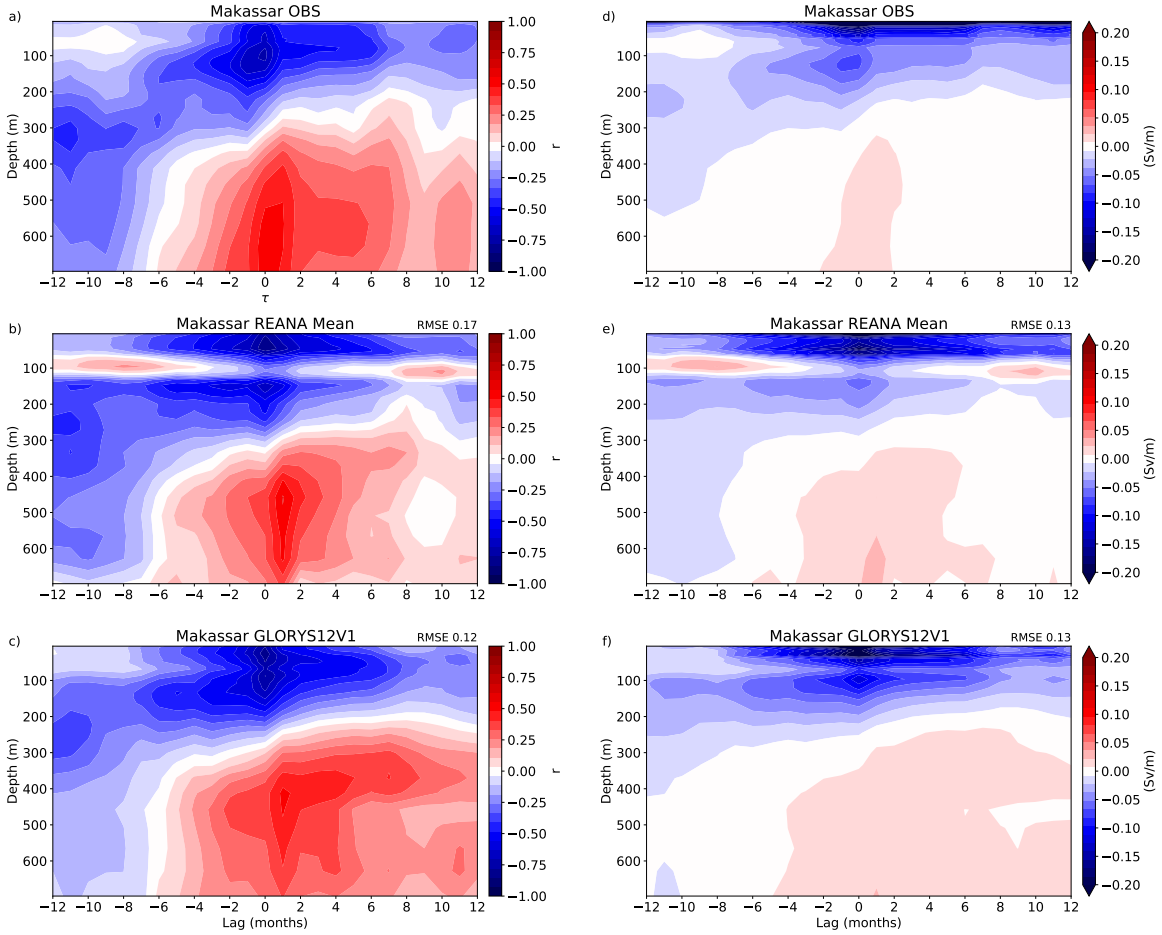

Figure 24: Left panel: Correlation between Makassar transport anomalies V(z) and sea level gradient anomalies $\nabla\eta$ (Pacific - Indian Ocean) dependent on both depth and time lags, as represented by a) observations, b) Reanalysis mean, and c) GLORYS12V1. Right panel: Regression of Makassar transport anomalies on sea level gradient anomalies (Sv/m) as represented by d) observations, e) Reanalysis mean, and f) GLORYS12V1. Considered time series cover the period between 2004 and 2017. Red (blue) values indicate positive (negative) correlations (left) and regression coefficients (right).

After this short excursion that focused on the behaviour of upper and lower layer transport anomalies in Makassar Strait, we circle back to the relation between full-depth integrated transports and the SLA gradient. Rather than examining the overall correlation between full-depth integrated transport anomalies and sea level difference anomalies (Figs. 22), we assess the correlation between said anomalies as a function of depth at different lags (Figs. 24a-c). Note again that sea level difference anomalies refer to the difference between sea level anomalies in the entrance region (Pacific) and exit region (Indian Ocean) of the ITF. The patterns produced by the observations (Fig. 24a) and GLORYS12V1 (Fig. 24c) exhibit strong similarities (RMSE = 0.12), while the Reanalysis mean (Fig. 24b) pattern deviates above ∼150 m (RMSE = 0.17). The higher RMSE in the Reanalysis mean (Fig.

24b,e) is most likely a result of positive correlations (regression coefficients) occurring around 100 m at higher lags. Nonetheless, the fact that negative correlations dominate the upper 300 m and negative lags between -7 and -12 months applies to all cases. Moreover, positive correlations prevail in lower layers, more so towards positive lags. Evidently, the aforementioned different behaviour in the upper and lower layer is also visible here. Focusing on the regression coefficients in Figs. 24d-f, we find qualitative agreement with Figs. 24a-c and validation in that sea level gradient anomalies are able to explain the direction of ITF transports.

Regarding the observations (Fig. 24a), we find maximum positive and negative correlations of $r_{OBS,+}$ = 0.54 and $r_{OBS,-}$ = -0.72 at lag = 0 in ∼630 m and ∼100 m, respectively. The Reanalysis mean reaches maximum negative correlations of $r_{RMEAN,-}$ = -0.85 already in ∼50 m at lag = 0, but $r_{RMEAN,+}$ = 0.56 at lag = 1 in ∼460 m. GLORYS12V1 exhibits peak negative correlations of $r_{GLORYS12V1,-}$ = -0.83 at lag = 0 in ∼25 m. Maximum positive correlations of $r_{GLORYS12V1,+}$ = 0.50 appear at lag = 1 in ∼410 m. The fact that maximum negative correlations occur consistently at lag = 0 supports our decision of choosing lag = 0 in Figs. 22. Upper layer negative correlations are noticeably stronger and indicate, again, southward (northward) directed transport if mean sea level anomalies are higher in the Pacific (Indian Ocean), e.g., positive (negative). Noteworthy positive correlations start to appear below 300 m, suggesting that sea level gradient-driven transports are an upper layer phenomenon.
Upper layer negative regression coefficients of up to $s_{OBS,-}$ = -0.46 Sv/m at lag = 0 indicate a decrease in southward-directed transport with decreasing SLA. Given the fact that the ITF's basic orientation runs southward, negative coefficients must correspond to the entrance region, i.e., the western Pacific. The Reanalysis mean and GLORYS12V1, respectively, reach maximum negative coefficients of $s_{RMEAN,-}$ = -0.34 Sv/m and $s_{GLORYS12V1,-}$ = -0.36 Sv/m, also at lag = 0. Similar to the correlation pattern, positive regression coefficients dominate the lower layer (<300 m) with maximum values of ∼0.02 Sv/m in all data sets that occur very close to the bottom layer in Figs. 24d-f. The lower layer response thus reverses, suggesting an increase in northward-directed transport with increasing SLA, which by definition of the ITF's orientation, corresponds to the behaviour of the exit region.

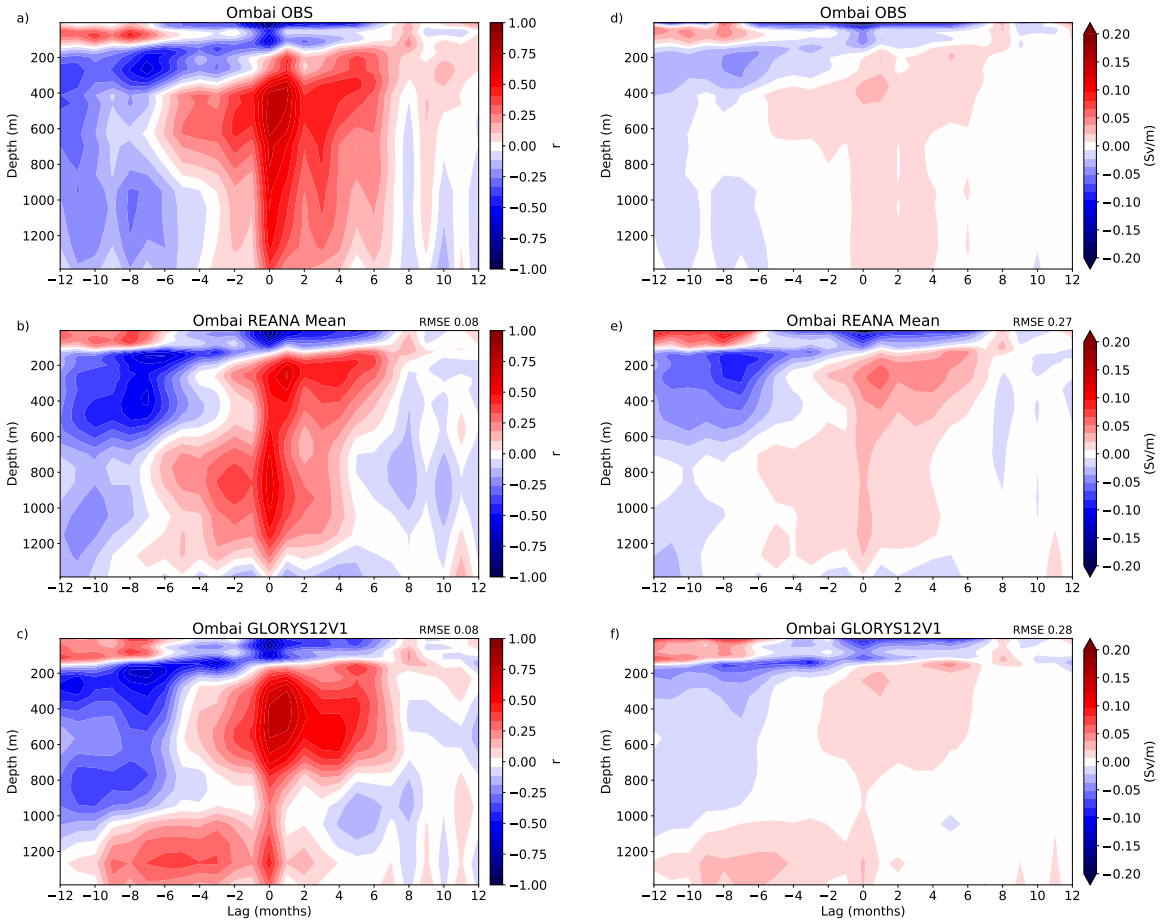

Figure 25: Left panel: Correlation between Ombai transport anomalies V(z) and sea level gradient anomalies $\nabla\eta$ (Pacific - Indian Ocean) dependent on both depth and time lags, as represented by a) observations, b) Reanalysis mean, and c) GLORYS12V1. Right panel: Regression of Ombai transport anomalies on sea level gradient anomalies (Sv/m) as represented by d) observations, e) Reanalysis mean, and f) GLORYS12V1. Considered time series cover the period between 2004 and 2006. Red (blue) values indicate positive (negative) correlations (left) and regression coefficients (right). Note the change in depth scale compared to Makassar Strait.

Seeing that part of the Makassar transport ends up traversing Ombai Strait and Timor Passage, we assume to find similar patterns of correlation and regression coefficients. Such an investigation only applies to deep enough straits, which is why we disregard Lombok Strait. Figs. 44a and b and 45a and b already highlighted the fact that the response to the large-scale sea level gradient reverses in the lower layer. Accordingly the two-layer system does not only apply to ITF inflow passages but also to the deeper outflow passages, Ombai and Timor. Figs. 25 and 26 confirm the assumption of a qualitatively similar current response in Ombai Strait and Timor Passage, respectively. RMSE of 0.08 (Figs. 25b and c) indicate an equally good match between Reanalysis products and observations in Ombai Strait. The same holds true for Figs. 25e and f. In Timor Strait, the advantages of GLORYS12V1 (0.10 below 0.13) are most likely at play.
Considering Ombai Strait, negative values dominate the upper 200 m around lag = 0 and lags between -6 to -12, particularly in the observations. Peak negative values of $r_{OBS,-}$ = -0.85, $r_{RMEAN,-}$ = -0.83 and $r_{GLORYS12V1,-}$ = -0.78 all occur within the first 40 m at lag = 0. Weaker negative coefficients appear on the positive lag axis as well. In between,

below ∼200 m, positive values of up to $r_{OBS,+} = 0.75$ (∼510 m), $r_{RMEAN,+} = 0.64$ (∼245 m), and $r_{GLORYS12V1,+} = 0.76$ (∼410 m) prevail. Peak positive values occur at different depths depending on the considered data set, and as with Makassar Strait, $r_{RMEAN,+}$, and $r_{GLORYS12V1,+}$ correspond to lag = 1 and $r_{OBS,+}$ to lag = 0. Furthermore, correlation coefficients exceed those in Makassar Strait and are led by the observations. Higher positive correlation coefficients below ∼200 m suggest a stronger but still reversed response in lower layers. This, in turn, indicates that the direction of transport in greater depths cannot be explained by sea level gradients.
With respect to Figs. 14 and Figs. 15 we have established a surface-confined ITF core within Ombai Strait and Timor Passage. Compared to Makassar Strait, a more vertically restricted area of negative values above ∼200 m possibly reflects this core. The regression maps (Figs. 25d-e) also show the depth-dependent sign convention in regression coefficients and, thus, the impact of potentially two different mechanisms.

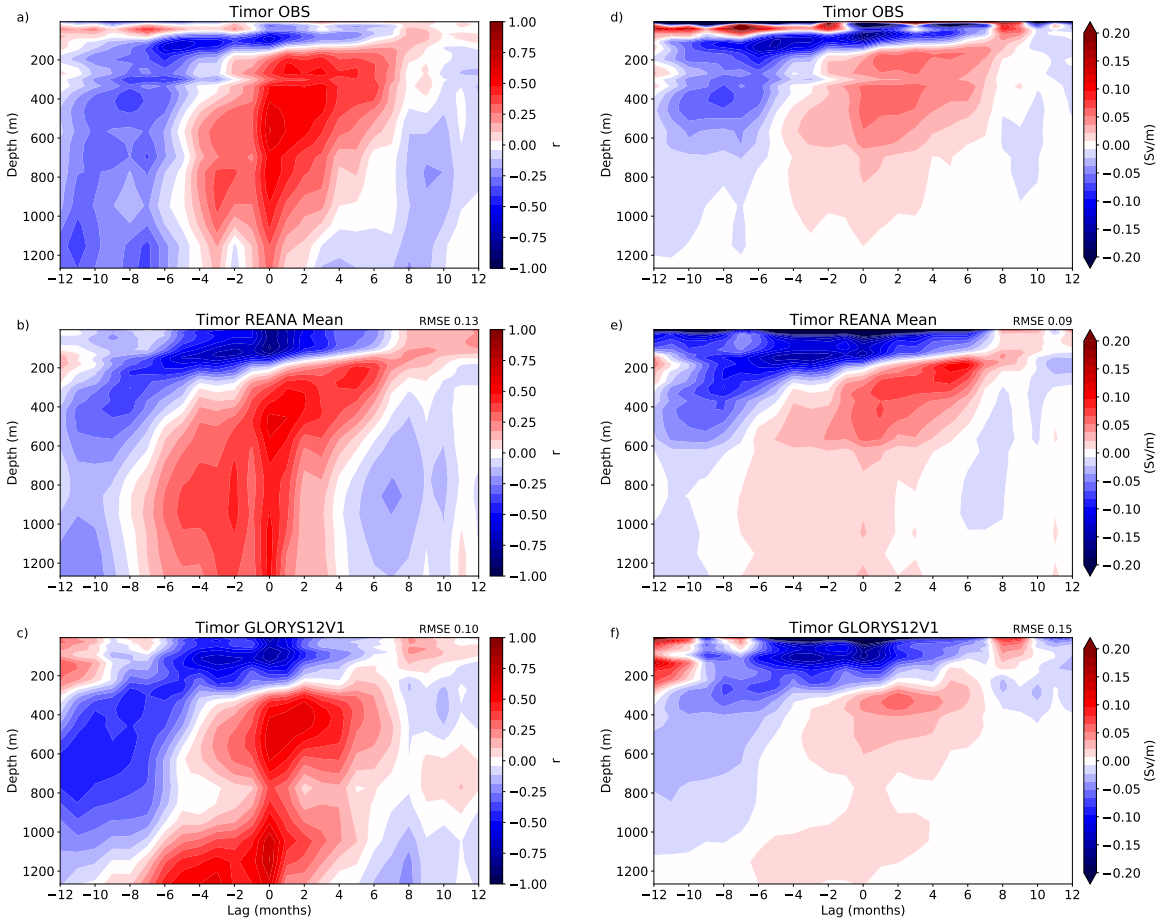

Figure 26: Left panel: Correlation between Timor transport anomalies V(z) and sea level gradient anomalies $\nabla\eta$ (Pacific - Indian Ocean) dependent on both depth and time lags, as represented by a) observations, b) Reanalysis mean, and c) GLORYS12V1. Right panel: Regression of Timor transport anomalies on sea level gradient anomalies (Sv/m) as represented by d) observations, e) Reanalysis mean, and f) GLORYS12V1. Considered time series cover the period between 2004 and 2006. Red (blue) values indicate positive (negative) correlations (left) and regression coefficients (right). Note again the change in depth scale.

Timor Passage (Figs. 26) produces similar results to Ombai Strait. Differences occur with respect to the magnitude of coefficients and maximum lags. Again, the upper layer corresponds to negative correlation coefficients that link southward (northward) directed transport anomalies to higher sea level anomalies in the western Pacific (eastern Indian Ocean). At lag = 0, $r_{RMEAN,-}$ and $r_{GLORYS12V1,-}$ reach maximum negative values of -0.86 (100 m) and -0.78 (80 m), respectively. Observations reach peak negative values of up to $r_{OBS,-}$ = -0.62 (120 m) at lag = -5, suggesting a lagged response of Timor transport to variabilities in the sea level gradient (lagging 5 months). There are also signs of secondary minima around lag = -8 in Ombai Strait between ∼200 to 400 m. Besides, Fig. 20b, as well as Figs. 44a and 45a indicate significant positive correlations in Ombai Strait compared to Timor Passage, where correlations seem to turn negative. This, in turn, suggests that the eastern Indian Ocean can positively influence the ITF transport in the upper layer in Ombai Strait, whereas the western Pacific negatively influences the upper layer transport in Timor Passage. We arrive at similar conclusions with regression maps between upper layer transport in Makassar and SLA (Figs. 21a-c).
Depending on the data set, we find different depths in which correlation coefficients turn positive. Maximum positive correlations are generally weaker compared to Ombai Strait with $r_{OBS,+}$ = 0.64 (570 m), $r_{RMEAN,+}$ = 0.58 (510 m) and $r_{GLORYS12V1,+}$ = 0.71 (1150 m), all corresponding to lag = 0. The maximum correlation of $r_{GLORYS12V1,+}$ in 1150 m is most likely a result of GLORYS12V1's ability to resolve to a depth of 1800 m, whereas 1/4° Reanalyses are limited to 1270 m. Magnitudes of negative regression coefficients (Figs. 26d-e) are more than twice the size of positive coefficients, indicating a decrease in the current response in lower levels.

Subchapter 2.1 dealt with the issue of barotropic flow near the surface and in greater depths. We demonstrated that the flow response would be the same everywhere only in the barotropic case, i.e., when the horizontal pressure gradient does not change with depth. One would assume that the flow response decreases with depth because current velocities decrease with depth. However, if the flow response reverses, as we find to be the case in Figs. 24, 25, and 26 one could attribute this to baroclinic effects that reverse the pressure gradient at greater depths. For this reason, we try to estimate the potential baroclinic effect on the pressure gradient at depth by integrating the water density vertically. We implement this by determining the depth-dependent pressure gradient between the western equatorial Pacific and the eastern equatorial Indian Ocean and correlating it with transport anomalies in Makassar Strait. Since observations are unavailable in these regions, we base this analysis solely on Reanalysis data.
In consideration of Eq. 14 we compute the pressure in each depth as follows

$$p(z) = p(SFC) + g \int_{dz} \rho(T, S)\ \mathrm{d}z. \tag{47}$$

Sea level anomalies serve as a proxy for pressure anomalies near the surface therefore, we calculate $p(SFC)$ using SLA within the entrance and exit region. Density is calculated using temperature and salinity data in the considered areas (UNESCO, 1981). The densities are then spatially averaged and vertically integrated. In the last step, we determine the depth-dependent pressure gradient ∇p(z) by taking the differences between $p(z)$ in the Indian Ocean and the western Pacific and correlating them with transport anomalies in each depth.

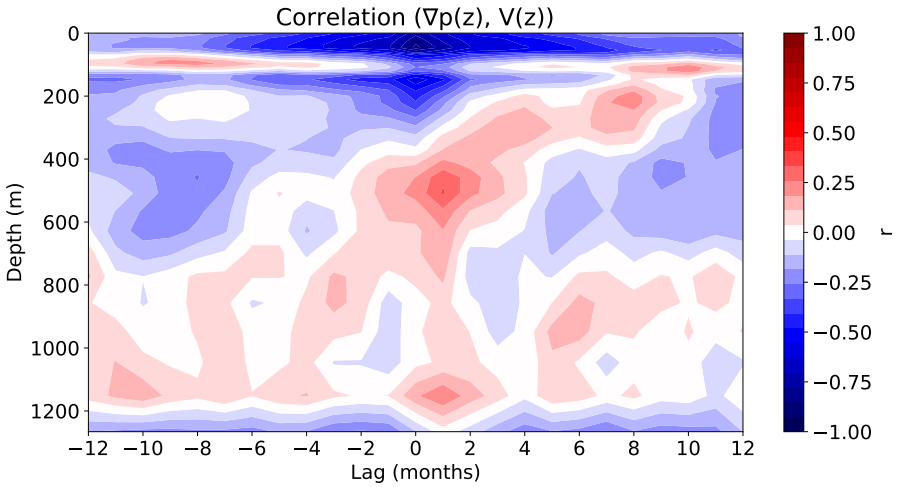

Figure 27: Correlation between depth-dependent pressure gradient anomalies ∇p(z) (Pacific - Indian Ocean) and Makassar transport anomalies V(z) dependent on both depth and time lags, as represented by the Reanalysis mean. Considered time series cover the period between 2004 and 2017. Red (blue) values indicate positive (negative) correlations. Note the change in depth scale compared to Figs. 24.

Fig. 27 displays correlations between depth-dependent pressure gradient anomalies ∇p(z) and integrated transport anomalies V(z) through Makassar Strait. Reanalyses allow us to study the response of transports on the pressure gradient in depths greater than 700 m. In Makassar Strait, velocity data are available down to ∼1250 m depth. Maximum negative correlations reach values of -0.87 in ∼50 m at lag = 0. Maximum positive correlations, on the other hand, obtain values of only 0.34, corresponding to a depth of ∼510 m at lag = 1. The overall correlation pattern remains similar to Fig. 24b.

The high negative correlation between the sea level gradient and transport anomalies in Fig. 22a suggest a strong influence of the sea level gradient on the upper layer (<300 m). We have already demonstrated several times the reversal of the current response in the lower layer. A positive correlation in the lower layer is no longer consistent with the orientation of the main southward-directed sea level gradient and implies the appearance of another mechanism. By means of Fig. 27, we find that the flow response does indeed decrease with depth and even reverses in ∼400 m. Furthermore, correlations decrease by a third and turn positive. Fig. 27 makes it apparent that the connection with SLA is solely an upper layer process, while other processes dominate in lower layers. Pujiana et al. (2019) attribute the appearance of this two-layer system to the role of baroclinic Kelvin waves that originate in the equatorial Indian Ocean and modulate the large-scale pressure head. Moreover, Li et al. (2020) investigated the two-layer system with regard to ENSO and suggest that variations in South Pacific water masses that feed the lower layer likely influence the behaviour of the ITF inflow. In addition, baroclinic Rossby waves originating in the north Pacific Ocean may impact the ITF sub-thermocline.

We seek to verify this result by reproducing the anomalies of the steric sea level component from ORAS5 (Figs. 29a and b). Following Greatbatch (1994) and hence the definition from the NEMO ocean model (Madec et al., 2008), we compute the steric sea level anomalies by vertically integrating the reanalysis-based density anomalies. Density anomalies are integrated with respect to a reference value of $\rho_0 = 1035$ kg/m^3. The resulting density anomaly gradients are depicted in Fig. 28a with a vertical variation of ∼0.1 kg/m^3 (∼100 Pa) in the upper 100 m and a vanishing gradient in greater depths. In consideration of Eq. 47, we show the corresponding pressure anomaly gradients (Fig. 28b), which are used in

the computation of Fig. 27 and demonstrate the overall weakening with depth.

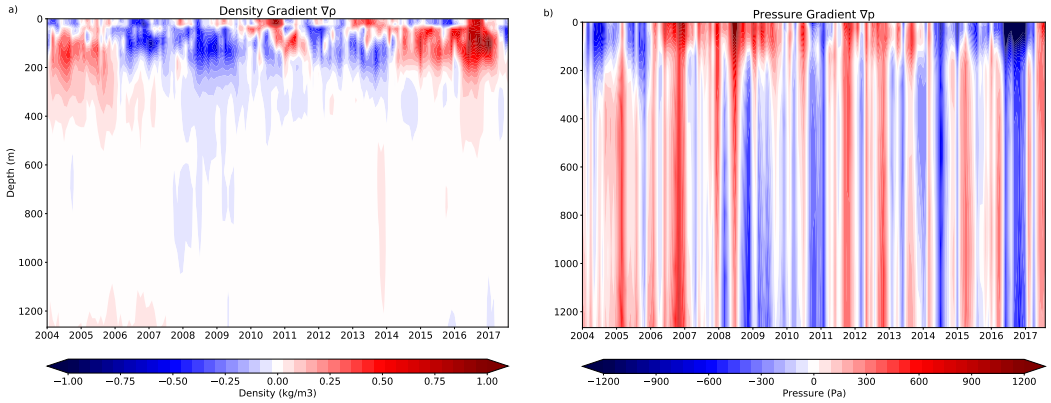

Figure 28: Vertical anomaly profiles of a) the density gradient $\nabla\rho$ and b) the pressure gradient ∇p between the western Pacific and the eastern Indian Ocean. Red (blue) values indicate positive (negative) a) density anomalies and b) pressure anomalies.

Figs. 29 display reproductions of the steric sea level component in ORAS5 by means of density anomalies from ORAS5 and the Reanalysis mean in the entrance (Fig. 29a) and exit region (Fig. 29b). The comparison serves as a scaling check and determines whether the density calculations represent the considered areas appropriately. Evidently, there is a higher agreement within the exit region ($r_{ORAS5} = 0.97$, $r_{RMEAN} = 0.95$). This is also in agreement with correlation maps between reanalysis-based transport anomalies and sea level anomalies (Figs. 20). By means of Fig. 29a, we found that the entrance region had to be slightly redefined in order to demonstrate the effects of the horizontal pressure gradient. Otherwise, correlations amount to only ∼0.5, and a considerable difference in magnitude occurs. Still, correlations are not as high as within the exit region ($r_{ORAS5} = 0.95$, $r_{RMEAN} = 0.79$). Note that FOAM shows considerable difficulties in the reproduction of SLA in the entrance region and is therefore replaced by its successor FOAMv2 (MacLachlan et al., 2015). FOAMv2 and GLORYS2V4 are responsible for the stronger deviations in the Reanalysis mean at the beginning of the time series and between 2014 and 2016. However, according to these results, we can exclude possible scaling errors.

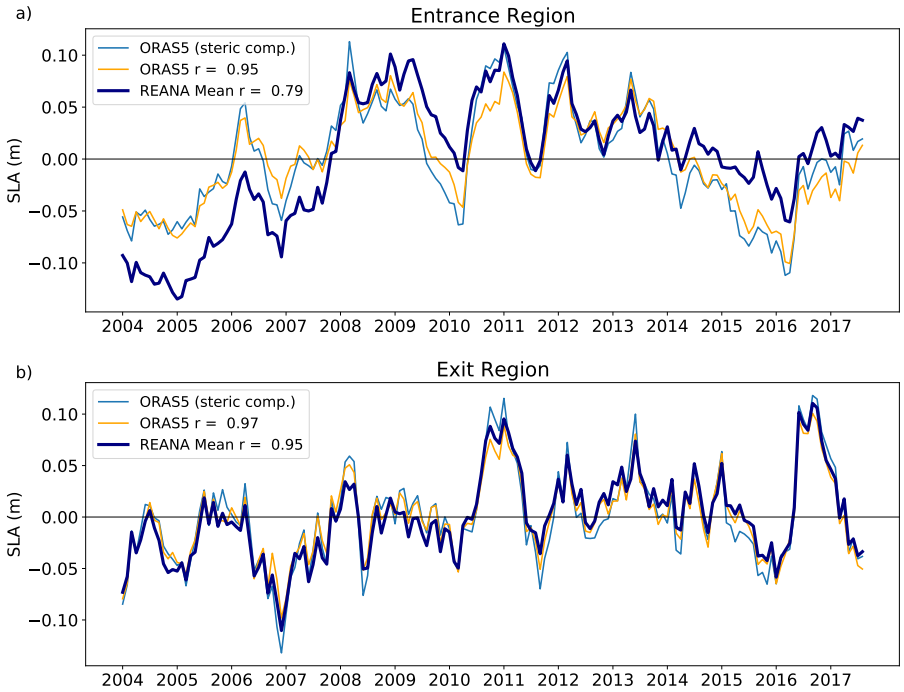

Figure 29: Sea level anomalies scaling check. Area-averaged monthly time series of SLA in a) the western Pacific and b) the eastern Indian Ocean as represented by the steric component from ORAS5 and vertically integrated density anomalies from ORAS5 and the Reanalysis mean.

5.3. ENSO

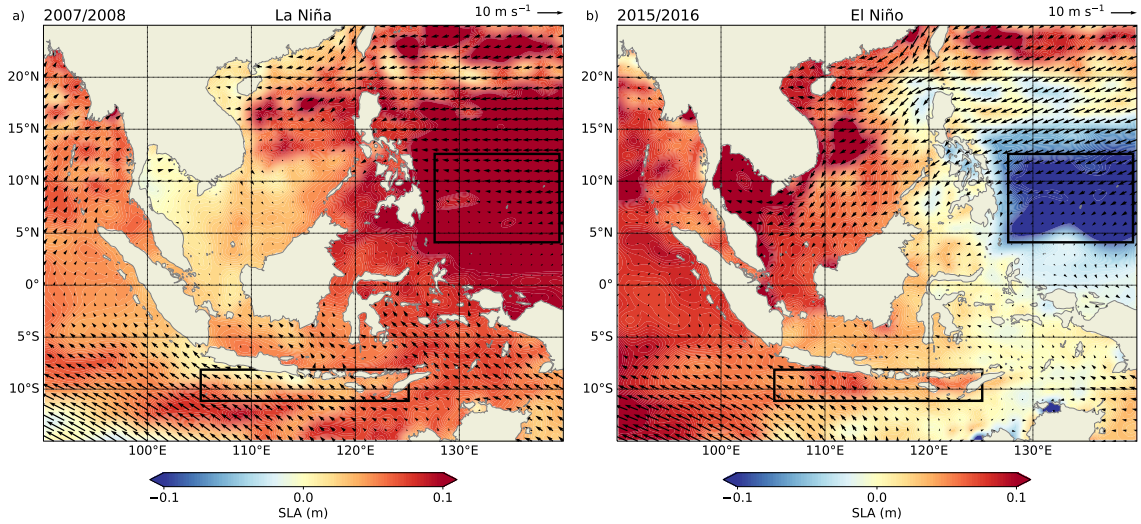

Figure 30: Mean sea level anomalies during a) La Niña 2007/2008 and b) El Niño 2015/2016 as determined by the NINO3.4 index, inferred from satellite-retrieved data between 2004 and 2017. Black arrows represent the corresponding wind regime with the legend in the top right corner. Black boxes indicate relevant areas that modify the large-scale sea level gradient during ENSO.

Chapter 5.2 dealt with the ITF's dependence on sea level gradients between the western Pacific and the eastern Indian Ocean with a special focus on the monsoon phases. The Australian-Indonesian monsoon is not the only phenomenon that affects the ITF. The following chapter demonstrates the connection between the prevailing sea level gradient, which is a result of varying sea level heights in the Pacific and the Indian Ocean, and ITF transport during ENSO. The ITF influences the heat and freshwater budgets of both oceans and may also be considered a primary element during ENSO (Godfrey, 1996). The analysis is based on Fig. 18a, which highlights the La Niña and El Niño phases in the form of blue and red shading, respectively. In order to define ENSO phases, we make use of the NINO3.4 index in which El Niño or La Niña events are defined when the Niño 3.4 SSTs (area-averaged within 5°N - 5°S, 170°W - 120°W) exceed +/- 0.4 °C for a period of six months or more (Trenberth, 2020). Please refer to Fig. 1 for geographical guidance.

Transport through Makassar Strait decreases during El Niño and increases as La Niña sets off (Gordon et al., 2012). Observations in Fig. 18a mimic this behaviour rather well, while Reanalysis products are not able to reproduce it entirely. Therefore, we focus on the La Niña event in 2007/2008 and the strong El Niño event in 2015/2016, where observations and Reanalyses do agree. Volume transport anomalies in Makassar Strait are negative (southward-directed) during La Niña and turn positive (northward-directed) during El Niño. Similar to Figs. 2 we illustrate the state of the sea level anomalies during the chosen La Niña (Fig. 30a) and El Niño (Fig. 30b) events. Moreover, we expanded and shifted the entrance region eastwards towards the NEC bifurcation, which responds to ENSO (Wang et al., 2020). By means of the marked entrance and exit regions in Fig. 30a, we find a southward-directed SLA gradient during the La Niña event in 2007/2008. This is in agreement with the negative, i.e., southward-directed transport anomalies apparent in Fig. 18a. The strong El Niño event in 2015/2016 is accompanied by positive, i.e., northward-directed transport anomalies that are led by the evident northward-directed SLA

gradient in Fig. 30b. Rather than analysing the correlation between transport anomalies and SLA differences, we look at their correlations with the NINO3.4 index (Figs. 32). The linkage between SLA and the temperature-dependent NINO3.4 index is mostly based on steric effects that explain the expansion or contraction of water columns due to temperature and salinity anomalies.

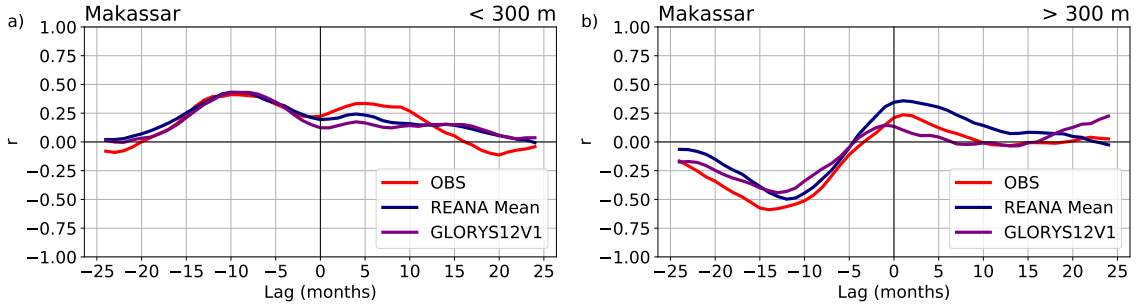

Figure 31: Lead and lag correlations between Makassar transport anomalies and NINO3.4 climate indices in the a) upper (<300 m) and b) lower (>300 m) layer.

Lead and lag correlations for the upper (Fig. 31a) and lower (Fig. 31b) layer help to determine maximum correlations in Figs. 32. According to the peaks of maximum correlation, both upper and lower layer flow lag ENSO, but their response differs. We are about to discuss this behaviour in view of Figs. 32.

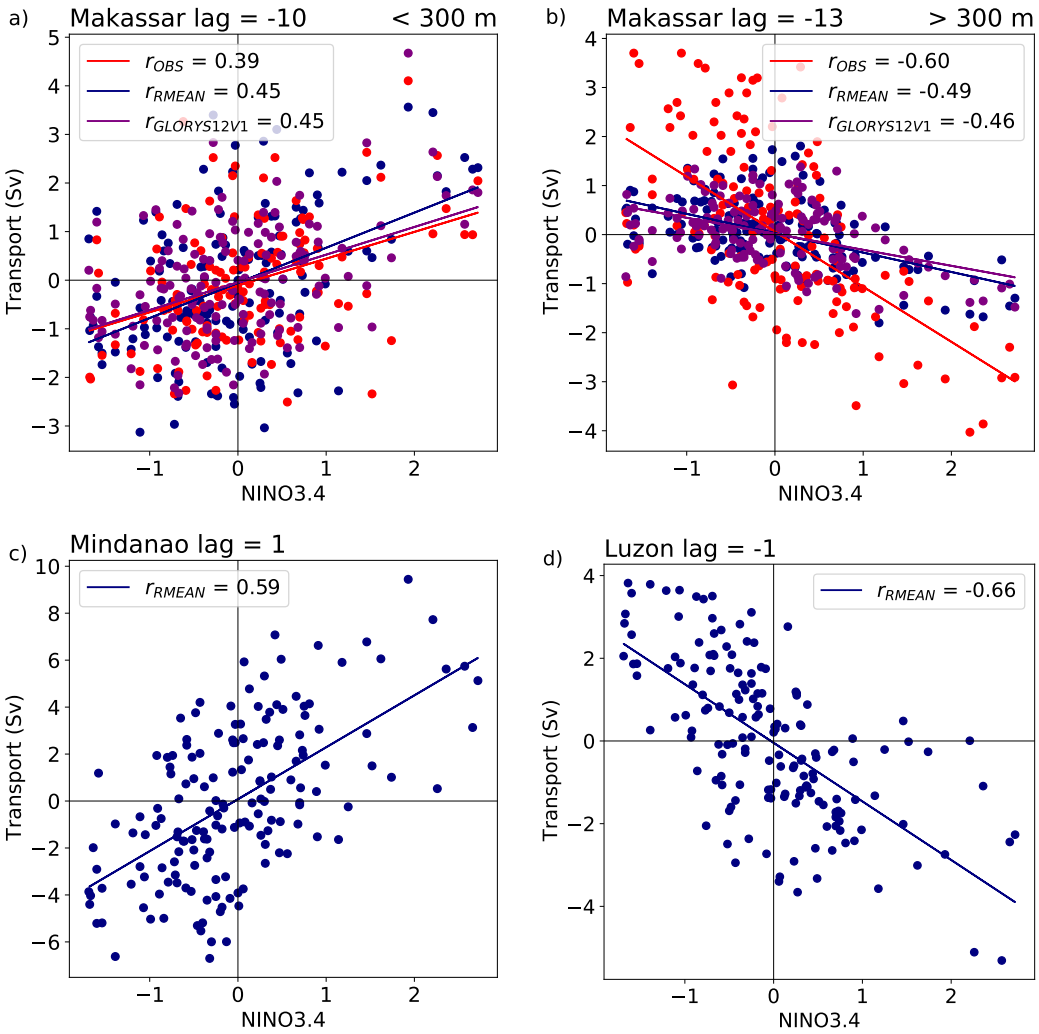

Figure 32: Scatter plots relating a) upper layer (0-300 m) and b) lower layer (300-700 m) integrated transport anomalies through Makassar Strait, full-depth integrated transport anomalies through c) Mindanao Strait and d) Luzon Strait to NINO3.4 indices as represented by observations, Reanalysis mean, and GLORYS12V1 between 2004-2017 at a) lag = -10, b) lag = -13, c) lag = 1, and d) lag = -1. Legends denote Pearson correlation coefficients r.

Figs. 32a-d display relations between transport anomalies and NINO3.4 index anomalies during the extended measuring period from 2004 to 2017. With respect to Makassar Strait the upper (Fig. 32a) and lower (Fig. 32b) layer are assessed separately. The upper 300 m deliver mediocre correlation coefficients of r_{OBS} = 0.39, r_{RMEAN} = 0.45, and $r_{GLORYS12V1}$ = 0.45 with lags in transport by ∼10 months, which is in agreement with findings by Pujiana et al. (2019). Considering full-depth integrated transports r_{OBS} (= 0.49) exceeds r_{RMEAN} (= 0.35) and $r_{GLORYS12V1}$ (= 0.19), but in terms of magnitude, correlations barely improve. Assuming that the flow dynamics during ENSO are explained by the large-scale SLA gradient, we find it reasonable to assess the upper and lower layer in Makassar Strait separately. The lower layer (>300 m) responds negatively to ENSO with an even higher lag in transports of 13 months, which is consistent with findings by Li et al. (2020). The response generally increases, but especially with respect to the observations, r_{OBS} = -0.60. The Reanalysis mean and GLORYS12V1 react marginally stronger to ENSO in the lower layer, reaching maximum correlations of r_{RMEAN} = -0.49 and $r_{GLORYS12V1}$ =

-0.46. Compared to the upper layer, the reversed correlation and the longer response time of deeper ocean transports to ENSO implies, once again, the appearance of two different effects controlling the different layers.

Negative (positive) NINO3.4 indices refer to La Niña (El Niño) events. Therefore, a positive correlation denotes maximum (southward) transport anomalies during La Niña, and minimum (northward) transport anomalies during El Niño. The NINO3.4 index and transport anomalies in the upper layer are positively correlated, with ENSO leading by about 10 months. This indicates a transport decrease (increase) in the upper layer of Makassar about 10 months after and El Niño (La Niña) event. The response to ENSO reverses and increases in the lower layer, with NINO3.4 leading by 13 months.
Seeing that correlations in Figs. 32a and b, but especially in the upper layer, are not particularly high, we look at two more relevant straits. The introduction mentioned two currents, the Mindanao Current and the Kuroshio, that are being fed by the NEC. Their bifurcation point, to the east of the Philippines, undergoes a seasonal cycle and responds to ENSO. The bifurcation latitude shifts towards the North during El Niño (and boreal winter), yielding a stronger transport through Luzon Strait (Gordon et al., 2012). During La Niña (and boreal summer), the bifurcation moves southward, enhancing the transport through Mindanao Strait via Sulawesi Sea into Makassar Strait. Mindanao Strait (Fig. 32c) and Luzon Strait (Fig. 32d), displaying correlation coefficients of 0.59 and -0.66, respectively, are evidently more ENSO sensitive. Note that the flow through Luzon Strait is technically not part of the ITF, but its contribution via Sibutu Passage into Makassar Strait is of importance. There are no observations in these regions, thus, we take advantage of the gridded and complete Reanalysis products. With Mindanao Strait feeding straight into Makassar, we expect them to have the same sign in correlation, indicating westward (eastward) transport anomalies during La Niña (El Niño). Correlation signs of full-depth integrated transport anomalies in Mindanao Strait correspond to that of the upper layer in Makassar. Note that Mindanao and Luzon Strait are North-South oriented. The correlation reverses in Luzon Strait, where La Niña (El Niño) conditions relate to eastward (westward) directed transport anomalies. When considering only upper layer transport anomalies in Mindanao Strait and Luzon Strait, correlations barely change. Lower layer transports, on the other hand, yield weak correlation coefficients of $r_{Mindanao}$ = 0.23 and r_{Luzon} = -0.21. Figs. 33a and b further highlight the difference in contribution to the ITF during La Niña or El Niño.

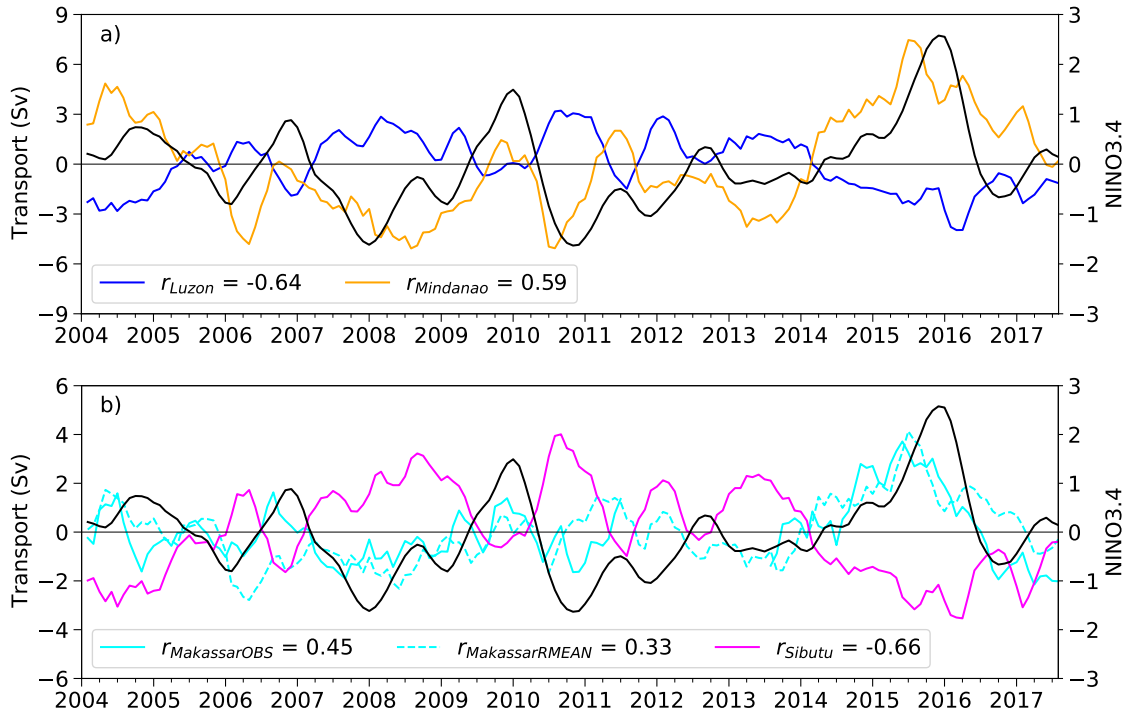

Figure 33: Monthly time series of a) transport anomalies in Luzon Strait and Mindanao Strait (left axis), b) Makassar Strait as represented by observations (OBS) and the Reanalysis mean (RMEAN) and Sibutu Passage, as well as the NINO3.4 index time series (right axis). Correlation coefficients between transport anomalies and the NINO3.4 index are given.

Transport anomalies through Luzon and Mindanao Strait and the NINO3.4 index during the extended measuring period (INSTANT+MITF) between 2004 and 2017 are demonstrated in Fig. 33a. As before, positive (negative) transport anomalies imply an eastward (westward) directed flow, and positive (negative) NINO3.4 indices denote an El Niño (La Niña) event. Correlation coefficients of r_{Luzon} = -0.64 and $r_{Mindanao}$ = 0.59 underline the results in Figs. 32b and c, and the course of anomalies show their contrary mannerism. Accordingly, a El Niño (La Niña) event is accompanied by a stronger flow through Luzon (Mindanao) Strait. Given that Luzon and Mindanao are fairly broad straits with ∼390 km and ∼420 km, respectively, corresponding to approximately 13 and 15 horizontal grid points, Reanalyses have a sufficient amount of reference points to estimate integrated transports. The problems Reanalyses showed earlier, regarding the asymmetry in the flow through the passages, are hardly of relevance with integrated transports. Even small peaks in transport anomalies are being compensated by the respective other strait, for example, in the second half of 2005 or late 2009 and early 2010.
Focusing on the strong El Niño in 2015/2016, we find that the NINO3.4 index does indeed lead transport anomalies in Luzon Strait (max. lag = -1). The Mindanao Current inflow also exhibits ENSO sensitivity, but it is opposite to the Luzon Strait throughflow. Fig. 33b displays full-depth transport anomalies through Makassar Strait and through Sibutu Passage, as well as the NINO3.4 index time series. Correlation coefficients remain mediocre in Makassar Strait ($r_{MakassarOBS}$ = 0.45, $r_{MakassarRMEAN}$ = 0.33) and reverse in Sibutu Passage (r_{Sibutu} = -0.66). The reason we choose to compare transport anomalies between Makassar Strait and Sibutu Passage lies in the fact that their volume transport is determined by Mindanao and Luzon throughflow, respectively. Makassar Strait throughflow displays

an ENSO relationship similar to the Mindanao Strait throughflow and is opposite to the Sibutu Passage throughflow. Moreover, the Sibutu Passage throughflow exhibits an ENSO relationship similar to Luzon Strait.
We have seen that transport through Luzon Strait increases during an El Niño event, and subsequently, larger water masses enter the SCS. Gordon et al. (2012) describe the connection between the ITF and the SCS throughflow in more detail. Water masses from the SCS enter the Indonesian Seas mainly along two paths: either through Mindoro Strait into the Sulu Sea or via Karimata Strait into the Java Sea. At this point, we are interested in the further course through the Sulu Sea. Similar courses ($r = 0.74$) and correlation sign conventions in Luzon Strait and Sibutu Passage imply that the majority of water masses transiting Luzon Strait traverse Sibutu Passage into the Sulawesi Sea, providing a direct connection to the Makassar throughflow. Now the question that arises is: Why does the flow through Makassar decrease during an El Niño event even if the flow through Luzon Strait discharges into the Sulawesi Sea? In order to understand this seemingly contradictory behaviour, we consider velocity profiles in Makassar.

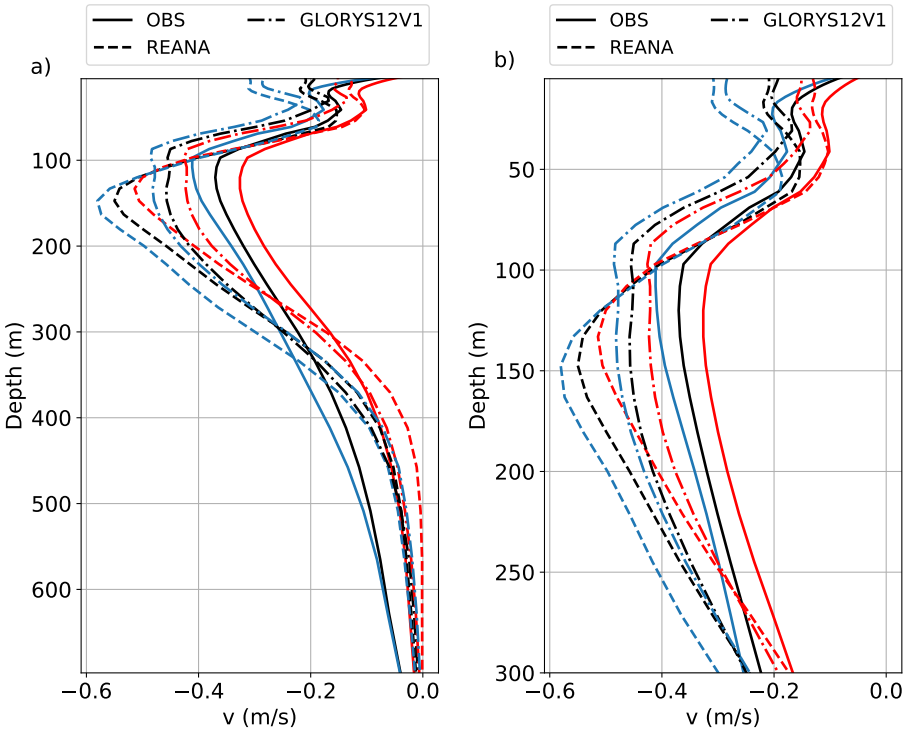

Figure 34: a) Mean vertical profiles (black; 2004-2017) of ASV as represented by observations (continuous lines), Reanalysis mean (dashed lines), and GLORYS12V1 (dash-dot lines). Red and blue lines, respectively, denote average profiles during El Niño 2015/2016 and La Niña 2007/2008. ENSO events are determined by Niño 3.4 SSTs. Negative values indicate southward-directed transport (toward the Indian Ocean). b) Zoom of the upper layer (<300 m).

Figs. 34a and b depict mean vertical profiles of ASV in Makassar Strait during La Niña 2007/2008 (red) and El Niño 2015/2016 (blue). Figs. 12 demonstrated that most of the transport happens between 110 and 130 m, thus, we zoom into the upper layer (<300 m, Fig. 34b). The mean vertical profiles (black), covering the period from 2014 to July 2017, serve for comparison only. We find maximum observed velocities of -0.33 m/s in ∼120 m and -0.41 m/s in ∼110 m during El Niño 2015/2016 and La Niña 2007/2008, respectively.

Magnitudes of current speeds increase throughout La Niña (Gordon et al., 2012). With regard to the Reanalysis mean, maximum velocity increases from -0.52 m/s to -0.58 m/s during La Niña, however, their depth of occurrence increases as well, from 133 m to 147 m. GLORYS12V1 behaves differently again, with an increase in maximum velocity from -0.42 m/s in 97 m to -0.49 m/s in the same depth. The zoomed representation highlights the weak near-surface (<50 m) contribution during El Niño, indicating a decrease in the transport of warmer water.

The reason for the decrease in ITF transport through Makassar Strait during El Niño can be explained through sea level gradients (Eq. 11) within the Sulawesi Sea. With respect to Figs. 30a and b, we define 118°E - 120°E and 1°N - 5°N as the western Sulawesi Sea, and 123°E - 125°E and 1°N - 5°N as the eastern Sulawesi Sea. During La Niña 2007/2008, mean SLA reached 0.08 m and 0.084 m in the western and eastern Sulawesi Sea, respectively, indicating a westward-directed sea level gradient. Note that the scale of SLA ranges between -0.1 m and 0.1 m. The sea level gradient reverses throughout El Niño 2015/2016 when SLA decrease from 0.03 m (western Sulawesi Sea) to 0.01 m (eastern Sulawesi Sea). SLA generally decrease due to the stronger flow through Luzon Strait, and the inversed gradient is a result of the increase in transport into the western Sulawesi Sea via Sibutu Passage. The effect is evidently more pronounced during the longer-lasting El Niño event as the regional west-east gradient in Fig. 30b suggests. An eastward-directed sea level gradient reduces the flow of Mindanao Current surface water into Makassar Strait, explaining minimum or even reversed transport through Makassar during El Niño (Fig. 18). Implied by Eq. 11 this assumption is valid for the near-surface region.

5.4. Conservation of volume within the Indonesian Seas

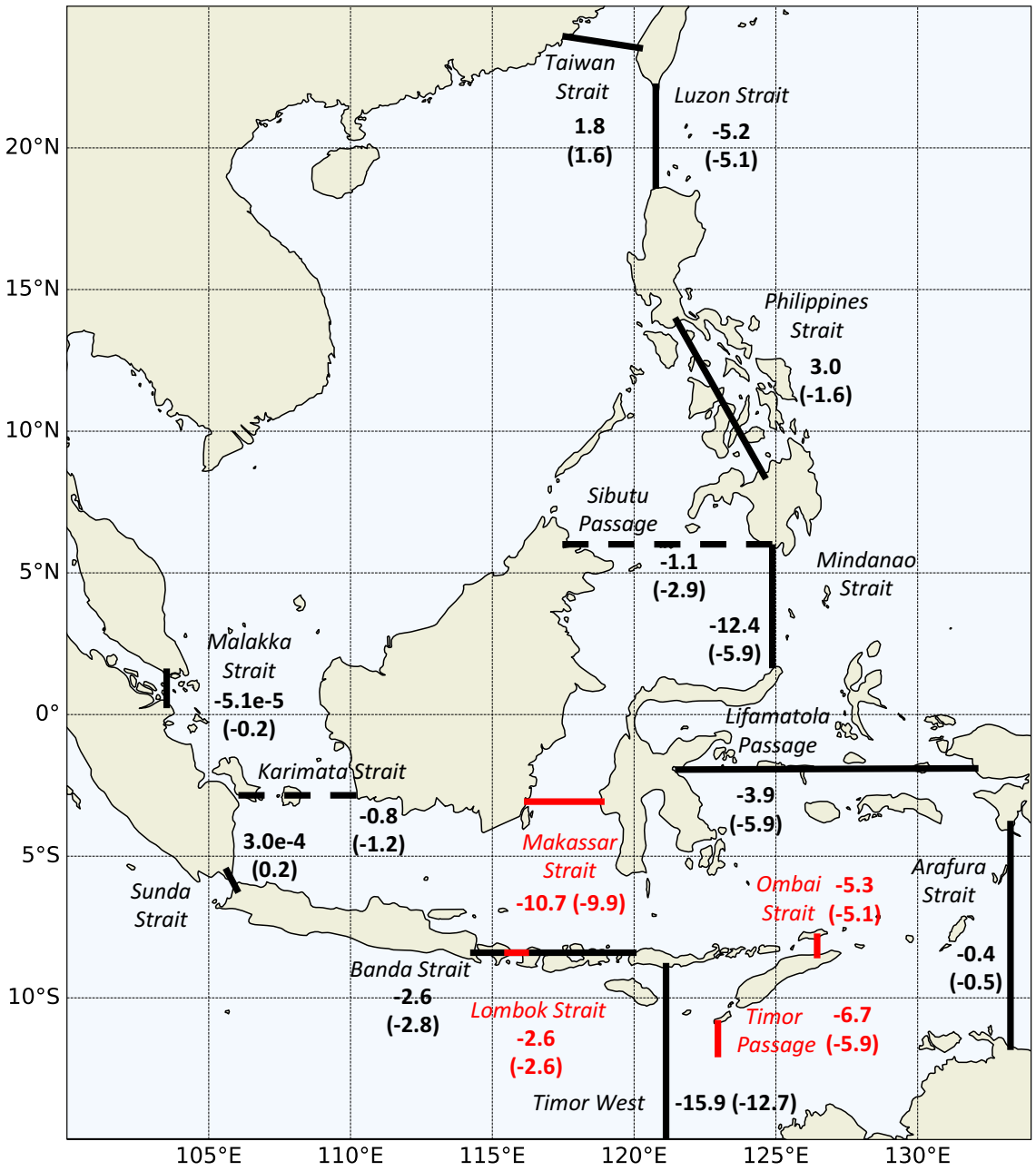

Figure 35: Mean integrated transports covering the extended measuring period from 2004 to 2017. Black continuous lines mark relevant cross sections with their names given in italic font. Bold printed numbers refer to the mean integrated transports as given by the Reanalysis mean and GLORYS12V1 (in brackets). Black dashed lines mark cross sections that are not being considered in the conservation of mass. Red continuous lines mark cross sections where observations are available with their respective names given in red italic font. Bold printed numbers refer to the mean integrated transports as given by the 1/4° and 1/12° (in brackets) bathymetry. The sign convention is such that positive (negative) values indicate northward/eastward (southward/westward) transport, depending on the strait's orientation.

Reanalyses provide the possibility to assess the conservation of volume within the Indonesian Seas. The continuity equation (Eq. 19) states that the inflowing water masses must be compensated by the outflowing water masses. Based on Fig. 35, we are able to distinguish between integrated transports flowing into and out of the Indonesian Seas. Regarding the Reanalysis mean, which has a horizontal resolution of 1/4°, we find a total inflow of |21.9 Sv|, while the total outflow results in |23.3 Sv|. Due to the fact that we are interested in the overall conservation of volume, we use absolute values at this point. Accordingly, a spread of 1.4 Sv remains. The same is done with the higher resolving Reanalysis GLORYS12V1, yielding a total inflow and outflow of |19.2 Sv| and |17.3 Sv|, respectively. We obtain a slightly higher spread of 1.9 Sv. The Reanalysis mean exhibits a stronger outflow than inflow, while GLORYS12V1 features a stronger inflow. The by far most striking difference between the Reanalysis mean and GLORYS12V1 occurs in Mindanao Strait. GLORYS12V1 attains a mean integrated transport (-5.9 Sv) smaller by more than a half compared to the Reanalysis mean (-12.4 Sv). This is caused by an increased number of eastward-directed velocities in GLORYS12V1. Sibutu Passage, exhibiting an overall small but important contribution, almost triples its transport with GLORYS12V1. This is attributed to the fact that GLORYS12V1 is still able to resolve in greater depths and narrow passages along the complex cross section. Differences in magnitude also arise in Lifamatola Passage and Timor West. Note that Timor West extends to the northern coast of Australia. We find a discrepancy in the direction of transport in the Philippines Strait, implying that transport runs eastward in the Reanalysis mean and westward considering GLORYS12V1. The many islands along this cross section pose a real challenge for the 1/4° products. The actual direction of the flow can be determined with GLORYS12V1.
Disregarding the SCS and thus Taiwan Strait, Luzon Strait, Philippines Strait, and Malakka Strait, the total inflow amounts to |18.6 Sv| and to a total outflow of |18.5 Sv|. Considering GLORYS12V1, we find a total inflow and outflow of |16.6 Sv| and |15.5 Sv|, respectively, yielding a spread of 1.1 Sv. Considering a smaller area that still covers the entirety of the ITF improves the accuracy of conservation of volume.

Budgets based on Reanalysis data have to be considered with caution. The assimilation of sea level trends in Reanalyses is implemented by comparing altimeter-retrieved global mean sea level trends with the trends in steric height from the ocean analysis (Balmaseda et al., 2013). This way, the component of global mean sea level change that is based on changes in water mass can be estimated. The segmentation into the steric component and the mass component is used to close the fresh-water budget over the oceans. The steric component is, however, not a prognostic variable, and the Boussinesq approximation is made, implying that the ocean model (NEMO) conserves volume rather than mass. Since the steric component is therefore not explicitly defined, the approach to close the fresh-water budget in Ocean Reanalyses is accompanied by uncertainty.

6. Conclusions and Outlook

The results of this work are ultimately based on two research questions that are introduced in Section 3. Firstly, the skill of different Ocean Reanalysis products within the bathymetrically complex straits of Makassar, Lombok, Ombai, and Timor was assessed. We implemented this by drawing various comparisons between Reanalysis products and mooring observations. This required uniform preprocessing between both data types, which was adapted and improved several times in the course of this work. The effect of mooring blow-over, incomplete or absent data files, and inconsistencies in data formats complicate the preprocessing of observational data. The bathymetry that was used to laterally extrapolate the along strait velocities represents an important factor in the preprocessing method. The level of agreement with transport values from the literature strongly depends on the chosen bathymetry, especially in regions with lots of islands and narrow straits, such as the Indonesian Archipelago. By employing the land-sea mask from Reanalysis products for both data types, we accounted for a fair comparison. Through the systematic preparation of the data sets and testing of different approaches, we came to realise that transport estimates in these narrow passages can be highly sensitive to the chosen bathymetry. Furthermore, the study included a detailed analysis of the cross-sectional distribution of along strait velocities in the different straits. Considering full-field velocity cross sections (Figs. 6 and 7), the most striking finding was that Reanalyses do not seem to get asymmetries in the flow through the passages right. GLORYS12V1 exhibited a slightly better performance regarding this matter due to the three times higher resolution of horizontal grid points. Comparisons between observations and nearest neighbours or interpolated profiles (Figs. 8, 9, and 12) revealed that Reanalysis products are able to capture the shape of observed velocity profiles well, but they over- and underestimate their magnitude and to some extent quite severely. Aside from a more representative depiction of maximum values in Makassar and Ombai Strait, we did not find a considerable advantage with GLORYS12V1 (Fig. 13a). We quantified how accurately the transport through cross sections is captured by only observing at selected sites (Figs. 10 and 11), i.e., mooring sites, and established that the flow is indeed well represented based on the results from Reanalysis data. Given that the asymmetry problem is solved, Reanalyses could be used for the selection of suitable mooring sites. GLORYS12V1 showed substantial advantages with integrated transport estimates, particularly in the more narrow straits of Ombai and Lombok (Fig. 13b). This is most likely again a result of the more closely spaced grid points and, thus, an advantage in the shaping of the flow. The compilation of along strait velocity cross sections highlighted that estimation of integrated transports requires careful quantification of sampling uncertainty and must be assessed by preparing the data individually for each strait. It should also be noted again that current measurements from moorings are not assimilated in Ocean Reanalysis products. Despite the partially substantial over- and underestimation of velocity magnitudes by Reanalyses, the Reanalysis mean did include the observations in most cases. Thus, the Reanalyses appear as suitable references for comparisons with the ocean components of the CMIP5 (Taylor et al., 2012) and CMIP6 models (Eyring et al., 2016). Nevertheless, long-term observations are needed to sample longer-lasting variabilities such as ENSO or the IOD reasonably.

Secondly, we focused on the large-scale sea level gradient that regulates the ITF transport on a seasonal scale. We found that ITF transport anomalies through Makassar Strait are southward (northward) directed when mean sea level anomalies are higher in the western Pacific (eastern Indian Ocean) (Figs. 22). In addition, transport is strongest during the SE

monsoon. An interesting result is the occurrence of an apparent two-layer system that is responsible for flow reversals in the lower layer (>300 m). Results suggest a strong influence of the sea level gradient in the upper layer (<300 m) (Figs. 22 and 24). The reversal of correlations in the lower layer is incompatible with the large-scale sea level gradient and implies the appearance of other processes. Seeing that the flow response reverses, it could be due to baroclinic effects influencing the pressure gradient at greater depths. The assessment of the depth-dependent horizontal pressure gradient (Fig. 27) displayed a decrease with depth and accordingly with current speeds, proving that the sea level gradient can regulate the flow only in the upper ∼300 m. We did not get to the bottom of the actual lower layer processes, but they have been attributed to baroclinic Kelvin waves originating in the Indian Ocean (Pujiana et al., 2019) and to Rossby waves propagating from the Pacific (Li et al., 2020). At present, literature on this topic is sparse. However, the two-layer system has so far been presented mainly in conjunction with ENSO.
Considering the Chapter on ENSO, we found interesting linkages between the ITF and the ENSO-relevant SCS throughflow that can be investigated with the use of Reanalyses. Transport through Makassar Strait decreases during El Niño and can partly be attributed to a local sea level gradient in the Sulawesi Sea. Enhanced transports through Luzon Strait are the other reason for a decrease in transport. The two-layer system is also reflected in the ENSO analysis with an even higher lagged response to ENSO in the lower layer.

A continuation of this work should include the investigation of lower-layer processes that are responsible for reversing the horizontal pressure gradient. The lack of current literature on this topic indicates that there is still a lot to analyse. Baroclinic Kelvin waves originate in the equatorial Indian Ocean as a result of anomalous wind forcing. The effect of possibly baroclinic processes, apparent in Makassar Strait, should thus be traced further back to their points and mechanisms of origin. The same applies to baroclinic Rossby waves intruding into the ITF from the equatorial Pacific.
Furthermore, we did not assess the performance of individual products on a technical basis, i.e., based on differences in their implementation. Investigating differences between Reanalysis data based on their model physics and assimilation schemes most likely yields insights into more subtle variations. In the course of this work, we made use of the Reanalysis mean (GREP) and focused on the comparison with GLORYS12V1. Seeing that GLORYS12V1 exhibits notable advantages in regions such as the Indonesian Archipelago, comparisons with other high-resolution products would be appropriate.

Acknowledgements

I would first like to thank my thesis advisors Prof. Leopold Haimberger and Dr. Michael Mayer, for their continuous support and scientific guidance. Their regular input and valuable suggestions encouraged me to pursue an oceanographic-based topic and to always consider a result from different angles. I also want to sincerely thank Susanna Winkelbauer for showing me how to handle Ocean Reanalyses data at the beginning and for taking the time to answer my questions.

My sincere thanks to Rebecca Cowley from CSIRO (Commonwealth Scientific and Industrial Research Organisation) for clarifying any issues with the INSTANT data set and for cross-checking my first attempts.

Further, I would like to acknowledge the help of Janet Sprintall from UC San Diego, Scripps Institution of Oceanography, for sharing her opinion on our preprocessing method and providing additional material.

References

Aanderaa. Aanderaa Instruments: Data collecting instruments for land sea and air. 2001. Retrieved from: https://epic.awi.de/id/eprint/45145/1/RCM9.pdf [accessed 07 September 2022].

A. Arakawa and V. Lamb. Computational Design of the Basic Dynamical Processes of the UCLA General Circulation Model. *Methods in Computational Physics: Advances in Research and Applications*, 17:173–265, 1977. doi: https://doi.org/10.1016/B978-0-12-460817-7.50009-4.

Argo. Argo float data and metadata from Global Data Assembly Centre (Argo GDAC). *SEANOE*, 2000. doi: https://doi.org/10.17882/42182.

M. Balmaseda, K. Mogensen, and A. Weaver. Evaluation of the ECMWF ocean reanalysis system ORAS4. *Quarterly Journal of the Royal Meteorological Society,*, 139:1132–1161, 2013. doi: https://doi.org/10.1002/qj.2063.

J. Boussinesq. Théorie Analytique de la Chaleur. *Gathier-Vellars*, 2:172 pp., 1903.

R. Boy. Lombok Strait: An Indonesian Throughflow Passage. *Oseana*, 2:33–40, 1995.

P. Brasseur and J. Verron. The SEEK Filter Method for Data Assimilation in Oceanography: A Synthesis. *Ocean Dynamics*, 56:650–661, 2006. doi: https://doi.org/10.1007/s10236-006-0080-3.

C. Cabanes, A. Grouazel, K. von Schuckmann, M. Hamon, V. Turpin, and C. Coatanoan. The CORA Dataset: Validation and Diagnostics of In-Situ Ocean Temperature and Salinity Measurements. *Ocean Science*, 9:1–18, 2013. doi: http://dx.doi.org/10.5194/os-9-1-2013.

A. J. Clarke. On the reflection and transmission of low-frequency energy at the irregular western Pacific Ocean boundary. *Journal of Geophysical Research*, 96:3289–3305, 1991. doi: https://doi.org/10.1029/90JC00985.

A. J. Clarke and X. Liu. Observations and dynamics of semiannual and annual sea levels near the eastern equatorial Indian Ocean boundary. *Journal of Physical Oceanography*, 23:386–399, 1993. doi: https://doi.org/10.1175/1520-0485(1993)023<0386:OADOSA>2.0.CO;2.

A. J. Clarke and X. Liu. Interannual sea level in the northern and eastern Indian Ocean. *Journal of Physical Oceanography*, 24:1224–1235, 1994. doi: https://doi.org/10.1175/1520-0485(1994)024<1224:ISLITN>2.0.CO;2.

C. C. S. CMEMS. Global Ocean Gridded L4 Sea Surface Heights and Derived Variables Reprocessed. 2021a. Retrieved from: https://doi.org/10.48670/moi-00145 [accessed 15 July 2022].

C. C. S. CMEMS. ORAS5 global ocean reanalysis monthly data from 1958 to present. 2021b. Retrieved from: https://cds.climate.copernicus.eu/cdsapp#!/dataset/reanalysis-oras5?tab=overview [accessed 28 May 2022].

I. P. F. Council. Indo Pacific Fisheries Council: Proceedings. *Directory of Fisheries Institutions, Asia and the Far East*, 1957. Retrieved from: https://www.fao.org/3/bm017e/bm017e.pdf [accessed 18 July 2022].

R. Cowley, B. Heaney, S. Wijffels, L. Pender, J. Sprintall, S. Kawamoto, and R. Molcard. INSTANT Sunda Data Report Description and Quality Control. *CSIRO Marine and Atmospheric Research*, 2009.

G. Cresswell. Coastal currents of northern Papua New Guinea, and the Sepik River outflow. *Marine and Freshwater Research*, 51:553–564, 2000. doi: http://dx.doi.org/10.1071/MF99135.

D. Dee, S. Uppala, A. Simmons, P. Berrisford, P. Poli, S. Kobayashi, U. Andrae, M. Balmaseda, G. Balsamo, P. Bauer, P. Bechtold, A. Beljaars, L. van de Berg, J. Bidlot, N. Bormann, C. Delsol, R. Dragani, M. Fuentes, A. Geer, and F. Vitart. The ERA-Interim reanalysis: configuration and performance of the data assimilation system. *Quarterly Journal of the Royal Meteorological Society*, 137(656):553–597, 2011. doi: https://doi.org/10.1002/qj.828.

C. Desportes, M. Drévillon, Y. Drillet, G. Garric, L. Parent, C. Régnier, S. Masina, A. Storto, D. Petterson, R. Wood, M. Balmaseda, and H. Zuo. GREP: Evaluation of the Copernicus Marine Service Global Reanalysis Ensemble Product: deriving uncertainty estimates for 3D T and S variability in the ocean. *EGU General Assembly Conference Abstracts*, page 16232, 2017. doi: https://ui.adsabs.harvard.edu/abs/2017EGUGA..1916232D.

K. Drushka, J. Sprintall, S. T. Gille, and I. Brodjonegoro. Vertical structure of Kelvin waves in the Indonesian Throughflow exit passages. *Journal of Physical Oceanography*, 40:1965 – 1987, 2010. doi: https://doi.org/10.1175/2010JPO4380.1.

ECMWF. Fact sheet: Reanalysis. 2020. Retrieved from: https://www.ecmwf.int/sites/default/files/medialibrary/2020-06/ecmwf-fact-sheet-reanalysis.pdf [accessed 07 September 2022].

V. W. Ekman. On the Influence of the Earth's Rotation on Ocean-Currents. *Arkiv For Matematik, Astronimi och Fysik*, 1905.

V. Eyring, S. Bony, G. A. Meehl, C. A. Senior, B. Stevens, R. J. Stouffer, and K. E. Taylor. Overview of the Coupled Model Intercomparison Project Phase 6 (CMIP6) experimental design and organization. *Geoscientific Model Development*, 9:1937–1958, 2016. doi: https://doi.org/10.5194/gmd-9-1937-2016.

Falmouth Scientific Inc. FSI ACM-PLUS. 2014. Retrieved from: https://www.comm-tec.com/Docs/Brochure/FSI/FSI_ACM-PLUS-21jan2014.pdf [accessed 22 Apr 2022].

G. Fang, Y. Wang, Z. Wei, Y. Fang, F. Qiao, and X. Hu. Interocean circulation and heat and freshwater budgets of the South China Sea based on a numerical model. *Dynamics of Atmospheres and Oceans*, 47:55–72, 2009. doi: https://doi.org/10.1016/j.dynatmoce.2008.09.003.

A. Ffield and A. L. Gordon. Vertical mixing in the Indonesian thermocline. *Journal of Physical Oceanography*, 22:184–195, 1992. doi: 10.1175/1520-0485(1992)022<0184:VMITIT>2.0.CO;2.

G. Garric and L. Parent. Quality Information Document For Global Ocean Reanalysis Products. 2017. Retrieved from: https://catalogue.marine.copernicus.eu/documents/QUID/CMEMS-GLO-QUID-001-025.pdf [accessed 28 May 2022].

GEOMAR. Ozean-Modelle HPC. 2022. Retrieved from: https://www.geomar.de/?id=3961&L=1 [accessed 25 Sep 2022].

T. Gilboy, T. Dickey, D. Sigurdson, X. Yu, and D. Manov. An Intercomparison of Current Measurements Using a Vector Measuring Current Meter, an Acoustic Doppler Current Profiler, and a Recently Developed Acoustic Current Meter. *Journal of Atmospheric and Oceanic Technology*, 17(4):561–574, 2000. doi: https://doi.org/10.1175/1520-0426(2000)017<0561:AIOCMU>2.0.CO;2.

J. Godfrey. A Sverdrup model of the depth-integrated flow for the world ocean allowing for island circulations. *Geophysical Astrophysical Fluid Dynamics*, 45:89–112, 1989. doi: https://doi.org/10.1080/03091928908208894.

J. Godfrey. The effect of the Indonesian Throughflow on ocean circulation and heat exchange with the atmosphere: A review. *Journal of Geophysical Research*, 101(C5):12217–12237, 1996. doi: https://doi.org/10.1029/95JC03860.

S. Good, M. Martin, and N. Rayner. EN4: quality controlled ocean temperature and salinity profiles and monthly objective analyses with uncertainty estimates. *Journal of Geophysical Research: Oceans*, 118:6704–6716, 2013. doi: https://doi.org/10.1002/2013JC009067.

A. Gordon. Oceanography of the Indonesian Seas and Their Throughflow. *Oceanography*, 18(4):14–27, 2005. doi: http://dx.doi.org/10.5670/oceanog.2005.01.

A. Gordon, R. Susanto, A. Ffield, B. Huber, W. Pranowo, and S. Wirasantosa. Makassar Strait throughflow, 2004 to 2006. *Geophysical Research Letter*, 2008. doi: http://dx.doi.org/10.1029/2008GL036372.

A. L. Gordon and J. L. McClean. Thermohaline Stratification of the Indonesian Seas: Model and Observations. *Journal of Physical Oceanography*, 29:198–216, 1999. doi: https://doi.org/10.1175/1520-0485(1999)029<0198:TSOTIS>2.0.CO;2.

A. L. Gordon, S. Ma, D. B. Olson, P. Hacker, A. Ffield, L. D. Talley, D. Wilson, and M. Baringer. Advection and diffusion of Indonesian Throughflow water within the Indian Ocean South Equatorial Current. *Geophysical Research Letters*, 24:2573–2576, 1997. doi: https://doi.org/10.1029/97GL01061.

A. L. Gordon, B. A. Huber, J. E. Metzger, D. R. Susanto, H. E. Hurlburt, and R. T. Adi. South China Sea throughflow impact on the Indonesian throughflow. *Geophysical Research Letters*, 39, 2012. doi: https://doi.org/10.1029/2012GL052021.

A. L. Gordon, A. Napitu, B. A. Huber, L. K. Gruenburg, K. Pujiana, and T. Agustiadi. Makassar Strait Throughflow Seasonal and Interannual Variability: An Overview. *Journal of Geophysical Research: Oceans*, 124:3724–3736, 2019. doi: https://doi.org/10.1029/2018JC014502.

R. J. Greatbatch. A note on the representation of steric sea level in models that conserve volume rather than mass. *Journal of Geophysical Research: Oceans*, 99:12,767–12,771, 1994. doi: https://doi.org/10.1029/94JC00847.

D. Halpern, R. Weller, M. Briscoe, R. Davis, and J. McCullough. Intercomparison tests of moored current measurements in the upper ocean. *Journal of Geophysical Research*, 86: 419–428, 1981. doi: https://doi.org/10.1029/JC086iC01p00419.

M. Hantel. Einführung Theoretische Meteorologie. 2013. doi: https://doi.org/10.1007/978-3-8274-3056-4.

M. Hantel and L. Haimberger. Grundkurs Klima. *Springer-Verlag Berlin Heidelberg*, 1, 2016. doi: https://doi.org/10.1007/978-3-662-48193-6.

S. L. Hautala, J. L. Reid, and N. Bray. The distribution and mixing of Pacific water masses in the Indonesian Seas. *Journal of Geophysical Research*, 101:12375–12389, 1996. doi: https://doi.org/10.1029/96JC00037.

H. Hersbach, B. Bell, P. Berrisford, G. Biavati, A. Horányi, J. Muñoz Sabater, J. Nicolas, C. Peubey, R. Radu, I. Rozum, D. Schepers, A. Simmons, C. Soci, D. Dee, and J.-N. Thépaut. ERA5 monthly averaged data on single levels from 1959 to present. Copernicus Climate Change Service (C3S) Climate Data Store (CDS). 2019. doi: 10.24381/cds.f17050d7.

D. Hosom, R. Weller, G. Allsup, S. Anderson, and R. Trask. Upgraded vector measuring current meter. *Oceans '99. MTS/IEEE. Riding the Crest into the 21st Century. Conference and Exhibition. Conference Proceedings (IEEE Cat. No.99CH37008)*, 1:377–381, 1999. doi: https://doi.org/10.1109/OCEANS.1996.572558.

E. Hovmoeller. The Trough-and-Ridge diagram. *Tellus*, 1:62–66, 1949. doi: https://doi.org/10.1111/j.2153-3490.1949.tb01260.x.

E. Hunke and W. Lipscomb. CICE: the Los Alamos sea ice model. Documentation and software users manual Version 4.1. 2010. Retrieved from: https://csdms.colorado.edu/w/images/CICE_documentation_and_software_user%27s_manual.pdf [accessed 29 May 2022].

W. H. O. Institution. Acoustic Doppler Current Profiler (ADCP). 2022. Retrieved from: https://www.whoi.edu/what-we-do/explore/instruments/instruments-sensors-samplers/acoustic-doppler-current-profiler-adcp/ [accessed 22 Apr 2022].

R. Kalman. A New Approach to Linear Filtering and Prediction Problems. *Journal of Basic Engineering*, 82:35–45, 1960. doi: https://doi.org/10.1115/1.3662552.

A. Koch-Larrouy, G. Madec, P. Bouruet-Aubertot, T. Gerkema, L. Bessieres, and R. Molcard. On the transformation of Pacific Water into Indonesian Throughflow Water by internal tidal mixing. *Geophysical Research Letters*, 34:L04604, 2007. doi: http://dx.doi.org/10.1029/2006GL028405.

W. G. Large and S. Yeager. Diurnal to decadal global forcing for ocean and sea-ice models: the data sets and flux climatologies. *NCAR Technical Note, NCAR/TN-460+STR, CGD Division of the National Center for Atmospheric Research*, 2004.

J.-M. Lellouche, E. Greiner, R. Bourdallé-Badie, G. Garric, A. Melet, M. Drévillon, C. Bricaud, M. Hamon, O. Le Galloudec, C. Regnier, T. Candela, C.-E. Testut, F. Gasparin, G. Ruggiero, M. Benkiran, Y. Drillet, and P.-Y. Le Traon. The Copernicus Global 1/12°

Oceanic and Sea Ice GLORYS12 Reanalysis. *Frontiers in Earth Science (Lausanne)*, 9, 2021. doi: https://doi.org/10.3389/feart.2021.698876.

M. Li, J. Wei, D. Wang, A. L. Gordon, S. Yang, P. Malanotte-Rizzoli, and G. Jiang. Exploring the importance of the Mindoro-Sibutu pathway to the upper-layer circulation of the South China Sea and the Indonesian Throughflow. *Journal of Geophysical Research: Oceans*, 124:5054–5066, 2019. doi: https://doi.org/10.1029/2018JC014910.

M. Li, A. L. Gordon, L. K. Gruenburg, J. Wei, and S. Yang. Interannual to decadal response of the indonesian throughflow vertical profile to Indo- Pacific forcing. *Geophysical Research Letters*, 47, 2020. doi: https://doi.org/10.1029/2020GL087679.

Q. Liu, M. Feng, D. Wang, and S. Wijffels. Interannual variability of the Indonesian Throughflow transport: A revisit based on 30 year expendable bathythermograph data. *Journal of Geophysical Research: Oceans*, 120, 2015. doi: https://doi.org/10.1002/2015JC011351.

Y. Liu, M. Feng, J. Church, and D. Wang. Effect of Salinity on Estimating Geostrophic Transport of the Indonesian Throughflow along the IX1 XBT Section. *Journal of Oceanography*, 61:795–801, 2005. doi: https://doi.org/10.1007/s10872-005-0086-3.

C. MacLachlan, A. Arribas, K. A. Peterson, A. Maidens, D. Fereday, A. A. Scaife, M. Gordon, M. Vellinga, A. Williams, R. E. Comer, J. Camp, P. Xavier, and G. Madec. Global Seasonal forecast system version 5 (GloSea5): a high-resolution seasonal forecast system. *Quarterly Journal of the Royal Meteorological Society*, 141(689):1072–1084, 2015. doi: https://doi.org/10.1002/qj.2396.

R. Madden and P. Julian. Description of Global-Scale Circulation Cells in the Tropics with a 40–50 Day Period . *Journal of the Atmospheric Sciences*, 29:1109–1123, 1972. doi: https://doi.org/10.1175/1520-0469(1972)029<1109:DOGSCC>2.0.CO;2.

G. Madec and M. Imbard. A global ocean mesh to overcome the North Pole singularity. *Climate Dynamics*, 12(6):381–388, 1996. doi: https://doi.org/10.1007/BF00211684.

G. Madec, R. Bourdallé-Badie, J. Chanut, E. Clementi, A. Coward, C. Ethé, D. Iovino, D. Lea, C. Lévy, T. Lovato, N. Martin, S. Masson, S. Mocavero, C. Rousset, D. Storkey, S. Müeller, G. Nurser, M. Bell, G. Samson, and A. Moulin. NEMO ocean engine. Note du Pole de modélisation. *Institut Pierre-Simon Laplace (IPSL), France*, 27, 2008.

J. Marshall and R. Plumb. Atmosphere, Ocean and Climate Dynamics: An Introductory Text. Chapter 9, The ocean and its circulation. *Elsevier Science Technology*, pages 163–195, 2007.

Y. Masumoto and T. Yamagata. Seasonal variations of the Indonesian throughflow in a general ocean circulation model. *Journal of Geophysical Research*, 101:12287–12293, 1996. doi: https://doi-org.uaccess.univie.ac.at/10.1029/95JC03870.

M. Mayer and M. Alonso Balmaseda. Indian Ocean impact on ENSO evolution 2014-2016 in a set of seasonal forecasting experiments. *Climate Dynamics*, 56:2631–2649, 2021. doi: https://doi.org/10.1007/s00382-020-05607-6.

M. Mayer, M. A. Balmaseda, and L. Haimberger. Unprecedented 2015/2016 Indo-Pacific heat transfer speeds up tropical Pacific heat recharge. *Geophysical Research Letters*, 45: 3274–3284, 2018. doi: https://doi.org/10.1002/2018GL077106.

A. Meindl. Guide to Moored Buoys and Other Ocean Data Acquisition Systems. DBCP Technical Document. *World Meteorological Organization (WMO); Intergovernmental Oceanographic Commission*, 8, 1996.

C. Merchant, O. Embury, and C. Bulgin. Satellite-based time-series of sea-surface temperature since 1981 for climate applications. *Scientific Data*, 6:223, 2019. doi: https://doi.org/10.1038/s41597-019-0236-x.

G. Meyers. Variation of the Indonesian throughflow and the El Niño–Southern Oscillation. *Journal of Geophysical Research Atmospheres*, 101:12255–12263, 1996. doi: http://dx.doi.org/10.1029/95JC03729.

K. Mogensen, M. Balmaseda, and A. Weaver. The NEMOVAR ocean data assimilation system as implemented in the ECMWF ocean analysis for System 4. 2012. Retrieved from: https://www.ecmwf.int/file/23284/download?token=L2fInOlQ [accessed 28 May 2022].

R. Molcard, M. Fieux, and A. Ilahude. The Indo-Pacific Throughflow in the Timor Passage. *Journal of Geophysical Research*, 1011:12411–12420, 1996. doi: http://dx.doi.org/10.1029/95JC03565.

R. Molcard, M. Fieux, and F. Syamsudin. The throughflow within Ombai Strait. *Deep-sea Research Part I-oceanographic Research Papers*, 48:1237–1253, 2001. doi: http://dx.doi.org/10.1016/S0967-0637(00)00084-4.

M. Nieva Tamasiunas, T. Shinoda, R. Susanto, L. Zamudio, and J. Metzger. Intraseasonal variability of the Indonesian throughflow associated with the Madden-Julian Oscillation. *Deep Sea Research Part II: Topical Studies in Oceanography*, 193:104985, 2021. doi: https://doi.org/10.1016/j.dsr2.2021.104985.

V. Nieves, J. Willis, and W. Patzert. Recent hiatus caused by decadal shift in Indo-Pacific heating. *Science*, 349(6247):532–535, 2015. doi: https://doi.org/10.1126/science.aaa4521.

NOAA. Acoustic Doppler Current Profiler. 2008. Retrieved from: https://oceanexplorer.noaa.gov/technology/acoust-doppler/acoust-doppler.html [accessed 22 Apr 2022].

NOAA. Niño 3.4 SST Index. 2021. Retrieved from: https://psl.noaa.gov/gcos_wgsp/Timeseries/Data/nino34.long.data [accessed 15 July 2022].

A. Nortek. Aquadopp Current Meter. 2018. Retrieved from: https://rts.as/wp-content/uploads/2018/09/Nortek-Aquadopp-Current-Meter.pdf [accessed 07 September 2022].

B. Peña-Molino, B. Sloyan, M. Nikurashin, O. Richet, and S. E. Wijffels. Revisiting the seasonal cycle of the Timor throughflow: Impacts of winds, waves and eddies. *Journal of Geophysical Research: Oceans*, 127, 2022. doi: https://doi.org/10.1029/2021JC018133.

A. Piola and A. Gordon. Pacific and Indian Ocean Upper-Layer Salinity Budget. *Journal of Physical Oceanography*, 14:747–753, 1984. doi: https://doi.org/10.1175/1520-0485(1984)014<0747:PAIOUL>2.0.CO;2.

J. Potemra, S. Hautala, J. Sprintall, and W. Pandoe. Interaction between the Indonesian Seas and the Indian Ocean in observations and numerical models. *Journal of Physical Oceanography*, 32:1838–1854, 2002. doi: https://doi.org/10.1175/1520-0485(2002)032<1838:IBTISA>2.0.CO;2.

J. Potemra, S. Hautala, and J. Sprintall. Vertical structure of Indonesian throughflow in a large-scale model. *Deep Sea Research, Part II*, 50:2143–2161, 2003. doi: https://doi.org/10.1016/S0967-0645(03)00050-X.

J. T. Potemra. Seasonal Variations of Upper Ocean Transport from the Pacific to the Indian Ocean via Indonesian Straits. *Journal of Physical Oceanography*, 29:2930–2944, 1999. doi: https://doi.org/10.1175/1520-0485(1999)029<2930:SVOUOT>2.0.CO;2.

J. T. Potemra and N. Schneider. Interannual variations of the Indonesian Throughflow. *Journal of Geophysical Research*, 112, 2007. doi: https://doi.org/10.1029/2006JC003808.

K. Pujiana, A. Gordon, and J. Sprintall. Intraseasonal Kelvin wave in Makassar Strait. *Journal of Geophysical Research: Oceans*, 118:2023–2034, 2013. doi: https://doi.org/10.1002/jgrc.20069.

K. Pujiana, M. J. McPhaden, A. L. Gordon, and A. Napitu. Unprecedented Response of Indonesian Throughflow to Anomalous Indo-Pacific Climatic Forcing in 2016. *Journal of Geophysical Research: Oceans*, 124:3737–3754, 2019. doi: https://doi.org/10.1029/2018JC014574.

M. Pujol, Y. Faugère, G. Taburet, S. Dupuy, C. Pelloquin, M. Ablain, and N. Picot. DUACS DT2014: the new multi-mission altimeter data set reprocessed over 20 years. *Ocean Science*, 12(5):1067–1090, 2016. doi: https://doi.org/10.5194/os-12-1067-2016.

T. Qu and L. Roger. The Bifurcation of the North Equatorial Current in the Pacific. *Journal of Physical Oceanography*, 33(1):5–18, 2003. doi: https://doi.org/10.1175/1520-0485(2003)033<0005:TBOTNE>2.0.CO;2.

T. Qu, Y. Y. Kim, M. Yaremchuk, T. Tozuka, A. Ishida, and T. Yamagata. Can Luzon Strait transport play a role in conveying the impact of ENSO to the South China Sea? *Journal of Climate*, 17:3644–3657, 2004. doi: https://doi.org/10.1175/1520-0442(2004)017<3644:CLSTPA>2.0.CO;2.

T. Qu, Y. Du, G. Meyers, A. Ishida, and D. Wang. Connecting the tropical Pacific with Indian Ocean through South China Sea. *Geophysical Research Letters*, 32(24):5–18, 2005. doi: http://dx.doi.org/10.1029/2005GL024698.

T. Qu, Y. T. Song, and T. Yamagata. An introduction to the South China Sea throughflow: Its dynamics, variability, and application for climate. *Dynamics of Atmospheres and Oceans*, 47:3–14, 2009. doi: http://dx.doi.org/10.1016/j.dynatmoce.2008.05.001.

B. Qui and R. Lukas. Seasonal and interannual variability of the north equatorial current, the Mindanao current, and the Kuroshio along the Pacific western boundary. *Journal of Geophysical Research: Oceans*, 101:12,315–12,330, 1996. doi: https://doi.org/10.1029/95JC03204.

R. W. Reynolds, T. M. Smith, C. Liu, D. B. Chelton, K. S. Casey, and M. G. Schlax. Daily High-Resolution-Blended Analyses for Sea Surface Temperature. *Journal of Climate*, 20(22):5473–5496, 2007. doi: https://doi.org/10.1175/2007JCLI1824.1.

J. Rodgers and A. Nicwander. Thirteen Ways to Look at the Correlation Coefficient. *The American Statistician*, 42(1):59–66, 1988. doi: http://dx.doi.org/10.1080/00031305.1988.10475524.

G. v. Schleinitz. Die Forschungsreise S.M.S. "Gazelle" in den Jahren 1874 bis 1876 unter Kommando des Kapitän zur See Freiherrn von Schleinitz. *Humboldt-Universität zu Berlin*, 1889. doi: http://dx.doi.org/10.18452/31.

G. Schott. Die äquatorialen Strömungen des westlichen Stillen Ozeans. *Ann. Hydrog. Berl.*, 67(5):247–257, 1939.

M. Schönau, D. Rudnick, I. Cerovecki, G. Gopalakrishnan, B. Cornuelle, J. McClean, and B. Qiu. The Mindanao Current: Mean structure and connectivity. *Oceanography*, 28: 34–45, 2015. doi: https://doi.org/10.5670/oceanog.2015.79.

S. SeaBird. CTD Basics Application Note 93. 2016. Retrieved from: https://www.seabird.com/asset-get.download.jsa?id=55024931651 [accessed 07 June 2022].

S. SeaBird. Guide to CTDs. Measure Conductivity and Temperature with an Oceanographic CTD. 2018. Retrieved from: https://www.seabird.com/eBooks/CTDs-Explained-Sea-Bird-Scientific [accessed 07 September 2022].

E. Siegel, D. Mayer, and R. Weisberg. A comparison of near-surface current measurement methods. *Proceedings of the IEEE/OES/CMTC Ninth Working Conference on Current Measurements Technology*, pages 44–49, 2008. doi: https://doi.org/10.1109/CCM.2008.4480842.

J. Sprintall, A. L. Gordon, R. Murtugudde, and R. D. Susanto. A semiannual Indian Ocean forced Kelvin wave observed in the Indonesian seas in May 1997. *Journal of Geophysical Research*, 105(C7):17217–17230, 2000. doi: https://doi.org/10.1029/2000JC900065.

J. Sprintall, S. Wijffels, A. L. Gordon, A. Ffield, R. Molcard, R. D. Susanto, I. Soesilo, J. Sopaheluwakan, Y. Surachman, and H. M. Aken. INSTANT: A new international array to measure the Indonesian Throughflow. *Eos (Washington, D.C.)*, 85:369–376, 2004. doi: http://dx.doi.org/10.1029/2004EO390001.

J. Sprintall, S. Wijffels, R. Molcard, and I. Jaya. Direct estimates of the Indonesian Throughflow entering the Indian Ocean: 2004–2006. *Journal of Geosphysical Research: Oceans*, 114(C7), 2009. doi: https://doi.org/10.1029/2008JC005257.

J. Sprintall, A. L. Gordon, S. E. Wijffels, M. Feng, S. Hu, A. Koch-Larrouy, and H. Phillips. Detecting Change in the Indonesian Seas. *Frontiers in Marine Science*, 6, 2019. doi: https://doi.org/10.3389/fmars.2019.00257.

H. Stanski, L. Wilson, and W. Burrows. Survey of Common Verification Methods in Meteorology. *WMO World Weather Watch Tech. Rep.*, 8, 1990.

A. Storto. Variational quality control of hydrographic profile data with non-Gaussian errors for global ocean variational data assimilation systems. *Ocean Model*, 104:226–241, 2016. doi: https://doi.org/10.1016/j.ocemod.2016.06.011.

A. Storto and S. Masina. C-GLORSv5: an improved multipurpose global ocean eddy-permitting physical reanalysis. *Earth System Science Data*, 8:679–696, 2016. doi: https://doi.org/10.5194/essd-8-679-2016.

A. Storto, A. Bonaduce, X. Feng, and C. Yang. Steric Sea Level Changes from Ocean Reanalyses at Global and Regional Scales. *Water*, 11, 2019. doi: https://doi.org/10.3390/w11101987.

R. Susanto and A. Gordon. Makassar Strait Transport: Initial Estimate Based on Arlindo Results. *Marine Technology Society Journal*, 32(4):34–45, 1998.

R. Susanto and A. Gordon. Velocity and transport of the Makassar Strait throughflow. *Journal of Geophysical Research*, 110, 2005. doi: https://doi.org/10.1029/2004JC002425.

R. D. Susanto, W. Zexun, A. Rameyo, F. Bin, L. Shujiang, and F. Guohong. Observations of the Karimata Strait throughflow from December 2007 to November 2008. *Acta Oceanologica Sinica*, 32:1–6, 2013. doi: https://doi.org/10.1007/s13131-013-0307-3.

L. Talley and J. Sprintall. Deep expression of the Indonesian Throughflow: Indonesian intermediate water in the South Equatorial Current. *Journal of Geophysical Research*, 110, 2005. doi: https://doi.org/10.1029/2004JC002826.

S. Tan and H. Zhou. The observed impacts of the two types of El Nino on the North Equatorial Countercurrent in the Pacific Ocean. *Geophysical Research Letters*, 45:10493–10500, 2018. doi: https://doi.org/10.1029/2018GL079273.

N. Taniguchi, T. Takahashi, K. Yoshiki, H. Yamamoto, T. Sugano, H. Mutsuda, and Y. Sakuno. Reciprocal acoustic transmission experiment at Mihara-Seto in the Seto Inland Sea, Japan. *Acoustical Science and Technology*, 42(5):290–293, 2021. doi: http://dx.doi.org/10.1250/ast.42.290.

K. E. Taylor, R. J. Stouffer, and G. Meehl. An overview of CMIP5 and the experiment design. *Bulletin of the American Meteorological Society*, 93:485–498, 2012. doi: https://doi.org/10.1175/BAMS-D-11-00094.1.

J. Toole, M. McCartney, R. Weller, and N. Hogg. Outposts in the Ocean. *Oceanus*, 42(1):20, 2000. Retrieved from: https://link.gale.com/apps/doc/A60138169/AONE?u=43wien&sid=bookmark-AONE&xid=eaf37d07 [accessed 21 Apr 2022].

K. Trenberth. The Climate Data Guide: Nino SST Indices (Nino 1+2, 3, 3.4, 4; ONI and TNI). 2020. Retrieved from: https://climatedataguide.ucar.edu/climate-data/nino-sst-indices-nino-12-3-34-4-oni-and-tni. [accessed 25 August 2022].

G. F. Tydeman. Siboga-Expeditie: Description of the ship and appliances used for scientific exploration. *Leiden*, 1902. Retrieved from: https://www.biodiversitylibrary.org/item/18949#page/7/mode/1up [accessed 06 September 2022].

C. Ummenhofer, A. Biastoch, and C. Böning. Multidecadal Indian Ocean Variability Linked to the Pacific and Implications for Preconditioning Indian Ocean Dipole Events. *Journal of Climate*, 30(5):1739–1751, 2017. doi: https://doi.org/10.1175/JCLI-D-16-0200.1.

UNESCO. Tenth report of the joint panel on oceanographic tables and standards. *Unesco technical papers in marine science*, 36, 1981.

University Rhode Island. Discovery of Sound in the Sea. 2021. Retrieved from: https://dosits.org/galleries/technology-gallery/observing-ocean-currents-and-temperature/acoustic-current-meters/ [accessed 22 Apr 2022].

H. M. van Aken, I. S. Brodjonegoro, and I. Jaya. The deep water motion through the Lifamatola Passage and its contribution to the Indonesian Throughflow. *Deep Sea Research*, 56:1203–1216, 2009. doi: http://dx.doi.org/10.1016/j.dsr.2009.02.001.

P. van Riehl. The Snellius Expedition. *Nature (London)*, 125:761–762, 1930. doi: https://doi.org/10.1038/125761a0.

H. von Storch and F. Zwiers. Statistical Analysis in Climate Research. *Cambridge University Press*, 1, 2001.

K. Vranes, A. L. Gordon, and A. Ffield. The heat transport of the Indonesian throughflow and implications for the Indian Ocean Heat Budget. *Deep Sea Research, Part II*, 49: 1391–1410, 2002. doi: https://doi.org/10.1016/S0967-0645(01)00150-3.

C. Wang, W. Wang, D. Wang, and Q. Wang. Interannual variability of the South China Sea associated with El Niño. *Journal of Geophysical Research*, 111, 2006. doi: http://dx.doi.org/10.1029/2005JC003333.

F. Wang and D. Hu. A time-dependent baroclinic model on NEC bifurcation. *Chinese Journal of Oceanology and Limnology*, 30(1):186–191, 2012. doi: http://dx.doi.org/10.1007/s00343-012-1213-9.

Q. Wang and D. Hu. Bifurcation of the North Equatorial Current derived from altimetry in the Pacific Ocean. *Journal of Hydrodynamics*, 18:620–626, 2006. doi: https://doi.org/10.1016/S1001-6058(06)60144-3.

X. Wang, B. Tong, D. Wang, and I. Yang. Variations of the North Equatorial Current Bifurcation and the SSH in the western Pacific associated with El Niño flavors. *Journal of Geophysical Research: Ocean*, 125, 2020. doi: https://doi.org/10.1029/2019JC015733.

J. Waters, D. J. Lea, M. J. Martin, D. Storkey, and J. While. Describing the development of the new FOAM-NEMOVAR system in the global 1/4 degree configuration. *Technical Report 578, Met Office*, 2013.

M. C. Wattimena, A. Atmadipoera, M. Purba, I. W. Nurjaya, and F. Syamsudin. Indonesian Throughflow (ITF) variability in Halmahera Sea and its coherency with New Guinea Coastal Current. *IOP Conference Series: Earth and Environmental Science*, 176, 2018. doi: https://doi.org/10.1088/1755-1315/176/1/012011.

R. Weller and R. Davis. A vector measuring current meter. *Deep Sea Research Part A. Oceanographic Research Papers*, 27:565–581, 1980. doi: https://doi.org/10.1016/0198-0149(80)90041-2.

M. Wheeler and J. McBride. *Australian-Indonesian monsoon. In: Intraseasonal Variability in the Atmosphere-Ocean Climate System.* Springer, Berlin, Heidelberg, 2005. doi: https://doi.org/10.1007/b138817.

M. Wheeler and H. Nguyen. TROPICAL METEOROLOGY AND CLIMATE | Equatorial Waves. In G. R. North, J. Pyle, and F. Zhang, editors, *Encyclopedia of Atmospheric Sciences (Second Edition)*, pages 102–112. Academic Press, second edition edition, 2015. doi: https://doi.org/10.1016/B978-0-12-382225-3.00414-X.

W. White, Y. Tourre, M. Barlow, and M. Dettinger. A delayed action oscillator shared by biennial, interannual, and decadal signals in the Pacific Basin. *Journal of Geophysical Research*, 108, 2003. doi: https://doi.org/10.1029/2002JC001490.

S. Wijffels and G. Meyers. An intersection of oceanic waveguides: Variability in the Indonesian Throughflow region. *Journal of Physical Oceanography*, 34:1232 – 1253, 2004. doi: https://doi.org/10.1175/1520-0485(2004)034<1232:AIOOWV>2.0.CO;2.

Wikipedia. A sketch of an ocean with the Ekman spiral and transport depicted that are generated by a zonal wind stress. 2021. Retrieved from: https://commons.wikimedia.org/wiki/File:Sketch_ocean_zonal_wind_stress_ekman_spiral_transport.jpg [accessed 25 Sep 2022].

R. v. Willemoes-Suhm. Von der Challenger-Expedition: Briefe an C. Th. E. v. Siebold. *Münchener DigitalisierungsZentrum (MDZ)*, 1874.

K. Wyrkti. An equatorial jet in the Indian Ocean. *Science*, 262–264:181(4096), 1973. doi: https://doi.org/10.1126/science.181.4096.262.

K. Wyrtki. Physical Oceanography of the Southeast Asian waters. *UC San Diego: Library – Scripps Digital Collection*, 1961. Retrieved from: https://escholarship.org/uc/item/49n9x3t4 [accessed 06 July 2022].

K. Wyrtki. Response of sea surface topography to the 1976 El Niño. *Journal of Physical Oceanography*, 9:1223–1231, 1979. doi: https://doi.org/10.1175/1520-0485(1979)009<1223:TROSST>2.0.CO;2.

K. Wyrtki. Indonesian Throughflow and the associated pressure gradient. *Journal of Geophysical Research*, 92:12941–12946, 1987. doi: https://doi.org/10.1029/JC092iC12p12941.

K. Wyrtki and R. Kendall. Transports of Pacific equatorial countercurrent. *Journal of Geophysical Research*, 72:2073–2076, 1967. doi: https://doi.org/10.1029/JZ072i008p02073.

W. Yan, X. Tengfei, L. Shujiang, R. Susanto, A. Teguh, T. Mukti, T. Wei, and W. Zexun. Seasonal variation of water transport through the Karimata Strait. *Acta Oceanologica Sinica*, 38:47–57, 2019. doi: http://dx.doi.org/10.1007/s13131-018-1224-2.

Z. Yu, S. Shen, J. McCreary, M. Yaremchuk, and R. Furue. South China Sea throughflow as evidence by satellite images and numerical experiments. *Geophysical Research Letters*, 340, 2007. doi: http://dx.doi.org/10.1029/2006GL028103.

D. Yuan, X. Yin, and X. Li. A Maluku Sea intermediate western boundary current connecting Pacific Ocean circulation to the Indonesian Throughflow. *Nature Communications*, 13, 2022. doi: https://doi.org/10.1038/s41467-022-29617-6.

H. Zuo, M. Balmaseda, and K. Mogensen. The new eddy-permitting ORAP5 ocean reanalysis: description, evaluation and uncertainties in climate signals. *Climate Dynamics*, 49, 2015. doi: http://dx.doi.org/10.1007/s00382-015-2675-1.

H. Zuo, M. A. Balmaseda, S. Tietsche, K. Mogensen, and M. Mayer. The ECMWF operational ensemble reanalysis–analysis system for ocean and sea ice: a description of the system and assessment. *Ocean Science*, 15:779–808, 2019. doi: https://doi.org/10.5194/os-15-779-2019.

H. Zuo, M. A. Balmaseda, E. de Boisseson, S. Tietsche, M. Mayer, and P. de Rosnay. The ORAP6 ocean and sea-ice reanalysis: description and evaluation. *EGU General Assembly 2021*, 2021. doi: https://doi.org/10.5194/egusphere-egu21-9997.

A. Appendix

Table 6: Comparison of the mean ITF transport estimates during the INSTANT Program (2004-2006). Transport averages are given in Sverdrup (Sv) with negative values representing southward-directed transport (toward the Indian Ocean).

Strait	OBS	CGLORS	FOAM	GLORYS2V4	ORAS5	ORAP6	REANA Mean
Makassar (all)	-10.7	-11.6	-11.0	-10.7	-12.3	-11.8	-11.5
Makassar (NN/INT)		-9.8	-10.9	-9.0	-11.4	-11.0	-10.5
Lombok (all)	-2.6	-2.3	-2.3	-0.9	-1.1	-1.1	-1.5
Lombok (NN/INT)		-1.7	-1.7	-0.6	-0.8	-0.8	-1.1
Ombai (all)	-5.3	-5.9	-3.5	-2.6	-2.8	-2.8	-3.5
Ombai (NN/INT)		-6.9	-3.2	-3.1	-3.8	-3.7	-4.1
Timor (all)	-6.7	-6.7	-7.6	-10.6	-9.9	-9.5	-8.9
Timor (NN/INT)		-7.8	-8.1	-11.9	-11.3	-10.1	-9.7

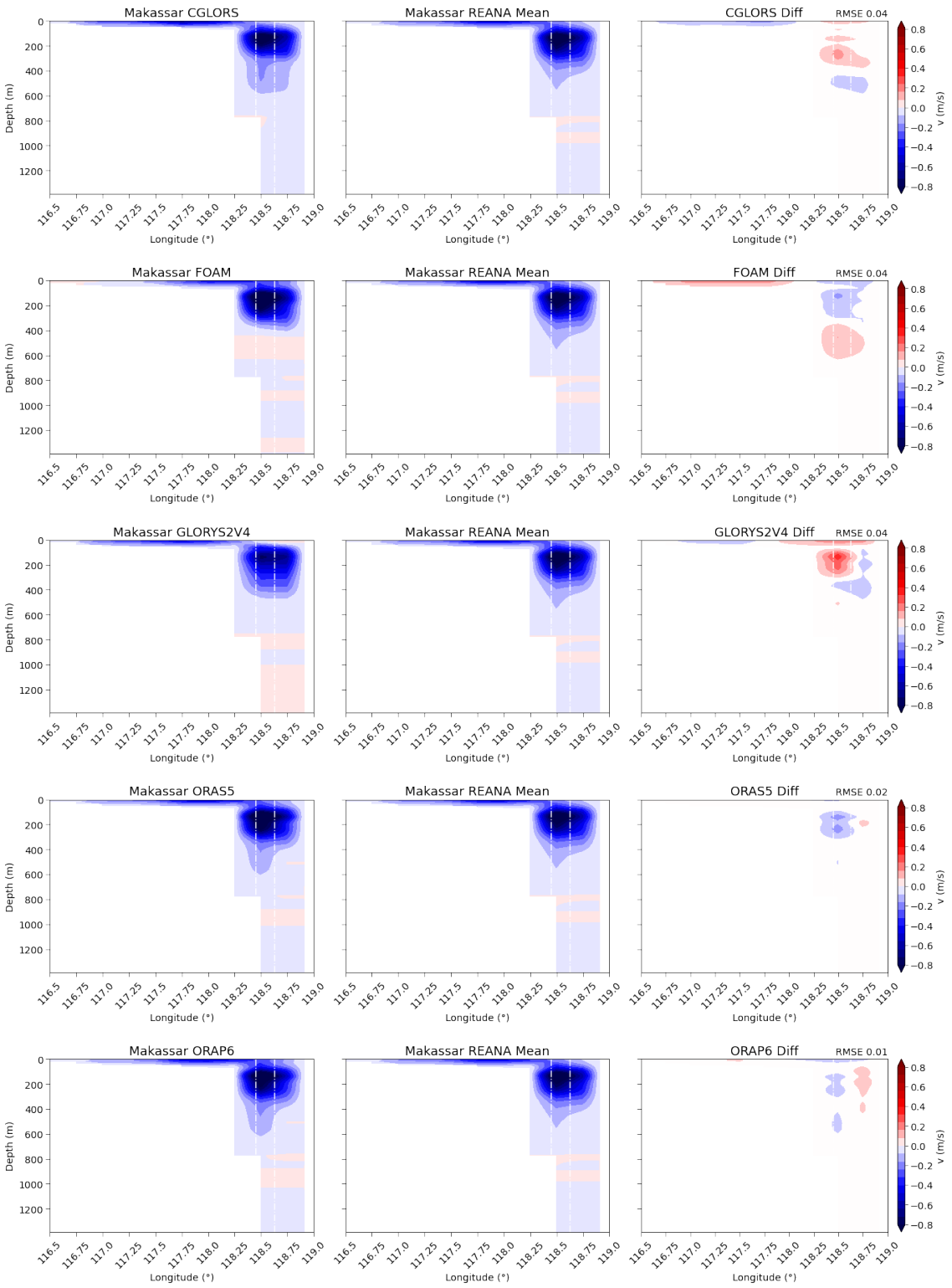

Figure 36: Mean ASV cross sections in Makassar Strait as represented by CGLORS, FOAM, GLORYS2V4, ORAS5, and ORAP6 using all horizontal grid points (left column), and by the Reanalysis mean (middle column) from January 2004 to December 2006 (INSTANT program). The right column shows their differences with the RMSE given in the top right corner. Negative values indicate southward-directed velocities (toward the Indian Ocean). White dash-dot lines represent mooring locations.

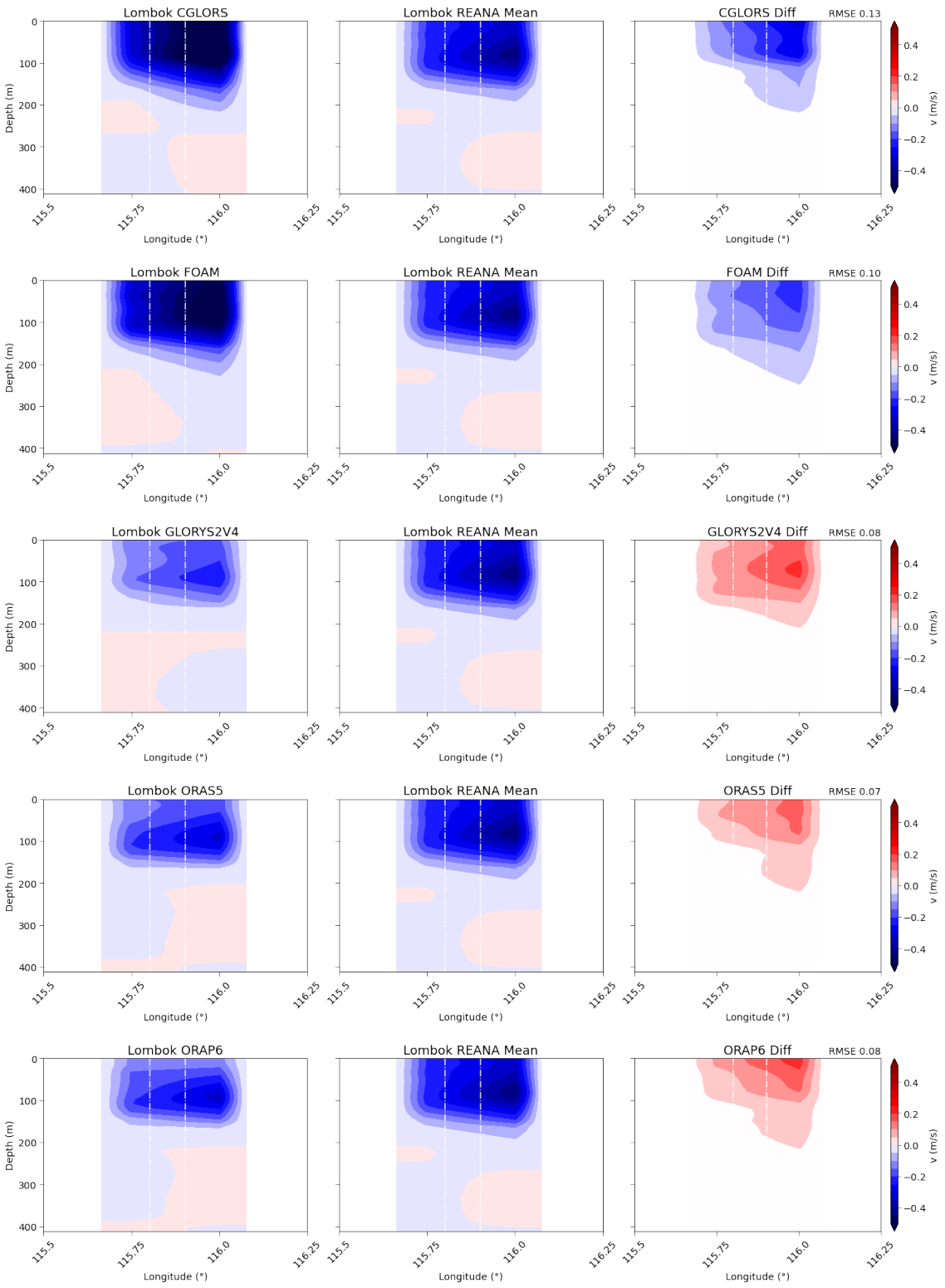

Figure 37: Mean ASV cross sections in Lombok Strait as represented by CGLORS, FOAM, GLORYS2V4, ORAS5, and ORAP6 using all horizontal grid points (left column), and by the Reanalysis mean (middle column) from January 2004 to December 2006 (INSTANT program). The right column shows their differences with the RMSE given in the top right corner. Negative values indicate southward-directed velocities (toward the Indian Ocean). White dash-dot lines represent mooring locations.

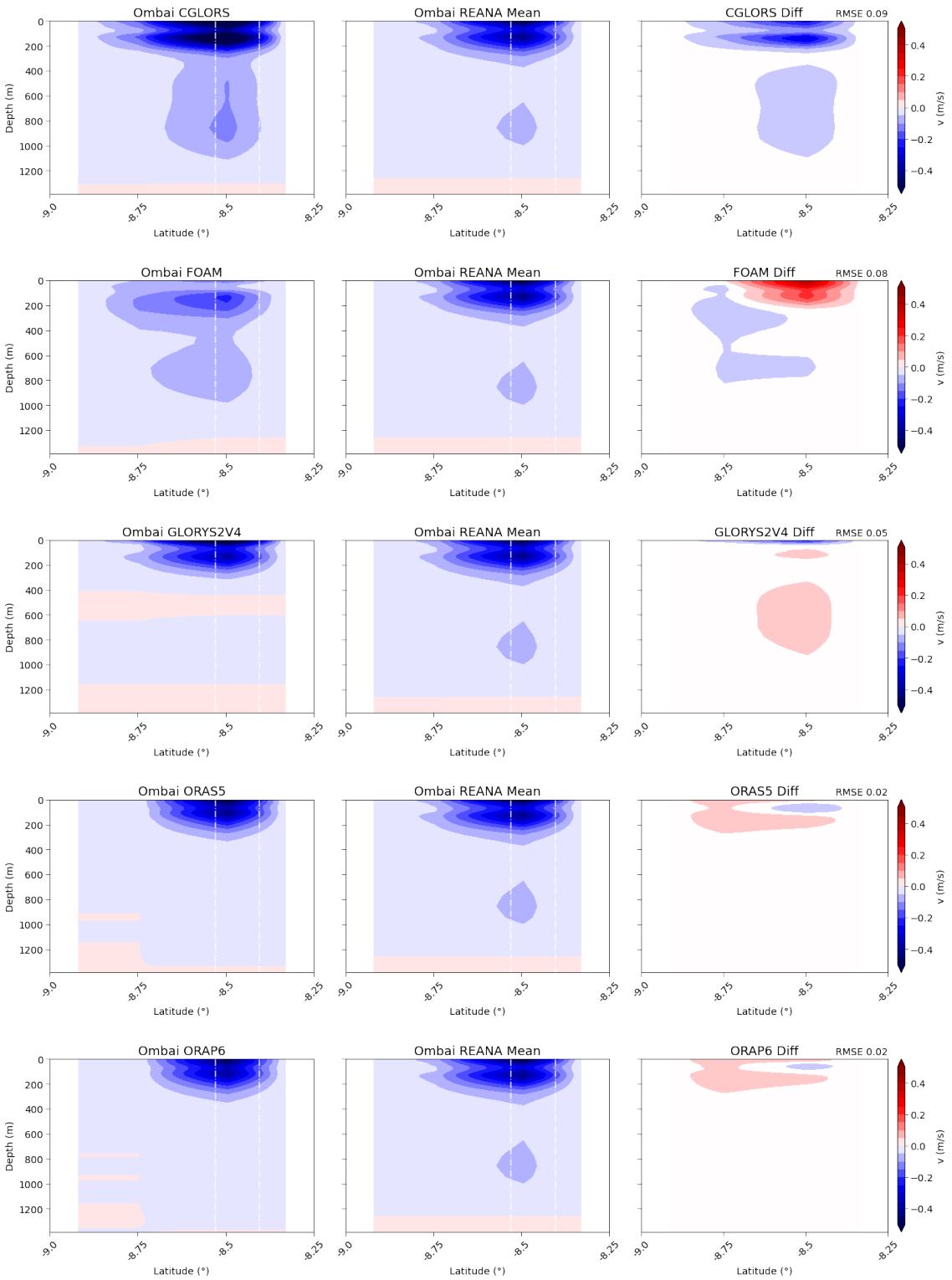

Figure 38: Mean ASV cross sections in Ombai Strait as represented by CGLORS, FOAM, GLORYS2V4, ORAS5, and ORAP6 using all horizontal grid points (left column), and by the Reanalysis mean (middle column) from January 2004 to December 2006 (INSTANT program). The right column shows their differences with the RMSE given in the top right corner. Negative values indicate southward-directed velocities (toward the Indian Ocean). White dash-dot lines represent mooring locations.

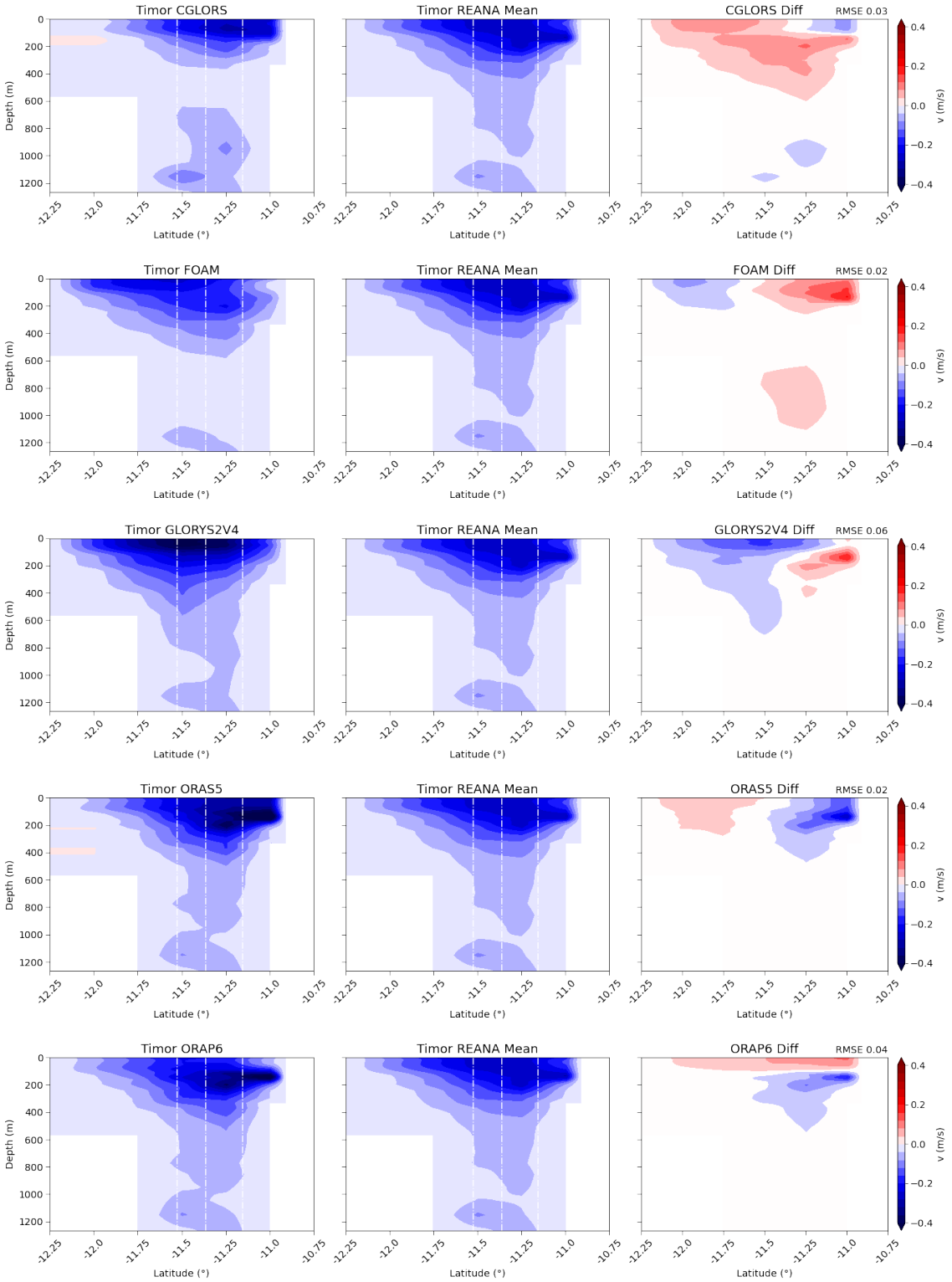

Figure 39: Mean ASV cross sections in Timor Passage as represented by CGLORS, FOAM, GLORYS2V4, ORAS5, and ORAP6 using all horizontal grid points (left column), and by the Reanalysis mean (middle column) from January 2004 to December 2006 (INSTANT program). The right column shows their differences with the RMSE given in the top right corner. Negative values indicate southward-directed velocities (toward the Indian Ocean). White dash-dot lines represent mooring locations.

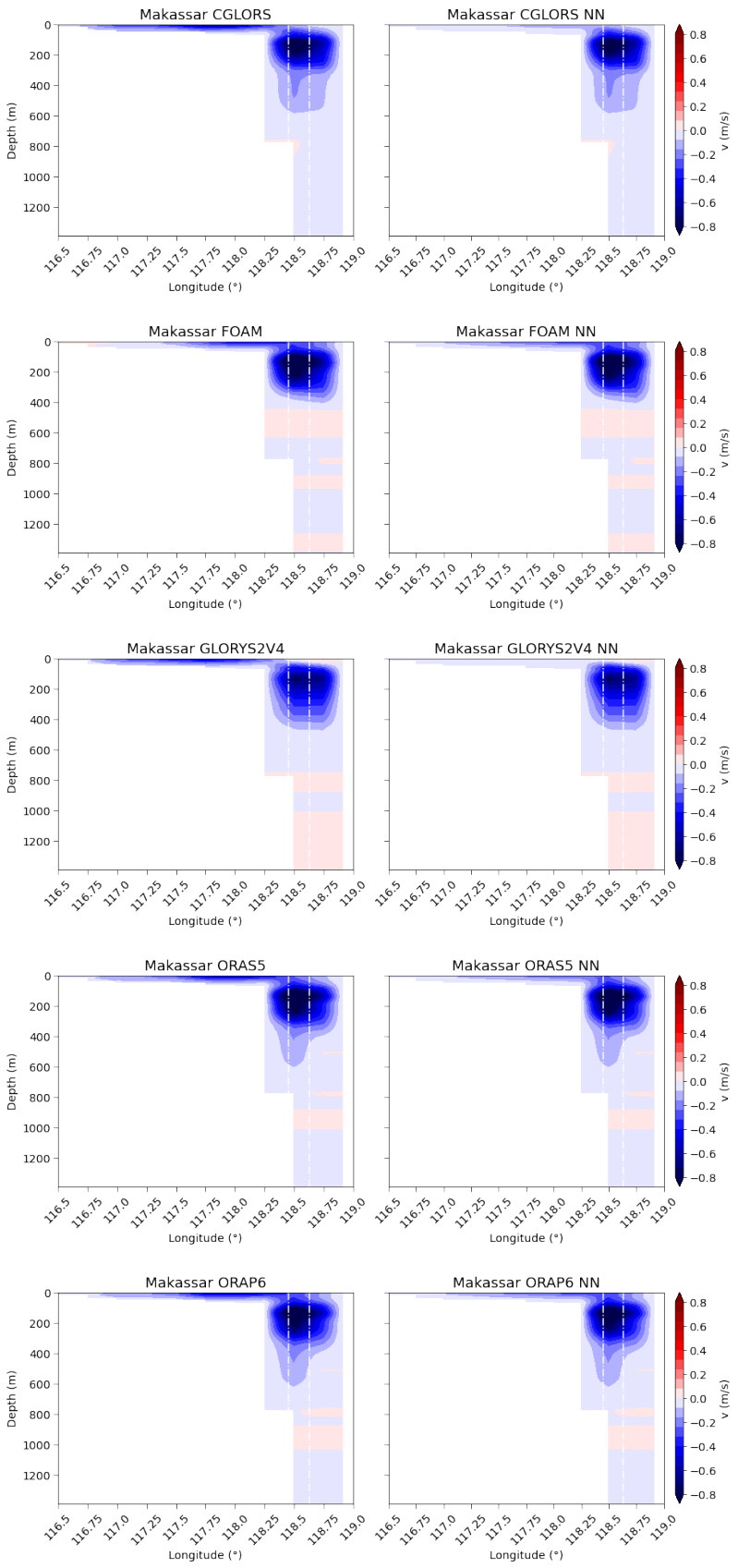

Figure 40: Mean ASV cross sections in Makassar Strait as represented by CGLORS, FOAM, GLORYS2V4, ORAS5, and ORAP6 using all horizontal grid points (left column) and NN-method (right column) from January 2004 to December 2006 (INSTANT program). Negative values indicate southward-directed velocities (toward the Indian Ocean). White dash-dot lines represent mooring locations.

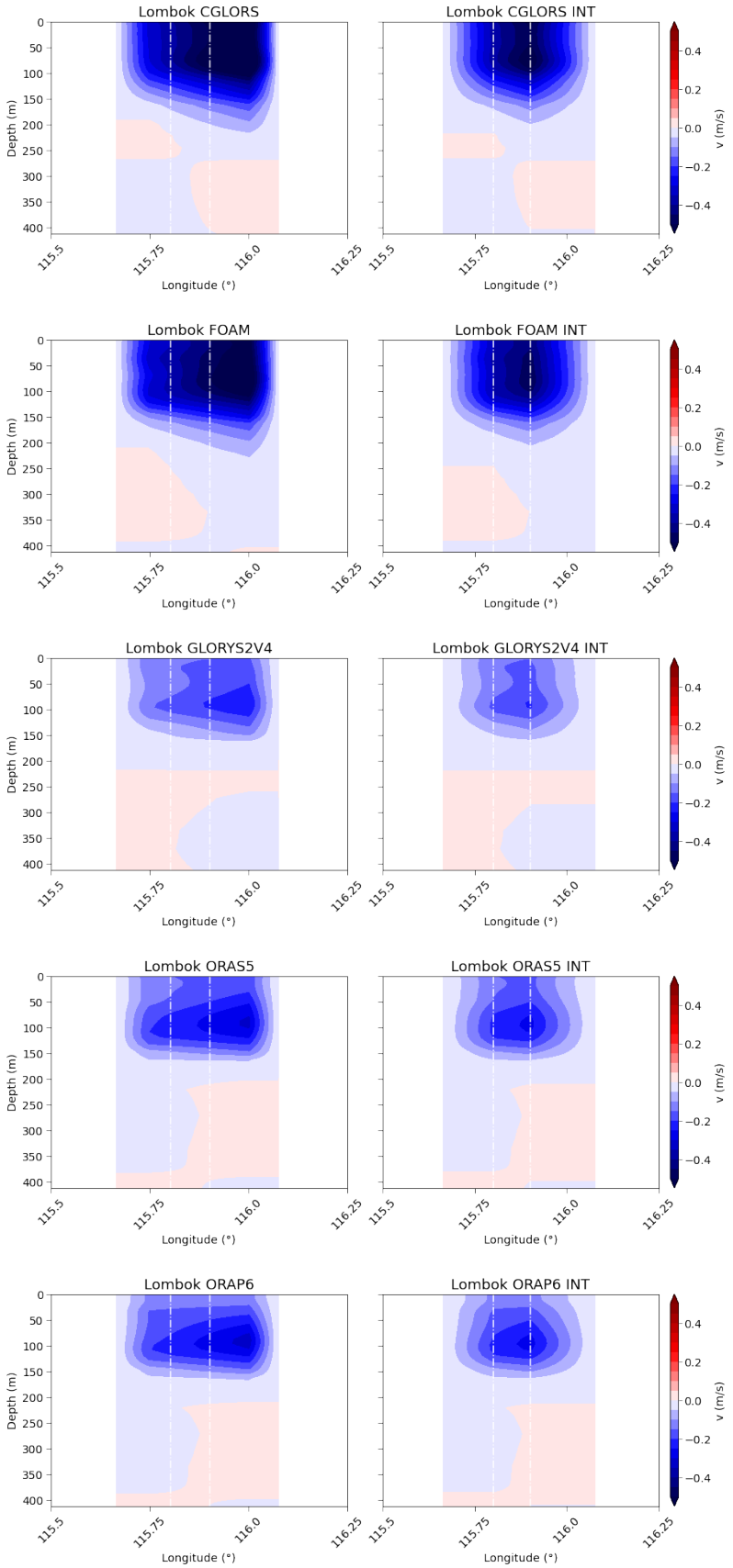

Figure 41: Mean ASV cross sections in Lombok Strait as represented by CGLORS, FOAM, GLORYS2V4, ORAS5, and ORAP6 using all horizontal grid points (left column) and INT-method (right column) from January 2004 to December 2006 (INSTANT program). Negative values indicate southward-directed velocities (toward the Indian Ocean). White dash-dot lines represent mooring locations.

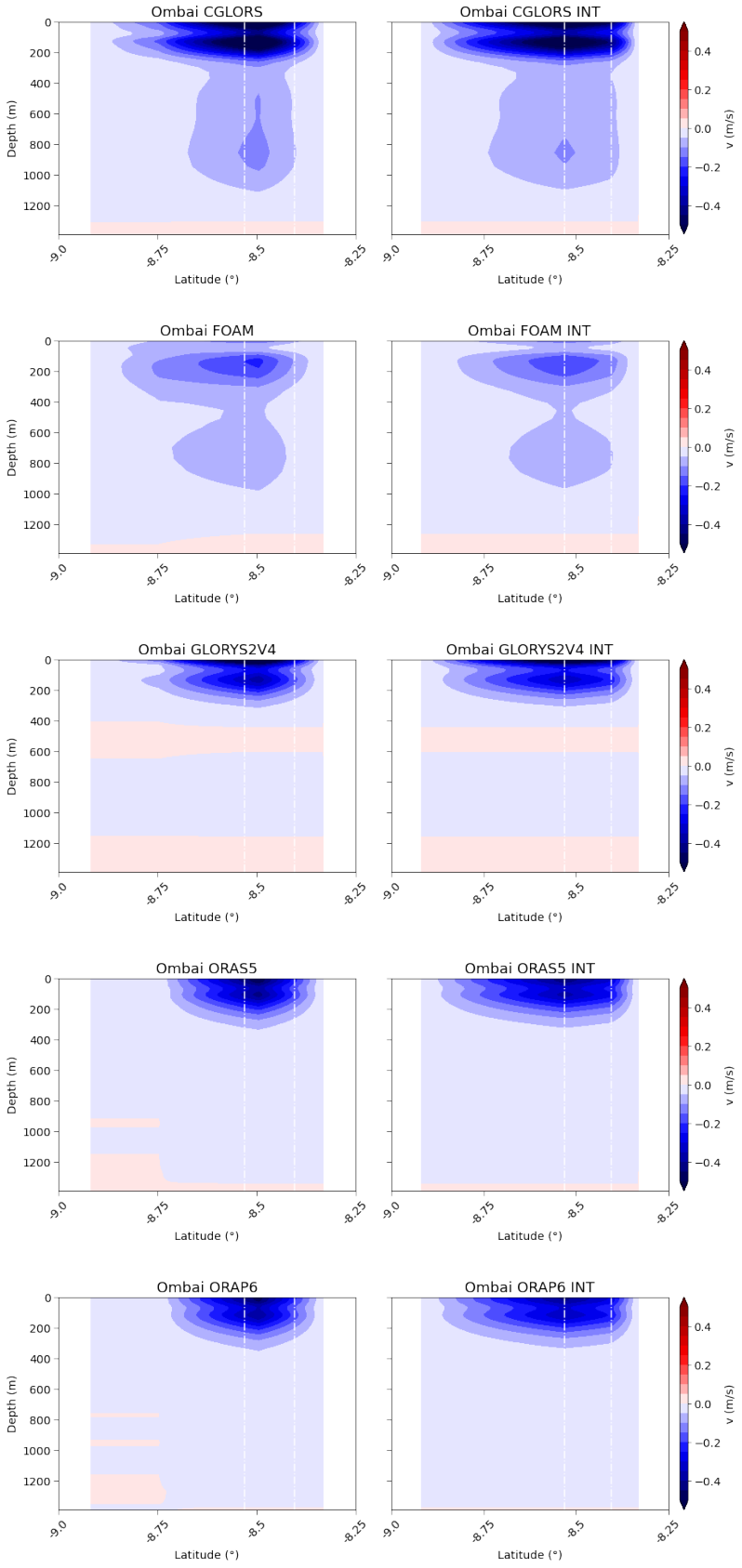

Figure 42: Mean ASV cross sections in Ombai Strait as represented by CGLORS, FOAM, GLORYS2V4, ORAS5, and ORAP6 using all horizontal grid points (left column) and INT-method (right column) from January 2004 to December 2006 (INSTANT program). Negative values indicate southward-directed velocities (toward the Indian Ocean). White dash-dot lines represent mooring locations.

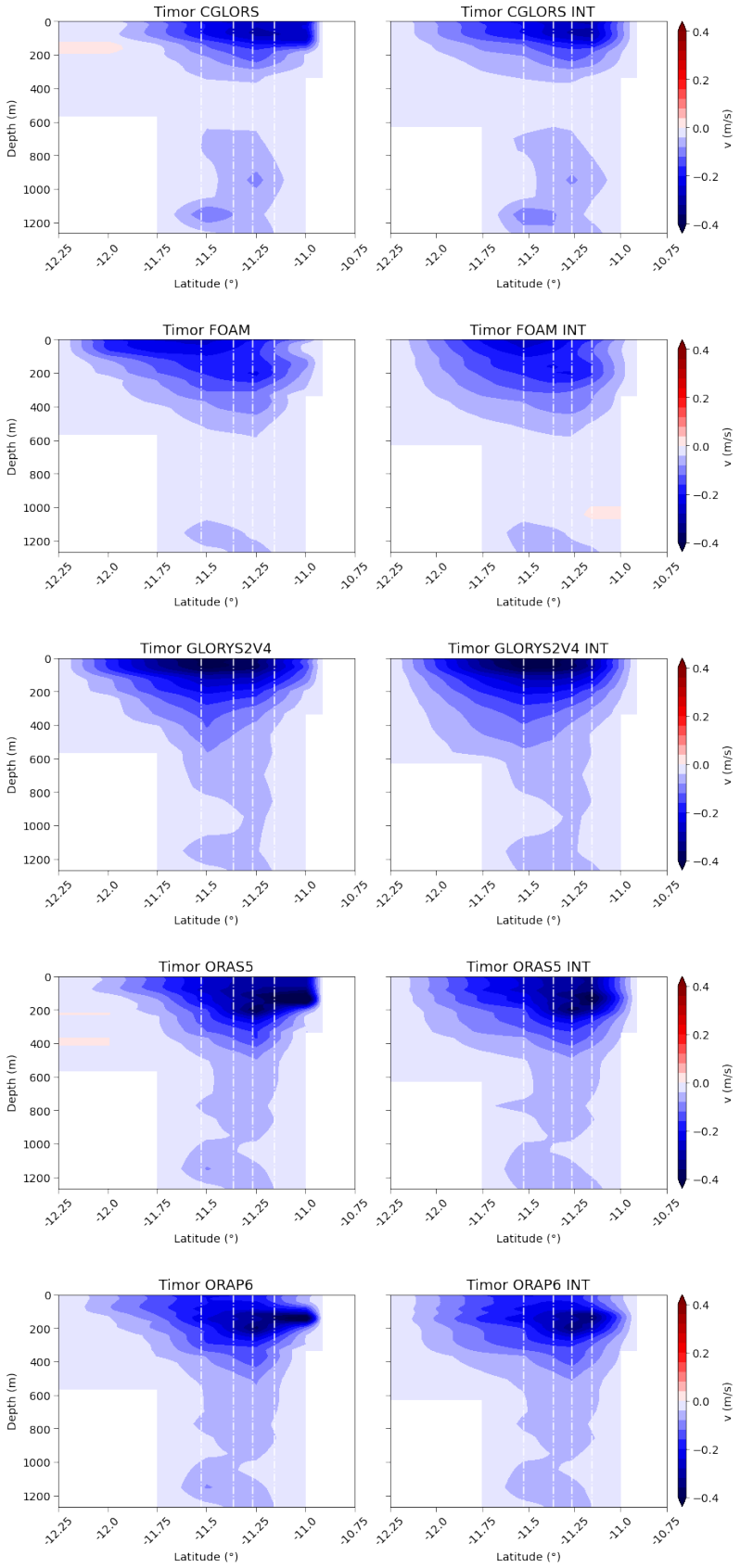

Figure 43: Mean ASV cross sections in Timor Passage as represented by CGLORS, FOAM, GLORYS2V4, ORAS5, and ORAP6 using all horizontal grid points (left column) and INT-method (right column) from January 2004 to December 2006 (INSTANT program). Negative values indicate southward-directed velocities (toward the Indian Ocean). White dash-dot lines represent mooring locations.

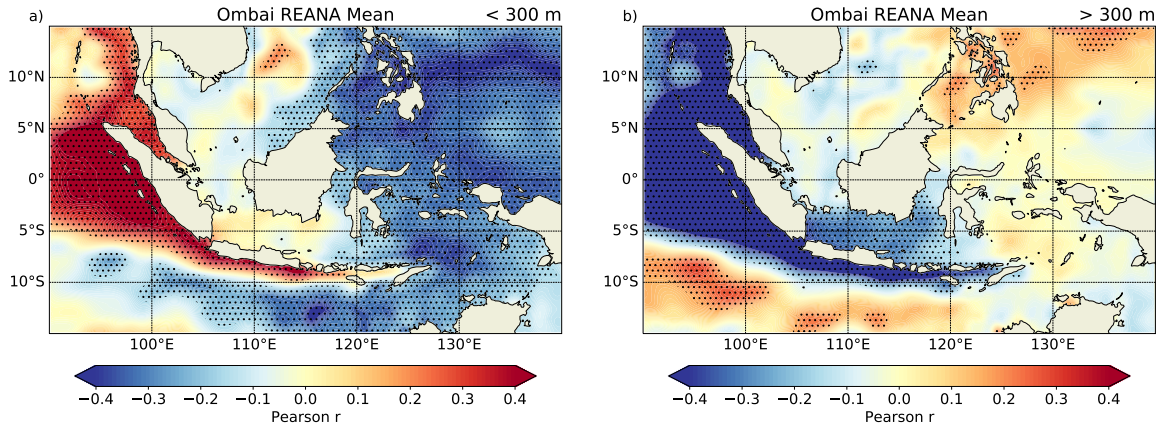

Figure 44: Correlation maps expressing correlations between integrated transport anomalies in the (a upper and (b lower layer through Ombai Strait and sea level anomalies as represented by the Reanlaysis mean. Anomalies cover the period from 2004 to 2017 at zero lag. Blueish (redish) values denote negative (positive) correlations. Stippling indicates significant correlation coefficients above the 95% confidence level.

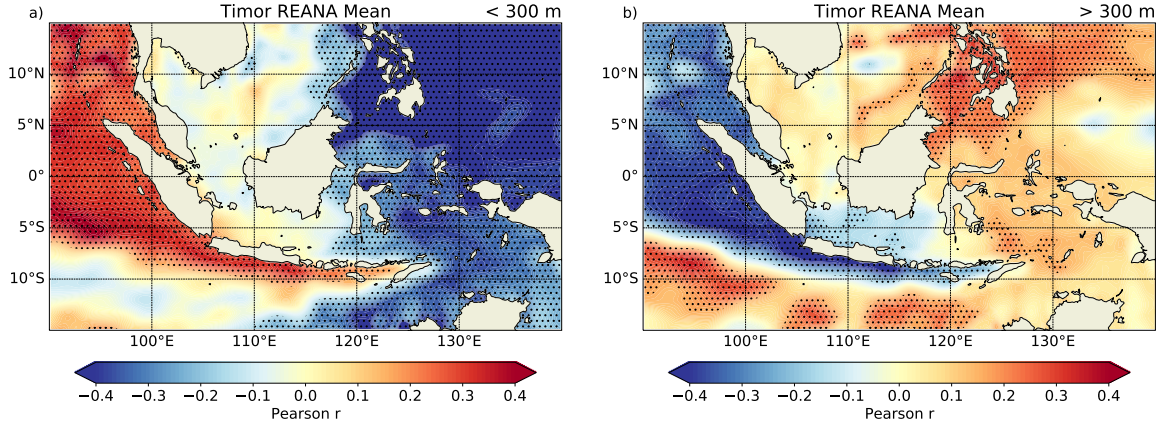

Figure 45: Correlation maps expressing correlations between integrated transport anomalies in the (a upper and (b lower layer through Timor Passage and sea level anomalies as represented by the Reanlaysis mean. Anomalies cover the period from 2004 to 2017 at zero lag. Blueish (redish) values denote negative (positive) correlations. Stippling indicates significant correlation coefficients above the 95% confidence level.